Osaka University Knowledge Archive

Title	Energy resolution of CANDLES detector for studying neutrino-less double beta decay of 48Ca
Author(s)	Bui, Tuan Khai
Citation	大阪大学, 2020, 博士論文
Version Type	VoR
URL	https://doi.org/10.18910/77473
rights	
Note	

Osaka University Knowledge Archive : OUKA

https://ir.library.osaka-u.ac.jp/

Osaka University

Osaka University
Graduate School of Science
Department of Physics

Doctor Thesis

Energy resolution of CANDLES detector for studying the neutrino-less double beta decay of ^{48}Ca

by Bui Tuan Khai

Osaka - September 14, 2020

Abstract

Neutrino-less double beta decay ($0\nu\beta\beta$) is a useful tool to determine the absolute neutrino mass and nature of neutrino (Majorana or Dirac particle). The $0\nu\beta\beta$ is forbidden in Standard Model (SM) due to the violation of lepton number conservation. The CANDLES experiment is searching for the $0\nu\beta\beta$ of ^{48}Ca using CaF_2(pure) scintillator as the detector and the source. Scintillation photons are collected by Photo Multiplier Tubes (PMTs) surrounding the crystals. A Flash Analog-to-Digital Converter records the waveform of each PMT. The two-neutrino double beta decay ($2\nu\beta\beta$), which is allowed process in SM, behaves as an irreducible background in the $0\nu\beta\beta$ experiments. In our plan, to achieve the effective neutrino mass sensitivity below the Inverted Hierarchy, a ton-scale detector containing 600 kg of ^{48}Ca is going to be developed; consequently, we will have a huge background from $2\nu\beta\beta$ from ^{48}Ca. To discriminate the $0\nu\beta\beta$ from $2\nu\beta\beta$, the energy resolution must be improved.

The CaF_2 signal contains many photoelectrons; hence, the energy resolution should be equal to the statistical fluctuation of the photoelectron number. In the current data analysis, the obtained energy resolution (2.6 %) is bigger than the statistical fluctuation (1.6 %) at Q-value of ^{48}Ca. There is another (or more) fluctuation that affects the energy resolution. Because of the long decay time of CaF_2 (1 μsec), we make a signal integral of 4 μsec to calculate the obtained energy. Thus, the baseline fluctuation is accumulated in the signal integration, and it makes the energy resolution worse. In this thesis, the error of charge measurement caused by the baseline fluctuations is discussed. The errors of charge measurement include the digitization error, baseline noise, and error in the baseline measurement. Among these fluctuations, the error in baseline measurement, which is linearly proportional to the integration interval, is the most severe with the fluctuation of about 1 % at Q-value of ^{48}Ca. This baseline fluctuation is accumulated to be more severe due to the long sampling interval for CaF_2 scintillator, while it is negligible in the short decay constant scintillator.

To avoid the baseline fluctuation, the photon counting method is consid-

ered to calculate the obtained energy. A threshold is set individually for every PMT for detecting photoelectrons in the waveform, and the energy is equivalent to the total photoelectrons. Thus, baseline fluctuation is avoided because of no signal integration. However, many multi-photoelectron signals occur near the rising edge of the waveform. These multi-photoelectron signals are recognized as a single-photoelectron signal; hence, there are lost photoelectrons when introducing photon counting. To avoid the baseline fluctuation and reduce the loss of photoelectrons, an alternative method named partial photon counting is introduced. In this method, the waveform is divided into two regions for calculating the energy: the energy in the prompt region containing many multi-photoelectron signals near the rising edge is calculated with signal integration, and the energy of the latter region near the tail of the waveform is calculated with photon counting. With this method, the energy resolution is improved 4.5-4.0 % at 1460 keV (γ-ray of ^{40}K) and 3.3-2.9% at 2614 keV (γ-ray of ^{208}Tl). With the improvement of resolutions at ^{40}K and ^{208}Tl peaks, the resolution at Q-value of ^{48}Ca is estimated to be improved to 2.2 %, and the sensitivity for $0\nu\beta\beta$ half-life can be improved by 1.09 times.

The energy resolution is an important key to improve the sensitivity in the search for $0\nu\beta\beta$ decay. At the cryogenic temperature, the scintillation light yield of CaF_2(pure) is increased by four times, so that the statistical fluctuation is much improved. However, the decay constant is extended 40 times; the fluctuation can be tremendously huge. With the photon counting method developed in this thesis, this baseline fluctuation can be removed, and the energy resolution 0.8-0.9 % can be achieved. This energy resolution is enough to achieve the $0\nu\beta\beta$ half-life sensitivity of about 10^{27} years, which is equivalent to the effective neutrino mass of 27-118 meV. Comparing to the current world-best sensitivity of effective neutrino mass of 61-165 meV reported by KamLAND-Zen, photon counting at the cryogenic temperature can be a promising method to achieve the new world-best limit.

Contents

1 Neutrino mass and Double Beta Decay **1**
1.1 Neutrino Physics . . . 1
1.1.1 A brief history of neutrino . . . 1
1.1.2 Neutrino oscillation . . . 3
1.1.3 Neutrino mass . . . 6
1.2 Double Beta Decay . . . 8
1.2.1 Two-Neutrino Double Beta Decay ($2\nu\beta\beta$) . . . 9
1.2.2 Neutrino-less Double Beta Decay ($0\nu\beta\beta$) . . . 11
1.3 Status of some $0\nu\beta\beta$ experiments . . . 13

2 CANDLES experiment **18**
2.1 Introduction of CANDLES . . . 18
2.2 Detector setup . . . 19
2.2.1 Kamioka Underground Observatory . . . 19
2.2.2 Detector setup . . . 21
2.2.3 Scintillator . . . 23
2.2.4 Data Acquisition system . . . 26
2.3 Background . . . 29
2.3.1 The $2\nu\beta\beta$ events . . . 30
2.3.2 The external background from (n, γ) reactions . . . 30
2.3.3 Background from ^{49}Ca . . . 30
2.3.4 The β-decay events from ^{208}Tl . . . 31
2.3.5 The BiPo sequential decay . . . 31
2.4 Enrichment . . . 32
2.5 CANDLES: current and future prospect . . . 32

3 Background of $2\nu\beta\beta$ and Energy resolution **34**
3.1 Overview of $2\nu\beta\beta$ background . . . 34
3.2 Energy resolution in CANDLES III . . . 36
3.2.1 Energy resolution of a scintillator detector . . . 36
3.2.2 The current energy resolution of CANDLES III . . . 38

3.2.3 Statistical fluctuation 39
3.2.4 Crystal dependence 40
3.2.5 Improve the energy resolution 41

4 Baseline fluctuation in CANDLES III 43
4.1 Dark Current 44
4.2 Digitization Error 46
4.2.1 Introduction of digitization error 46
4.2.2 Estimate the effect of digitization error 49
4.3 Noise in 62 PMTs of CANDLES 53
4.3.1 Noise Analysis 53
4.3.2 Effect of noise in 10-inch PMTs 54
4.4 Error of baseline measurements 57
4.4.1 Uncertainty of pedestal value 57
4.4.2 Error accumulation of the signal integration 58
4.5 Summary of baseline fluctuations 61

5 Measurement at Kamioka Underground Observatory 64
5.1 DAQ setup for photon counting 64
5.1.1 DAQ setup for photon counting 64
5.1.2 Data taking efficiency in photon counting measurement 66
5.2 Event Reconstruction 68
5.2.1 Data Quality check 69
5.2.2 Pulse Shape Discrimination by Charge Ratio 70
5.2.3 Start Channel 71
5.2.4 Charge of single photoelectron 72
5.2.5 Event Position Reconstruction 73

6 Photon Counting Analysis 76
6.1 Threshold for Photon Counting Analysis in CANDLES 76
6.1.1 Threshold for photon counting 77
6.1.2 Charge of single photoelectron obtained by photon counting 79
6.2 Overlap of single photoelectron signals in Photon Counting . . 80
6.3 Partial Photon Counting 82
6.3.1 Distribution of photoelectron charge by timebin 83
6.3.2 Partial Photon Counting 84

7 Result and Discussion 90
7.1 Discussion about Energy Resolution 90
7.1.1 Fluctuations affecting the energy resolution 90

7.1.2 Discussion about the remaining fluctuation 92
7.2 Improvement of energy resolution and $0\nu\beta\beta$ half-life limit . . . 93
7.2.1 Energy resolution at Q-value of ^{48}Ca 93
7.2.2 Estimate the improvement of the $0\nu\beta\beta$ half-life limit . 96

8 Conclusion **98**

9 Future Prospect **100**
9.1 CaF_2(pure) scintillation properties at low temperature 100
9.2 Photon Counting for low temperature measurement 101

A Energy spectrum of double beta decay **104**

B PMT Resolution **107**

C Signal Overlap in Digitization Error Estimation **111**

D Digitization error: Signal Overlap and Peak Shifting **113**

E Pedestal Fluctuation - Error in baseline measurement **122**

F Overlap in Photon Counting **130**

G Threshold in Photon Counting **133**

Bibliography **135**

List of Figures

1.1 Elementary particles in Standard Model 2
1.2 Neutrino Mass Hierarchy in NH and IH 6
1.3 Energy spectrum of β-decay from ^{3}H 7
1.4 Effective neutrino mass as a function of lightest neutrino . . . 8
1.5 Mass of isobaric nuclei 9
1.6 Q-value of various double beta decay isotopes 10
1.7 The diagrams of beta decays 12
1.8 Spectrum of kinetic energy of $2e^{-}$ 12
1.9 The NME of $0\nu\beta\beta$ (top) and the half-life of $0\nu\beta\beta$ 14

2.1 Decay scheme of ^{48}Ca 19
2.2 CANDLES experiment in Kamioka Underground Observatory 20
2.3 The muon flux at different underground observatories 20
2.4 Experimental setup CANDLES III detector 22
2.5 Layout of CaF_2(pure) crystals in CANDLES III 23
2.6 Layout of 62 PMTs in CANDLES III detector. 23
2.7 Optical properties of different components in CANDLES . . . 25
2.8 Typical pulse shapes obtained in CANDLES III detector . . . 26
2.9 The μTCA DAQ system in CANDLES 27
2.10 Decay chain of impurities as background in CANDLES 31

3.1 Simulation histograms of $0\nu\beta\beta$ and $2\nu\beta\beta$ of ^{48}Ca 35
3.2 Energy Resolutions in CANDLES III 39
3.3 The dependence of mean value of ^{208}Tl γ-peak on the crystal ID 40
3.4 A sum waveform of 62 PMTs with a CaF_2 event 41

4.1 Dark Current rate for every 100 nsec 44
4.2 Dark Current Rate of all PMTs 45
4.3 Dark Current rate and its fluctuation of 62 PMTs 45
4.4 The Gaussian distribution of true pedestal 47
4.5 Digitization Error as a function of measured pedestal 47

4.6 The 1p.e. charge value as a function of the measured pedestal 48
4.7 Profile of energy scale factor in 1 year 49
4.8 Estimated digitization error effect on the energy spectrum . . 51
4.9 Estimated digitization error at the ^{40}K and ^{208}Tl peaks 52
4.10 Estimated fluctuation of digitization error effect 52
4.11 Fitting function on the baselines of some PMTs 54
4.12 Noise cycle and noise amplitude in 62 PMTs of CANDLES . . 55
4.13 Distributions of the amplitude and cycle of 730 nsec noise . . . 55
4.14 The $\text{Effect}_{\text{noise}}$ distributions with different integration intervals 56
4.15 Maximum fluctuation of 730 nsec noise 57
4.16 Sigma of pedestal as a function of pedestal 59
4.17 Accumulated fluctuation in the baseline of PMT27 59
4.18 The pedestal fluctuation in many PMTs 60
4.19 Noise fluctuation per data point 60
4.20 Summary of fluctuations in baseline 62

5.1 DAQ Middleware configurations 65
5.2 Waveform in Photon Counting and Physics Run 66
5.3 Read time as a function of packet size in μTCA DAQ system . 67
5.4 Estimated DAQ efficiency in photon counting measurement . . 67
5.5 Obtained DAQ efficiency in photon counting measurement . . 68
5.6 Bad quality waveform examples 69
5.7 Charge Ratio distribution 70
5.8 CaF_2 + LS examples 71
5.9 Start Channel distribution 72
5.10 Charge of single photoelectron of 62 PMTs 72
5.11 Two-dimensional distributions of CaF_2 events' positions 73
5.12 Distributions of event positions in X-, Y-, Z- axes 74

6.1 Peak Distribution of 1p.e. signal of PMT01 77
6.2 Distribution of 200-400 nsec signal integration in PMT01 . . . 78
6.3 The waveform of 1p.e. signal and photon counting threshold . 79
6.4 Charge distributions of photoelectrons in CaF_2 and dark current 80
6.5 Signal overlapping in photon counting 81
6.6 Energy histograms with full integration and full photon counting 82
6.7 Charge of p.e. signals distributed by the timebin 84
6.8 Charge distribution at different timebin of CaF_2 signal 85
6.9 Sum waveform of 62 PMTs and waveform of one PMT 86
6.10 Spectra by partial photon counting before calibration 87
6.11 Spectra by partial photon counting after calibration 87
6.12 Fitting function to extract energy resolutions 88

6.13 Resolutions obtained by partial photon counting 89

7.1 Energy resolutions and acknowledged fluctuations 91
7.2 The remaining fluctuation 93
7.3 Fitting studied function for resolutions in Run010 95
7.4 Estimated resolutions at Q-value of ^{48}Ca 95

9.1 The decay time and light yield of CaF_2(pure) 101
9.2 Simulation spectrum of $0\nu\beta\beta$ and $2\nu\beta\beta$ of resolution $\sigma/Q_{\beta\beta}$ =0.8-0.9 % and $T^{0\nu}_{1/2}$=10^{27}year 102

C.1 Calculation reduction factor in digitization error 112

D.1 Linear coefficient of $\Delta_{\text{p.e.}}$ and Pedestal 114
D.2 signal points in 1p.e. signal as a function of obtained photo-electrons 115
D.3 Obtained widths of 1p.e. signals of 62 PMTs 116
D.4 Compare shapes of 1p.e. signals 116
D.5 Non-overlap and overlap of two 1p.e. signals 117
D.6 Reduced factor in estimation of digitization error 118
D.7 Profile of average pedestal of 62 PMTs in 1 year 120
D.8 Profile of normalized peak positions and normalized DEEP at ^{40}K and ^{208}Tl 121

E.1 The fluctuations of pedestal differences 128
E.2 The fluctuations accumulated in integration interval 129

F.1 Define SIGNAL INTERVAL in photon counting 131
F.2 Minimum intervals for counting photons of 62 PMTs 132

G.1 Correlation of counted p.e. with true p.e. using different thresholds 134

List of Tables

1.1 The three-flavor oscillation parameters from global data fitting 5
1.2 Q-value, natural abundance and half-life of $2\nu\beta\beta$ ($T^{2\nu}_{1/2}$) of different double-beta decay isotopes 11
1.3 Summary of the best lower limit of half-life of $0\nu\beta\beta$ of different isotopes 16

2.1 Characteristics of PMTs used in CANDLES 24
2.2 Compare CaF_2(Eu) scintillator used in ELEGANT VI and CaF_2(pure) scintillator 24
2.3 Compare the data format in CANDLES III (current) and Photon Counting (this thesis) 28
2.4 Series of CANDLES detector: current and future 33

3.1 Comparison of $2\nu\beta\beta$ background rate with different mass of ^{48}Ca and energy resolution using simulation 35

4.1 The statistical fluctuation ($\sigma_{\text{p.e.}}$), and all factors of baseline fluctuation (σ_{DE}, σ_{HF}, σ_{DC} and σ_{PedErr}) on energy resolutions. 62

7.1 The energy resolution and the contributing fluctuations (statistical, baseline and remaining fluctuations) at ^{40}K and ^{208}Tl 92
7.2 Estimated the sensitivity of $0\nu\beta\beta$ half-life of ^{48}Ca after improvement of energy resolution 96

9.1 Estimate energy resolution with cryogenic CaF_2(pure) and photon counting 102

Chapter 1

Neutrino mass and Double Beta Decay

1.1 Neutrino Physics

The Standard Model is the theory explaining the elementary particles (or the building blocks of physical matters) and three of four fundamental forces (electromagnetic, weak, and strong interactions). There are 12 elementary particles, which are be classified into two groups of fermions called quarks (with fractional charge) and leptons (with integer charge), and they are divided into three generations (I, II, and III) of 4 particles each. Figure 1.1 shows the 12 elementary fermions and the 4 fundamental bosons (Gluon, Photon, Z boson, W boson) meditating the forces.

Neutrino is one of the leptons with a neutral charge and assumed to be a mass-less particle in Standard Model. In correspondence to the three generations, there are three flavors of neutrinos called electron-neutrino (ν_e), muon-neutrino (ν_μ) and tau-neutrino (ν_τ). There are experimental evidence that neutrino can change from one flavor to another, and it is called neutrino oscillation (discussed in section 1.1.2). The neutrino oscillation indicates neutrino is a massive particle. Neutrino is a neutral charge and it interacts through weak interactions with small cross-section. It is challenging to study the properties of neutrino. Some predicted and obtained properties of neutrino can explore new physics beyond Standard Model. Hence, the physics and properties of neutrino are interesting topics in physics.

1.1.1 A brief history of neutrino

In 1914, J. Chadwick discovered the continuous spectrum of β-rays [2]. Without acknowledgment of neutrino, the continuous spectrum is not con-

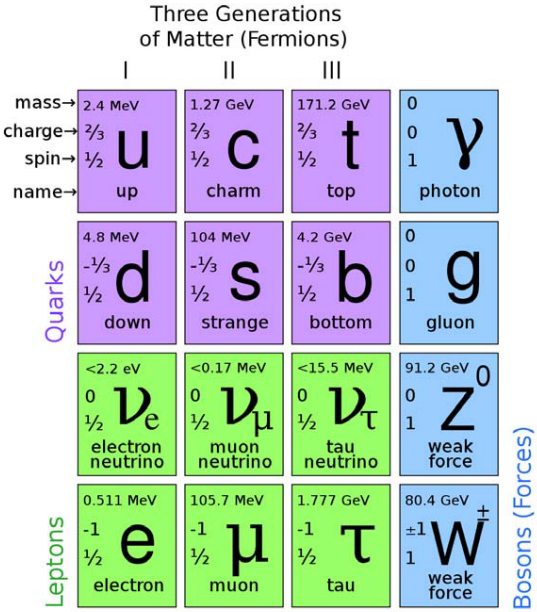

Figure 1.1: Elementary particles in Standard Model [1].

sistent with the theoretical expectation. In 1930, W. Pauli firstly postulated the idea of a neutral charge particle, which was then named neutrino, with the spin of 1/2 and a tiny mass in order to compensate for the conservation of energy and momentum. The idea worked well, and E. Fermi constructed the equations of interactions between neutrino and other particles. The theoretical equation of β-decay can be described as the following equation.

$$n \rightarrow p + e^- + \bar{\nu}_e \tag{1.1}$$

The three flavors of neutrino were obtained by experiments:

- The anti-electron-neutrino ($\bar{\nu}_e$) from β-decays inside a large reactor was detected at Los Alamos in 1956 by C. L. Cowan and F. Reines [3];
- In 1962, in Brookhaven accelerator, L. M. Lederman, M. Schwartz, and J. Steinberger confirmed the existence of muon neutrino (ν_μ) as a proof of two kinds of neutrino [4];
- The tau neutrino was discovered in 2000 by the DONUT collaboration at Fermilab using nuclear emulsion [5];
- In 2006, the LEP Electroweak Working Group (CERN) announced the number of neutrino flavors determined by the results of four LEP ex-

periments (ALEPH, DELPHI, L3, and OPAL) [6]. It is shown that there are three flavors lighter than Z_0.

After the discovery of neutrino, there were many experiments carried out to study cosmological objects using high penetration through the matter of neutrino. Neutrinos can be found from many sources, such as the Sun or atmosphere. There were two important studies of neutrinos, which signaled the disagreement between experimental and theoretical observations, and they are Solar Neutrino Deficit and Atmospheric Neutrino Anomaly. The disagreement of obtained and estimated results was later found due to the neutrino oscillation (discussed in section 1.1.2).

1.1.2 Neutrino oscillation

In this section, two problems of Solar neutrino and Atmospheric neutrino are recalled. The neutrino oscillation, which is the explanation for these two problems, is discussed. The relation of neutrino oscillation the neutrino mass is also briefly explained.

Solar Neutrino Deficit: One of the cosmological objects for studying neutrinos is the Sun. In the Sun, the nuclear fusion via proton-proton chain reactions produces a vast amount of emitted neutrinos, which are so-called Solar neutrinos. R. Davis and J. N. Bahcall carried out the Homestake experiment in order to count the number of Solar neutrinos [7]. However, the amount of neutrino flux obtained is one-third of the expected flux estimated from the luminosity of the Sun. The Solar Neutrino Deficit was a long-standing problem.

Atmospheric Neutrino Anomaly: The cosmic rays enter the Earth and bombard the atmospheric elements. The interactions generate many π mesons (and less abundant K mesons). These π decay into other particles (a $\mu^{\pm}$, an $e^{\pm}$, a ν_μ, a $\bar{\nu}_\mu$, and a ν_e or a $\bar{\nu}_e$). Consequently, there are 2 ($\nu_\mu + \bar{\nu}_\mu$) and 1 (ν_e or $\bar{\nu}_e$) for every π decay, and the expected ratio of $(\nu_\mu + \bar{\nu}_\mu)/(\nu_e + \bar{\nu}_e)$ is approximately 2. The Kamiokande Collaboration announced the disagreement of the observed and calculated ν_μ rates (85 events and 144 events, respectively), while the obtained result of ν_e is quite consistent with the calculated result [8].

To resolve these deficits, a phenomenon called neutrino oscillation was proposed by B. Pontecorvo [9]. In this phenomenon, the neutrino flavor can change from one flavor to another one ($\nu_e \leftrightarrow \nu_\mu$, $\nu_\mu \leftrightarrow \nu_e$, etc.). This phenomenon was then obtained by many experiments using different neutrino sources (e.g., nuclear reactors, accelerators). In 2015, T. Kajita in Super Kamiokande collaboration [10] and A. Donald in SNO collaboration

[11] were awarded the Nobel Prize in Physics for the discovery of neutrino oscillation, which implies the non-zero mass of neutrino [12]. The theory of neutrino oscillation was then elaborated by Z. Maki, M. Nakagawa, and S. Sakata with the neutrino mixing matrix, which is named the PMNS matrix. In this theory, each neutrino flavor eigenstate can be derived in the linear combination of mass eigenstates as the following equation:

$$\begin{pmatrix} \nu_e \\ \nu_\mu \\ \nu_\tau \end{pmatrix} = (U_{\alpha i}) \begin{pmatrix} \nu_1 \\ \nu_2 \\ \nu_3 \end{pmatrix} = \begin{pmatrix} U_{e1} & U_{e2} & U_{e3} \\ U_{\mu 1} & U_{\mu 2} & U_{\mu 3} \\ U_{\tau 1} & U_{\tau 2} & U_{\tau 3} \end{pmatrix} \begin{pmatrix} \nu_1 \\ \nu_2 \\ \nu_3 \end{pmatrix} \tag{1.2}$$

or

$$|\nu_\alpha\rangle = \sum_{i=1}^{3} U^*_{\alpha i} |\nu_i\rangle \tag{1.3}$$

where $|\nu_\alpha\rangle$ is the flavor eigenstate (α=e, μ, τ)

$|\nu_i\rangle$ is the mass eigenstate (i=1, 2, 3)

U is the 3×3 PMNS unitary matrix

The PMNS matrix is parameterized by three mixing angles (θ_{12}, θ_{23}, and θ_{13}) and a single-phase angle called δ_{CP} related to the Charge-Parity violations.

$$U = \begin{pmatrix} 1 & 0 & 0 \\ 0 & c_{23} & s_{23} \\ 0 & -s_{23} & c_{23} \end{pmatrix} \cdot \begin{pmatrix} c_{13} & 0 & s_{13}\mathrm{e}^{-\mathrm{i}\delta} \\ 0 & 1 & 0 \\ -s_{13}\mathrm{e}^{\mathrm{i}\delta} & 0 & c_{13} \end{pmatrix} \cdot \begin{pmatrix} c_{12} & s_{12} & 0 \\ -s_{12} & c_{12} & 0 \\ 0 & 0 & 1 \end{pmatrix} \cdot \mathcal{P} \tag{1.4}$$

where c_{ij} is $cos\theta_{ij}$

s_{ij} is $sin\theta_{ij}$

$\mathcal{P}$ is a diagonal matrix which depends on the nature of neutrino.

The $\mathcal{P}$ is identity if neutrino is a Dirac particle (particle and anti-particle are not identical), while it is $\mathcal{P}$=diag($e^{i\alpha_1}$,$e^{i\alpha_2}$,1) if neutrino is a Majorana particle (particle and anti-particle are identical). The probability for a neutrino changing its flavor to another is:

$$\begin{aligned} P(\nu_\alpha \to \nu_\beta) = \delta_{\alpha\beta} - 4\sum_{i<j} Re\left(U^*_{\alpha i}U_{\beta i}U_{\alpha j}U^*_{\beta j}\right) sin^2\left(\frac{\Delta m^2_{ij}L}{4E}\right) \\ +2\sum_{i<j} Im\left(U^*_{\alpha i}U_{\beta i}U_{\alpha j}U^*_{\beta j}\right) sin2\left(\frac{\Delta m^2_{ij}L}{4E}\right) \end{aligned} \tag{1.5}$$

where $\delta_{\alpha\beta}$ is the Kronecker delta ($\delta_{\alpha\beta}$=1 if $\alpha = \beta$, and $\delta_{\alpha\beta}$=0 if $\alpha \neq \beta$),

$\Delta m^2_{ij} = \left|m^2_i - m^2_j\right|$ is the mass-square difference,

E is the energy of the neutrino,

Table 1.1: The three-flavor oscillation parameters from global data fitting. The results shown in the upper (lower) section are obtained without (with) the Super-Kamiokande atmospheric data. The numbers in the 1st (2nd) column are obtained assuming Normal Hierarchy (Inverted Hierarchy). $\Delta m^2_{3l} = \Delta m^2_{31} > 0$ for NH and $\Delta m^2_{3l} = \Delta m^2_{32} < 0$ for IH [13].

		Normal Ordering (best fit)		Inverted Ordering ($\Delta\chi^2 = 6.2$)	
		bfp $\pm 1\sigma$	3σ range	bfp $\pm 1\sigma$	3σ range
without SK atmospheric data	$\sin^2\theta_{12}$	$0.310^{+0.013}_{-0.012}$	$0.275 \to 0.350$	$0.310^{+0.013}_{-0.012}$	$0.275 \to 0.350$
	$\theta_{12}/^\circ$	$33.82^{+0.78}_{-0.76}$	$31.61 \to 36.27$	$33.82^{+0.78}_{-0.76}$	$31.61 \to 36.27$
	$\sin^2\theta_{23}$	$0.558^{+0.020}_{-0.033}$	$0.427 \to 0.609$	$0.563^{+0.019}_{-0.026}$	$0.430 \to 0.612$
	$\theta_{23}/^\circ$	$48.3^{+1.1}_{-1.9}$	$40.8 \to 51.3$	$48.6^{+1.1}_{-1.5}$	$41.0 \to 51.5$
	$\sin^2\theta_{13}$	$0.02241^{+0.00066}_{-0.00065}$	$0.02046 \to 0.02440$	$0.02261^{+0.00067}_{-0.00064}$	$0.02066 \to 0.02461$
	$\theta_{13}/^\circ$	$8.61^{+0.13}_{-0.13}$	$8.22 \to 8.99$	$8.65^{+0.13}_{-0.12}$	$8.26 \to 9.02$
	$\delta_{\rm CP}/^\circ$	222^{+38}_{-28}	$141 \to 370$	285^{+24}_{-26}	$205 \to 354$
	$\frac{\Delta m^2_{21}}{10^{-5}\ \rm eV^2}$	$7.39^{+0.21}_{-0.20}$	$6.79 \to 8.01$	$7.39^{+0.21}_{-0.20}$	$6.79 \to 8.01$
	$\frac{\Delta m^2_{3\ell}}{10^{-3}\ \rm eV^2}$	$+2.523^{+0.032}_{-0.030}$	$+2.432 \to +2.618$	$-2.509^{+0.032}_{-0.030}$	$-2.603 \to -2.416$
		Normal Ordering (best fit)		Inverted Ordering ($\Delta\chi^2 = 10.4$)	
		bfp $\pm 1\sigma$	3σ range	bfp $\pm 1\sigma$	3σ range
with SK atmospheric data	$\sin^2\theta_{12}$	$0.310^{+0.013}_{-0.012}$	$0.275 \to 0.350$	$0.310^{+0.013}_{-0.012}$	$0.275 \to 0.350$
	$\theta_{12}/^\circ$	$33.82^{+0.78}_{-0.76}$	$31.61 \to 36.27$	$33.82^{+0.78}_{-0.75}$	$31.61 \to 36.27$
	$\sin^2\theta_{23}$	$0.563^{+0.018}_{-0.024}$	$0.433 \to 0.609$	$0.565^{+0.017}_{-0.022}$	$0.436 \to 0.610$
	$\theta_{23}/^\circ$	$48.6^{+1.0}_{-1.4}$	$41.1 \to 51.3$	$48.8^{+1.0}_{-1.2}$	$41.4 \to 51.3$
	$\sin^2\theta_{13}$	$0.02237^{+0.00066}_{-0.00065}$	$0.02044 \to 0.02435$	$0.02259^{+0.00065}_{-0.00065}$	$0.02064 \to 0.02457$
	$\theta_{13}/^\circ$	$8.60^{+0.13}_{-0.13}$	$8.22 \to 8.98$	$8.64^{+0.12}_{-0.13}$	$8.26 \to 9.02$
	$\delta_{\rm CP}/^\circ$	221^{+39}_{-28}	$144 \to 357$	282^{+23}_{-25}	$205 \to 348$
	$\frac{\Delta m^2_{21}}{10^{-5}\ \rm eV^2}$	$7.39^{+0.21}_{-0.20}$	$6.79 \to 8.01$	$7.39^{+0.21}_{-0.20}$	$6.79 \to 8.01$
	$\frac{\Delta m^2_{3\ell}}{10^{-3}\ \rm eV^2}$	$+2.528^{+0.029}_{-0.031}$	$+2.436 \to +2.618$	$-2.510^{+0.030}_{-0.031}$	$-2.601 \to -2.419$

L is the distance from the neutrino source to the detector.

The probability in equation 1.5 is called the survival probability with $\alpha = \beta$. The neutrino mixing angles θ_{ij} and the mass-square difference Δm^2_{ij} can be determined from a measurement of survival probability. Table 1.1 shows the Oscillation Parameters from global data fitting [13].

1.1.3 Neutrino mass

In Standard Model, neutrinos are assumed as mass-less particles. The discovery of neutrino oscillation (section 1.1.2) is proof that neutrino is a massive particle. However, the absolute value of neutrino mass is still a puzzle for physicists. In this section, the different approaches for measuring the neutrino mass are introduced.

From Neutrino Oscillation experiments: The survival probability of $\nu_{e,\mu,\tau}$ can help us determine the mass-square difference ($|m_i^2 - m_j^2|$). Additionally, the mass hierarchy is not confirmed. There are 3 orders of neutrino mass eigenstates (m_1, m_2 and m_3):

- Normal Hierarchy (NH): the order is $m_1 < m_2 < m_3$,
- Inverted Hierarchy (IH): the order is $m_3 < m_2 < m_1$,

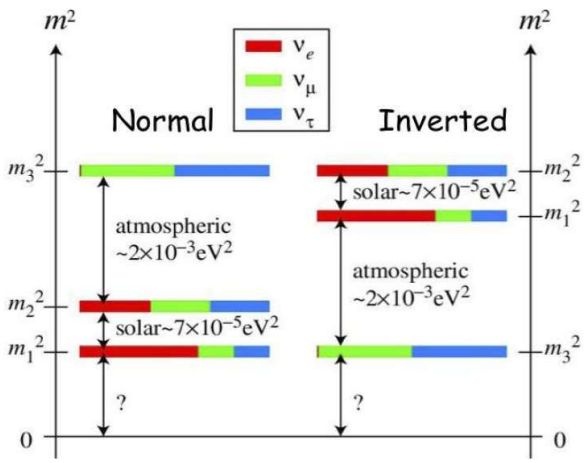

Figure 1.2: Neutrino Mass Hierarchy [14] in Normal Hierarchy and Inverted Hierarchy. Based on (atmospheric and solar) neutrino experiments, Δm^2_{ij} can be determined, but the absolute value of neutrino is still unknown.

- Quasi-Degenerate (QD): the order is $m_1 \approx m_2 \approx m_3$.

The Normal Hierarchy and Inverted Hierarchy (with data from neutrino oscillation experiments) are shown in Figure 1.2.

From Cosmology: The data from Cosmology Microwave Background (CMB) can be used to probe the upper limit of the sum of neutrino masses. In 2019, the Planck Collaboration reported the following upper limit of the sum of neutrino mass [15]:

$$\sum = \sum_i m_i < 0.12 \text{ eV } (95 \text{ \% C.L.})$$

From Direct Measurement: This direct measurement is also named the Kurie-plot experiment. At the endpoint (near Q-value) of a continuous spectrum of β-decay, the spectrum of β-ray in case of $m(\nu) = 0$ is different from the spectrum of β-ray in case of $m(\nu) \neq 0$. ^{3}H is the preferred isotope for the direct measurement of neutrino mass because of its small Q-value; hence, the effect of neutrino mass on the energy spectrum is more significant. Figure 1.3 shows the energy spectrum of β-decay from ^{3}H in cases of $m(\nu_e) = 0$ eV and $m(\nu_e) = 1$ eV. The Karlsruhe Tritium Neutrino Experiment (KATRIN) aims to observe the neutrino mass interpreted from the energy spectrum of ^{3}H using high resolution magnetic adiabatic collimation with electrostatic filtering. In September 2019, the KATRIN collaboration reported the upper limit of electron neutrino mass [17]:

$$m_\beta = \sqrt{\sum_i |U_{ei}|^2 m_i^2} < 1.1 \text{ eV } (90 \text{ \% of C.L.})$$

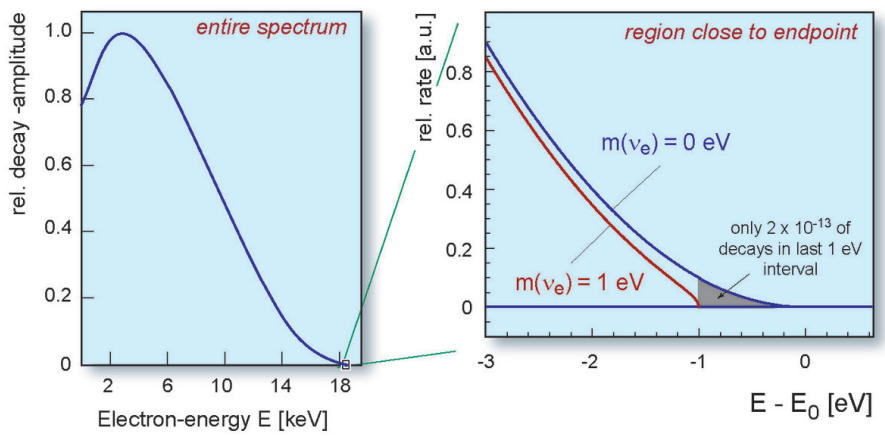

Figure 1.3: Energy spectrum of β-decay from ^{3}H [16]. If neutrino-mass is non-zero, there is a difference at the end-point of the spectrum.

From Double Beta Decay experiment: The measurement for neutrino-less double beta decay probes the effective neutrino mass, and it is proof that neutrino is a Majorana particle. In the neutrino-less double beta decay, the mass of neutrino depends on the half-life of neutrino-less double beta decay and the nuclear matrix element. The nuclear matrix element depends on the nuclear model; however, the correct model to explain the neutrino-less double beta decay is still not confirmed. Additionally, the effective neutrino mass can be plotted as a function of the lightest neutrino. Figure 1.4 shows the effective neutrino mass as a function of the lightest neutrino in 3 hierarchies: QD, NH, and IH. Thus, by determination of the effective neutrino mass, one can also confirm the mass hierarchy.

1.2 Double Beta Decay

In this section, the phenomenon of double beta decay is introduced. There are two decay modes can occur: two-neutrino double beta decay and neutrino-less double beta decay. The neutrino-less double beta decay can help us determine the neutrino mass and explore the new physics beyond the Standard Model.

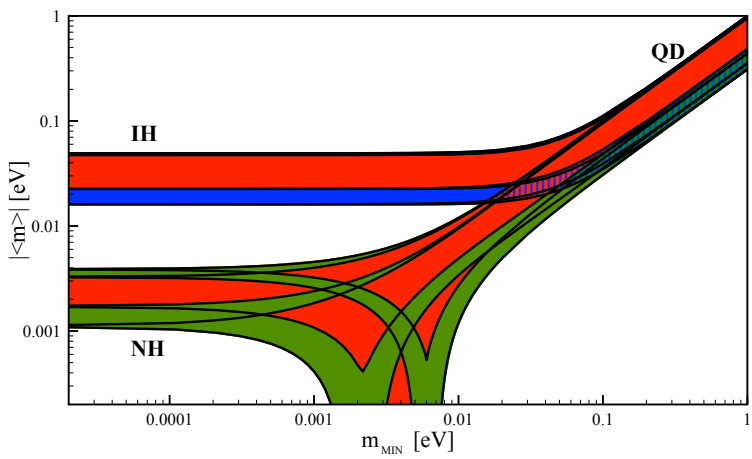

Figure 1.4: The value of effective neutrino mass can be plotted theoretically as a function of the lightest neutrino (the picture is on page 250 of reference [18]), including the 2σ uncertainty. Three ranges are corresponding to 3 neutrino mass hierarchies: Quasi-Degenerated (QD), Normal Hierarchy (NH), and Inverted Hierarchy (IH).

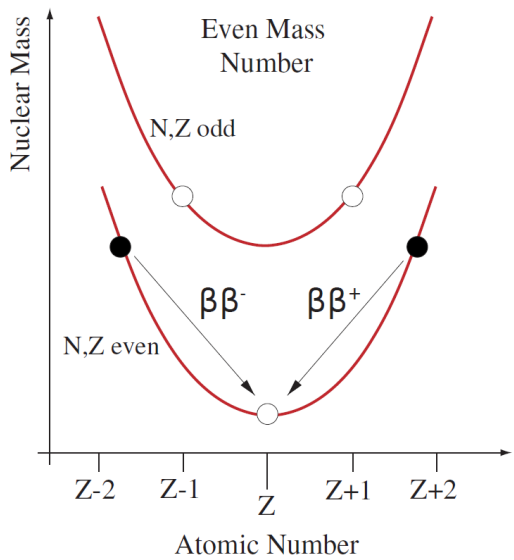

Figure 1.5: Mass of isobaric nuclei as a function of atomic number[19].

1.2.1 Two-Neutrino Double Beta Decay ($2\nu\beta\beta$)

The semi-empirical mass formula was introduced by Weizsacker to calculate the mass of a nucleus based on the liquid-drop model. The mass of isobaric nuclei can be plotted as a function of the atomic number. With isobaric nuclei whose atomic mass is even, the pairing term of the Weizsacker formula is negative for even-even nuclei and positive for odd-odd nuclei. Therefore, the semi-empirical mass formula can be plotted into two curves, as shown in Figure 1.5. The nucleus with the lowest nuclear mass is stable, and the other unstable nuclei will reach to this nucleus via $\beta^{\pm}$ transitions. The single β is sometimes energetically forbidden, for instance, the transition from (A, Z±2) to (A, Z±1); on the other hand, the transitions from (A, Z±2) to (A, Z) is energetically allowed. This phenomenon is named Double Beta Decay with the nuclear decay equations:

$$ {}^{A}_{Z-2}X \rightarrow {}^{A}_{Z}X + 2e^{-} + 2\bar{\nu}_e \tag{1.6} $$

The phenomenon was proposed by theoretical physicist M. Goeppert Mayer [20], and, later then, it was obtained in more than ten radioisotopes. Since there are $2\bar{\nu}_e$ emitted together with $2\beta^{-}$, it is usually called two-neutrino double beta decay ($2\nu\beta\beta$).

There are 35 isotopes acting as double beta decay sources. Since the double beta decay is a weak process with a scarce decay rate, there are three primary considerations to choose a double beta decay source in practice [21]:

- Q-value: In a rare decay experiment, background is a essential problem. The Q-value far from energies of natural background can help reduce the background.
- Isotopic abundance together with the available enrichment techniques: The rare decay rate can be compensated with the natural abundance of the isotopes (such as ^{130}Te with 34 % natural abundance) or the available techniques for enrichment (such as ^{136}Xe or ^{76}Ge).
- Compatibility with available detection techniques.

Figure 1.6 shows the Q-value of different double beta decay isotopes, and 2 dashed lines are the energies of the background from ^{208}Tl and ^{214}Bi. The red points are the 9 isotopes, which are named "the magnificent nine", commonly used as double beta decay sources because of their experimental advantages. Table 1.2 shows the half-life of $2\nu\beta\beta$ ($T^{2\nu}_{1/2}$) of different isotopes. The results are taken from different experiments.

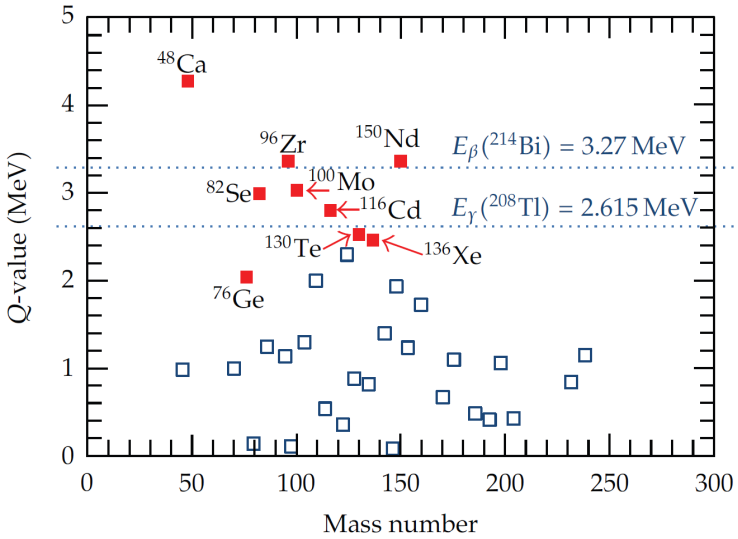

Figure 1.6: Q-value of various double beta decay isotopes [21]. The current isotopes used in experiments are marked with red squares. Two blue dashed lines are used to indicate the highest energies of γ-decay and β-decay from natural background.

Table 1.2: Q-value, natural abundance, and half-life of $2\nu\beta\beta$ ($T^{2\nu}_{1/2}$) of different double-beta decay isotopes. $T^{2\nu}_{1/2}$ values are taken from different experiments.

Isotope	**Q-value** (MeV)	**Abundance** (%)	$\mathbf{T^{2\nu}_{1/2}}$ (10^{19} year)
^{48}Ca	4.272	0.187	$4.3\pm^{2.4}_{1.1}$(stat.)±1.4(sys.) [22]
^{76}Ge	2.039	7.8	184^{+9}_{-8}(stat.)$^{+11}_{-6}$(sys.) [23]
^{82}Se	2.998	9.2	9.6±0.3(stat.)±1.0(sys.) [25]
^{96}Zr	3.348	2.8	2.35±0.14(stat.)±0.16(sys.) [24]
^{100}Mo	3.035	9.6	0.711±0.002(stat.)±0.054(sys.) [26]
^{116}Cd	2.809	7.6	2.88±0.04(stat.)±0.16(sys.) [26]
^{130}Te	2.527	34.08	70±9(stat.)±11(sys.) [27]
^{136}Xe	2.459	8.9	216.5±1.6(stat.)±5.9(sys.) [28]
^{150}Nd	3.371	5.6	$184^{+0.025}_{-0.022}$(stat.)±0.63(sys.) [29]

1.2.2 Neutrino-less Double Beta Decay ($0\nu\beta\beta$)

Beside the $2\nu\beta\beta$, there is an alternative decay mode named Neutrino-less Double Beta Decay ($0\nu\beta\beta$). The $0\nu\beta\beta$ is the phenomenon when (A, Z) decay into (A, Z+2) without the emission of anti-neutrinos. In this $0\nu\beta\beta$, the emitted anti-neutrino can be converted into a neutrino, and they are absorbed inside the atomic nucleus. The equation of $0\nu\beta\beta$ is:

$$^{A}_{Z-2}X \rightarrow^{A}_{Z} X + 2e^{-} \tag{1.7}$$

Figure 1.7 shows the Feynman diagrams of $0\nu\beta\beta$ and $2\nu\beta\beta$. The lepton number (ΔL=$N^{After}_{Lepton} - N^{Before}_{Lepton}$) is not conserved in $0\nu\beta\beta$, hence, this process is not allowed in Standard Model. The $0\nu\beta\beta$ is an exciting topic which can answer crucial questions for physicists:

(i) Determine the neutrino mass: The neutrino mass depends on the half-life of $0\nu\beta\beta$ and the nuclear matrix element. It is explained more details in the following section.

(ii) Confirm the nature of neutrino: The detection of $0\nu\beta\beta$ occurs if the neutrino is a Majorana particle. Thus, $0\nu\beta\beta$ is a way to probe whether neutrino is a Majorana particle (particle=antiparticle) or a Dirac particle (particle≠antiparticle).

(iii) Explore new Physics beyond the Standard Model: In $0\nu\beta\beta$, there is a lepton number conservation violation, which is not allowed in Standard Model. Therefore, $0\nu\beta\beta$ is a tool to explore the new Physics.

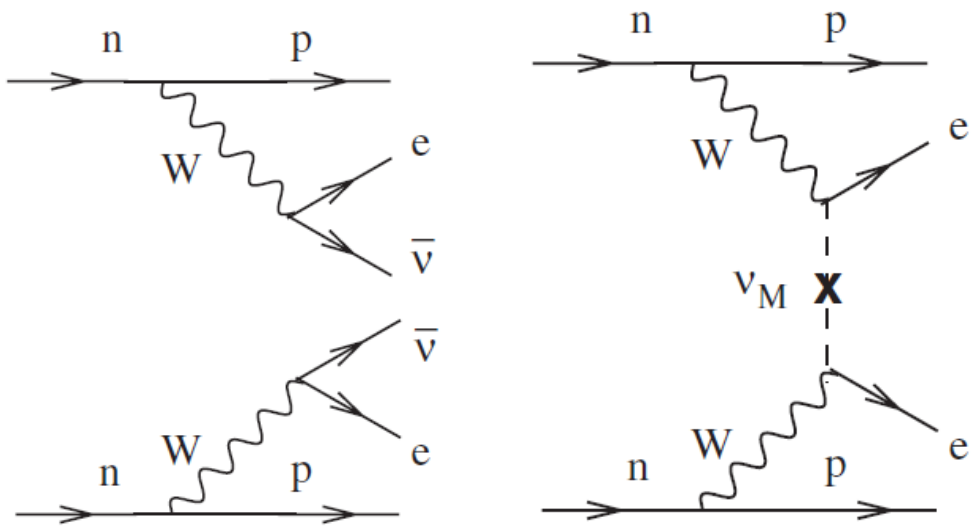

(a) $2\nu\beta\beta$ (ΔL=0)
$^{A}_{Z-2}X \rightarrow ^{A}_{Z}X + 2e^- + 2\bar{\nu}_e$

(b) $0\nu\beta\beta$ (ΔL=2)
$^{A}_{Z-2}X \rightarrow ^{A}_{Z}X + 2e^- \cancel{+ 2\bar{\nu}_e}$

Figure 1.7: The diagrams of beta decays [30]. The left figure is the diagram of the $2\nu\beta\beta$ with emission of 2 $\bar{\nu}_e$, and the right figure is the diagram of the $0\nu\beta\beta$ without emission of $\bar{\nu}_e$. The Lepton number is conserved in $2\nu\beta\beta$ (ΔL=0), but not conserved in $0\nu\beta\beta$ (ΔL=2).

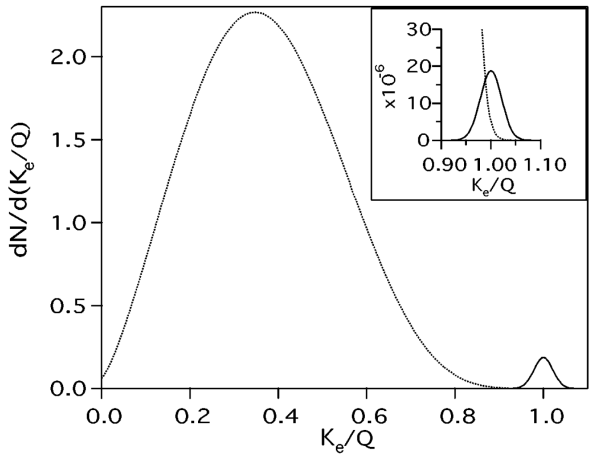

Figure 1.8: Spectrum of kinetic energy of $2e^-$ [31]. The kinetic energy is normalized to Q-value. The $2\nu\beta\beta$ spectrum is continuous, but the $0\nu\beta\beta$ spectrum is mono-energetic.

■ **Determination of neutrino mass from $0\nu\beta\beta$**

The $2\nu\beta\beta$ can be explained as two single β-decay processes. In $2\nu\beta\beta$, a portion of the released energy is carried away by $2\bar{\nu}_e$, thus, the obtained $2e^-$ spectrum in $2\nu\beta\beta$ is continuous. On the other hand, in $0\nu\beta\beta$, since there is no emission of $\bar{\nu}_e$, the $2e^-$ energy spectrum in $0\nu\beta\beta$ is a mono-energetic peak at Q-value. The half-life of $0\nu\beta\beta$ can be parameterized as [32] [33]:

$$(T_{1/2}^{0\nu})^{-1} = G^{0\nu} \left| \frac{\langle m_{\beta\beta} \rangle^2}{{m_e}^2} \right| \left| M^{0\nu} \right|^2 \tag{1.8}$$

where $G^{0\nu}$ is phase-space factor, $M^{0\nu}$ is nuclear matrix element, and m_e is electron mass. The $\langle m_{\beta\beta} \rangle$ is effective neutrino mass, which is defined as:

$$\langle m_{\beta\beta} \rangle = \left| \sum_{i=1}^{3} U_{ei}^2 m_i \right| \tag{1.9}$$

where U_{ei} is the PMNS matrix for Majorana neutrinos, and m_i is the eigenvalue of the ith neutrino mass eigenstate. Therefore, evaluation of the half-life of $0\nu\beta\beta$ ($T_{1/2}^{0\nu}$) is an essential step to calculate the effective neutrino mass.

In the equation 1.8, the values of $G^{0\nu}$ and m_e are well determined. However, besides the $T_{1/2}^{0\nu}$, the nuclear matrix element (NME) is not known either because of the unknown mechanism of $0\nu\beta\beta$. There are several theoretical structures proposed to calculate the NME for $0\nu\beta\beta$: Large-Scale Shell Model (LSM) [34], Energy Density Functional (EDF) [35], Interacting Boson Model (IBM) [36], Quasiparticle Random-Phase Approximation (QRPA) [37], etc. The different results of NMEs from these approaches cause a deviation of neutrino mass (as shown in Figure 1.9).

1.3 Status of some $0\nu\beta\beta$ experiments

The $0\nu\beta\beta$ is extremely rare, and it has not been observed in any experiments. Since $0\nu\beta\beta$ is an interesting topic in nuclear and particle physics, there are many experiments in over the world trying to prove this phenomenon from different isotopes using different experimental approaches. In this section, the most stringent results of the "magnificent nine" are indicated. The list is sorted in the other of the atomic mass number.

•**^{48}Ca with $Q_{\beta\beta}$=4.3 MeV:** The current best limit $0\nu\beta\beta$ of ^{48}Ca was reported by the 6th generation of ELEctron GAmma-ray Neutrino Telescope (ELEGANT-VI) experiment in 2008 [39]:

$$T_{1/2}^{0\nu}(^{48}\mathrm{Ca}) \ > \ 5.8 \times 10^{22} \text{ year} \quad (90\% \text{ C.L.}) \tag{1.10}$$

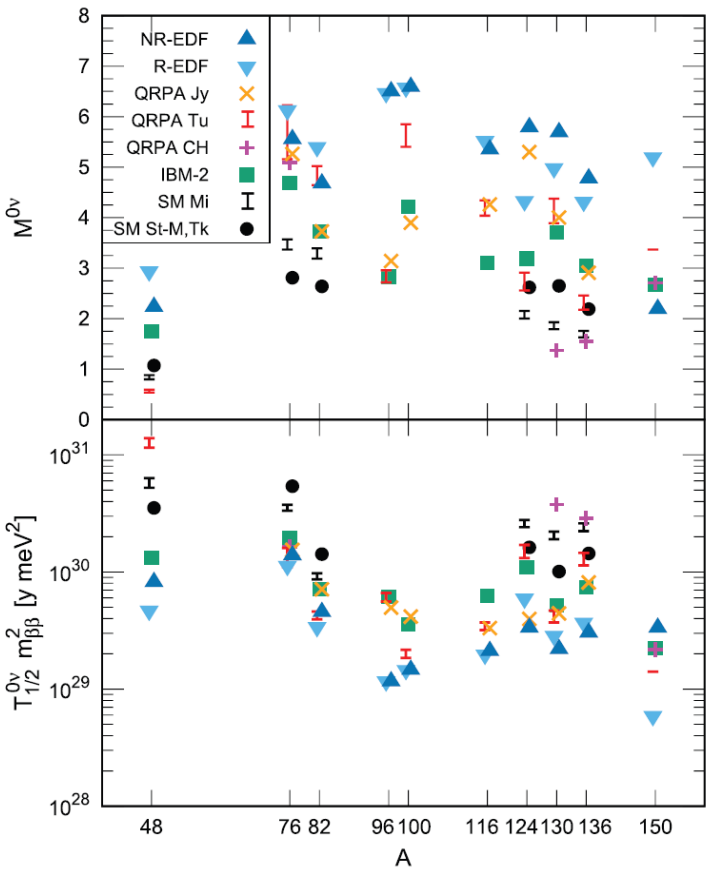

Figure 1.9: The Nuclear Matrix Element of $0\nu\beta\beta$ (top) and the half-life of $0\nu\beta\beta$. The half-life is scaled by the effective neutrino mass and is plotted as a function of atomic mass [38] using different nuclear matrix elements.

The experiment was carried out at the Oto Cosmo Observatory, whose vertical depth is 1400 m.w.e, and the non-enriched CaF_2(Eu) crystals were used as detector and source. The total amount of ^{48}Ca was 7.6 g, and the exposure was reported as 3394 kg·day (for data in 2008) combined with 1553 kg·day (for data in 2004). However, the world-best limit of ^{48}Ca may be taken over by the CANDLES collaboration according to a preliminary result of the better limit in 2018 [40]:

$$T^{0\nu}_{1/2}(^{48}\mathrm{Ca}) \ > \ 6.2 \times 10^{22} \text{ year} \tag{1.11}$$

•**^{76}Ge with $Q_{\beta\beta}$=2.0 MeV:** The Germanium Detector Array (GERDA) experiment is set up at the Gran Sasso National Laboratories, in which the vertical depth is 3500 m.w.e, to obtain the $0\nu\beta\beta$ from ^{76}Ge. They deploy 37 high purity ^{76}Ge-enriched (from 7.8 % to 85 %) detectors whose total mass is

35.6 kg. They experimented with the exposure of 82.4 kg·year, and reported the most stringent half-life limit in 2019 [41]:

$$T^{0\nu}_{1/2}(^{76}\text{Ge}) \ > \ 0.9 \times 10^{26} \text{ year} \quad (90\% \text{ C.L.}) \tag{1.12}$$

•**^{82}Se with $Q_{\beta\beta}$=3.0 MeV:** The CUPID-0 Collaboration reports the best limit of $0\nu\beta\beta$ of ^{82}Se carried out at the Gran Sasso National Laboratories. The CUPID, which is the acronym of CUORE Upgrade with Particle Identification, is the successor of the Cryogenic Underground Observatory for Rare Events (CUORE) experiment. The CUPID collaborators use the scintillating bolometers, which enhance the Particle Identification ability to eliminate the α background from the detector surfaces. In the latest report published in 2019, with a total exposure of 5.29 kg·year, they set a world most stringent limit in search of $0\nu\beta\beta$ half-life of ^{82}Se [43]:

$$T^{0\nu}_{1/2}(^{82}\text{Se}) \ > \ 3.5 \times 10^{24} \text{ year} \quad (90\% \text{ C.L.}) \tag{1.13}$$

•**^{96}Zr with $Q_{\beta\beta}$=3.3 MeV:** The international collaboration named Neutrino Ettore Majorana Observatory (NEMO-3), which is located at the Modane Underground Laboratory (4800 m.w.e), reported the most stringent lower limit of ^{96}Zr. The two main components of the detector are the scintillator blocks, which work as a calorimeter, and the drift cells, which work as a tracking chamber. The NEMO-3 detector holds more than 10 kg of isotopes, which are prepared as source foil. The source foils are surrounded by these factors to obtain the energy and particle trajectory, which is used to discriminate the β^- with other particles. The world best limit of ^{96}Zr $0\nu\beta\beta$ with the exposure of 0.031 kg·year was reported in 2010 [44]:

$$T^{0\nu}_{1/2}(^{96}\text{Zr}) \ > \ 9.2 \times 10^{21} \text{ year} \quad (90\% \text{ C.L.}) \tag{1.14}$$

•**^{100}Mo with $Q_{\beta\beta}$=3.0 MeV:** The NEMO-3 collaborators aimed to obtain the $0\nu\beta\beta$ from 7 DBD isotopes. They set three world best limits for the search of $0\nu\beta\beta$ half-life limits of ^{96}Zr, which as aforementioned, ^{100}Mo, and ^{150}Nd. For ^{100}Mo, with the exposure of 34.3 kg·year, the most stringent lower limit was set in 2015 [45]:

$$T^{0\nu}_{1/2}(^{100}\text{Mo}) \ > \ 1.1 \times 10^{24} \text{ year} \quad (90\% \text{ C.L.}) \tag{1.15}$$

•**^{116}Cd with $Q_{\beta\beta}$=2.8 MeV:** The Aurora experiment at the Gran Sasso National Laboratory aims to obtain the $0\nu\beta\beta$ of ^{116}Cd. With the help of 1.162 kg of $^{116}CdWO_4$ scintillator crystals measured in 35324 hours, the Aurora collaborators currently set the world best limit of the $0\nu\beta\beta$ half-life of ^{116}Cd in 2018 [46]:

$$T^{0\nu}_{1/2}(^{116}\text{Cd}) \ > \ 2.2 \times 10^{23} \text{ year} \quad (90\% \text{ C.L.}) \tag{1.16}$$

Table 1.3: Summary of the best lower limit of the half-life of $0\nu\beta\beta$ of different isotopes with 90 % Confidence Level. The list is made in the order of the increment of atomic mass.

Isotope	$\mathbf{T^{0\nu}_{1/2}}$ **limit (year)**	$\langle \mathbf{m_{\beta\beta}} \rangle$ **limit (eV)**	**Experiment & Published Year**
^{48}Ca	$> 5.8\times10^{22}$	<(3.5-22)	ELEGANT-VI (2008) [39]
^{76}Ge	$> 0.9\times10^{26}$	<(0.104-0.228)	GERDA (2019) [41]
^{82}Se	$> 3.5\times10^{24}$	<(0.311-0.638)	CUPID-0 (2019) [43]
^{96}Zr	$> 9.2\times10^{21}$	<(7.2-19.5)	NEMO3 (2010) [44]
^{100}Mo	$> 1.1\times10^{24}$	<(0.33-0.62)	NEMO3 (2015) [45]
^{116}Cd	$> 2.2\times10^{23}$	<(1.0-1.7)	Aurora (2018) [46]
^{130}Te	$> 1.5\times10^{25}$	<(0.11-0.52)	CUORE (2018) [47]
^{136}Xe	$> 1.07\times10^{26}$	<(0.061-0.165)	KamLAND-Zen (2016) [48]
^{150}Nd	$> 2.0\times10^{22}$	<(1.6-5.3)	NEMO3 (2016) [49]

•**^{130}Te with $Q_{\beta\beta}$=2.5 MeV:** The CUORE, which is aforementioned in the world-best limit of ^{82}Se, aims to obtain the $0\nu\beta\beta$ from ^{130}Te using 988 TeO_2 crystals, each having a mass of 750 g. In 2018, with the total exposure of 86.3 kg·year, the CUORE set the world best limit of ^{130}Te $0\nu\beta\beta$ [47]:

$$T^{0\nu}_{1/2}(^{130}\text{Te}) \;>\; 1.5 \times 10^{25} \text{ year} \quad (90\% \text{ C.L.}) \tag{1.17}$$

•**^{136}Xe with $Q_{\beta\beta}$=2.5 MeV:** Kamioka Liquid Scintillator Antineutrino Detector - Zero Neutrino Double β-Decay (KamLAND-Zen) obtained The most stringent limit of ^{136}Xe was reported in 2016 [48]:

$$T^{0\nu}_{1/2}(^{136}\text{Xe}) \;>\; 1.07 \times 10^{26} \text{ year} \quad (90\% \text{ C.L.}) \tag{1.18}$$

The experiment was carried out with enriched ^{136}Xe-loaded liquid scintillator, and the above result was obtained with by a combined exposure of 593.5 kg·year.

•**^{150}Nd with $Q_{\beta\beta}$=3.4 MeV:** The best lower limit of ^{150}Nd was reported by NEMO-3 collaboration in 2016 with the exposure of 5.25 kg·year [49]:

$$T^{0\nu}_{1/2}(^{150}\text{Nd}) \;>\; 2.0 \times 10^{22} \text{ year} \quad (90\% \text{ C.L.}) \tag{1.19}$$

• **Summary:** The world-best limits of the half-lives of $0\nu\beta\beta$ from different isotopes are reported in Table 1.3. The final goal of $0\nu\beta\beta$ experiments is to probe the effective Majorana neutrino mass. Consequently, the upper limit of effective neutrino mass denoted from the experiments are compared. The corresponding effective neutrino masses are also reported in Table 1.3.

So far, the KamLAND-Zen experiment has set the world best upper limit of the effective neutrino mass [48]:

$$\text{world-best sensitivity (2016): } \langle m_{\beta\beta} \rangle < \text{(61-165) meV}$$

This upper limit is just above the Inverted Hierarchy region in Figure 1.4. A very close limit was reported by GERDA collaborators in 2019 by combining the effective neutrino mass limits of ^{76}Ge, ^{82}Se, ^{130}Te and ^{136}Xe in different experiments [42]:

$$\text{combined sensitivity (2019): } \langle m_{\beta\beta} \rangle < \text{(66-155) meV}$$

In the next generations of many experiments, researchers aim to achieve the sensitivity below the inverted hierarchy (about 20 meV). The isotope enrichment and tons scale detector are prepared in order to achieve this sensitivity. CANDLES experiment, which is the main object of this thesis, is also under development process to improve the sensitivity.

Chapter 2

CANDLES experiment

This chapter covers the details setup of the current CANDLES III detector as well as the merit and demerit when using ^{48}Ca as the research target. Because the background is an essential factor when carrying out the neutrinoless double beta decay, the current dominant background candidates (near the Q-value region of ^{48}Ca) are discussed together with the background reduction methods. Furthermore, the goals to achieve the better upper limits of $T^{0\nu}_{1/2}(^{48}\mathrm{Ca})$ in association with the techniques and methodologies of the present and future generations of CANDLES detector are indicated.

2.1 Introduction of CANDLES

CANDLES is the acronym of **CA**lcium fluoride for studies of **N**eutrino and **D**ark matters by **L**ow **E**nergy **S**pectrometer. CANDLES is the successor of ELEGANT VI [39] experiment with the same target is to obtain the $0\nu\beta\beta$ from ^{48}Ca. The decay scheme of ^{48}Ca is shown in Figure 2.1. The Q-value for Double Beta Decay transition ($Q_{\beta\beta-}$) of ^{48}Ca is 4272 keV, which is the highest Q-value among all of double beta decay isotopes (Figure 1.6). This is the biggest advantage when using this isotope as the target of experiment because its Q-value is much higher than most of the natural background from γ-decay, the highest one is $E_\gamma(^{208}\mathrm{Tl}) = 2614.5$ keV, or β-decay, the highest one is $E_\beta(^{214}\mathrm{Bi}) = 3270$ keV. Only a few decays from the natural background can dominate as the background in the Q-value region (this will be discussed in section 2.3). With this advantage, the CANDLES experiment targets to carry the zero-background measurement. Background reduction has been carried out so far to achieve the goal.

Although the highest Q-value is the great advantage for background free environment, ^{48}Ca has a disadvantage, which is its low natural abundance. As

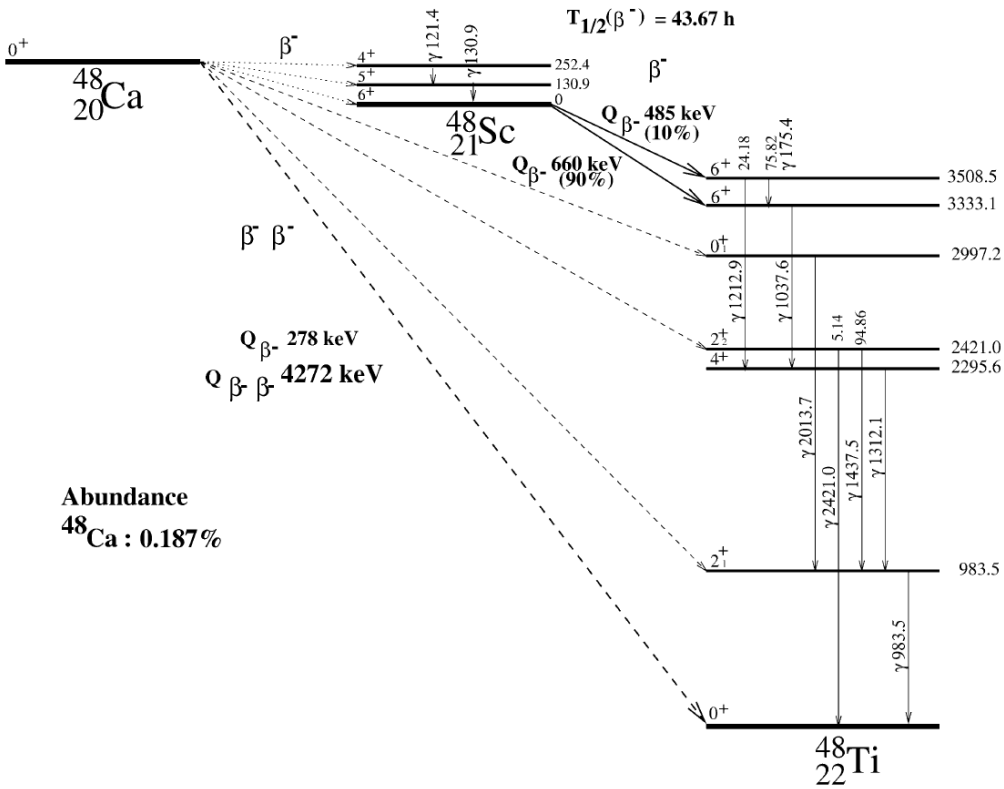

Figure 2.1: Decay scheme of ^{48}Ca [50]. The dashed lines are possible Double Beta Decay transitions from ^{48}Ca to ^{48}Ti.

we can see in Table 1.2, the natural abundance of ^{48}Ca is very low (0.187%). The low abundance limits the sensitivity of the measurement. CANDLES collaboration is studying the cost-effective methods for enrichment of ^{48}Ca (indicated in section 2.4) to compensate for the low abundance.

2.2 Detector setup

2.2.1 Kamioka Underground Observatory

Obtaining the $0\nu\beta\beta$ from ^{48}Ca is a big challenge due to the extremely rare decay rate ($T^{0\nu}_{1/2} > 5.8\times10^{22}$ year [39]). Therefore, the experiment requires an intense amount of source and a low-background environment. For a low background environment, CANDLES is set up in the Kamioka Underground Observatory at 1,000 m underground (2,700 m.w.e) in the Kamioka Mine,

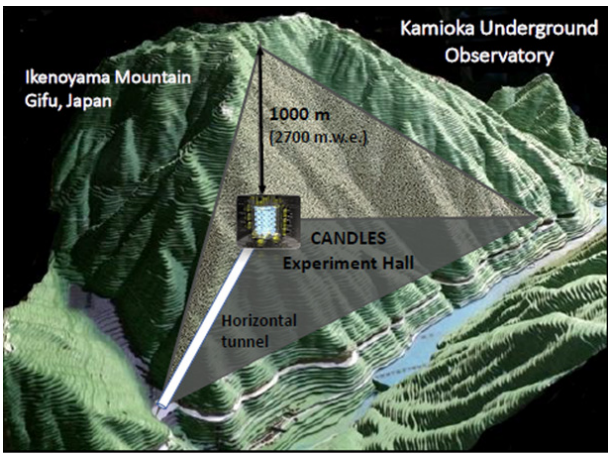

Figure 2.2: CANDLES experiment in Kamioka Underground Observatory, Ikenoyama Mountain, Gifu Prefecture, Japan [52].

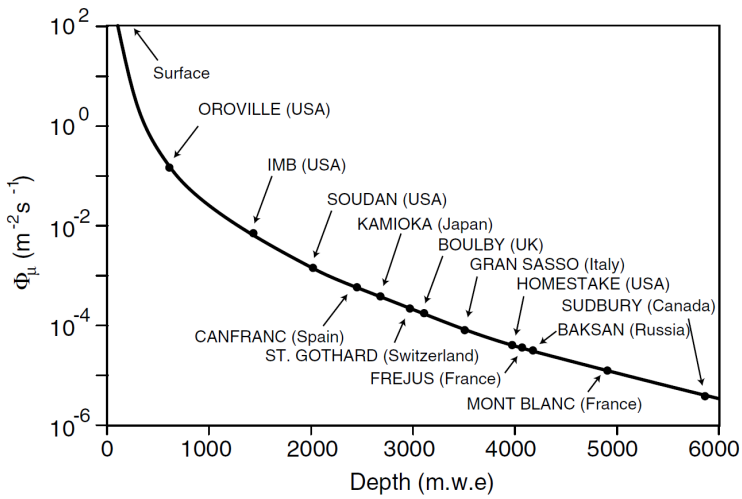

Figure 2.3: The muon flux as a function of vertical depth of different underground observatories in the world [53].

Ikenoyama Mountain, Gifu prefecture (Figure 2.2). The muon flux from cosmic-ray is reduced as a function of vertical depth (Figure 2.3). At a depth of 2,700 m.w.e, the muon flux is about 10^{-5} of the surface flux [51]. With large reduction of muon flux, other experiments (such as Super-Kamiokande [10] and Kam-LAND [48]) are also situated there.

2.2.2 Detector setup

As a scale-up version of ELEGANT VI in which 7.6 g of ^{48}Ca is used, we use much more amount of ^{48}Ca for $0\nu\beta\beta$ research. In plan, there are 5 generations of CANDLES detector:

- CANDLES-I and CANDLES-II are prototype detectors [54].
- CANDLES-III is the **current generation** (this thesis).
- CANDLES-IV and CANDLES-V are the future generations with improved sensitivities (section 2.5).

Figure 2.4 shows the current setup of CANDLES III detector. CANDLES detector consists of 96 cubic crystals of source-and-detector CaF_2(pure) with side lengths of 10 cm. The crystals are mounted in a jig with six levels and 16 crystals per level in total (Figure 2.5). The total mass of CaF_2 is about 305 kg; and the total amount of ^{48}Ca is nearly 350 g. These crystals are submerged within a vessel containing 2,000 liters of the liquid scintillator (LS). The decay constants of LS and CaF_2 are about 10 nsec and 1 μsec, respectively. With the difference between the pulse shapes, the LS can be used as an active shielding. Scintillation photons from LS and CaF_2 are collected by 62 Photo Multiplier Tubes (PMTs) surrounding the vessel, and each PMT is connected to one FADC. The layout of 62 PMTs is shown in Figure 2.6, and the characteristics of the PMTs are shown in Table 2.1. There are three different sizes of PMTs used in CANDLES:

- twelve 10-inch PMTs on the 1st row of the sides of the vessel;
- thirty-six 13-inch PMTs on the 2nd, 3rd and 4th rows of the sides of the LS vessel;
- fourteen 20-inch PMTs on top and bottom of the LS vessel.

The light pipes are placed between the LS vessel and the PMTs [57] to increase the photo-coverage. Scintillators, PMTs and light pipes are mounted inside a cylindrical water tank with a height of 4 m and a diameter of 3 m. In order to reduce the background induced by (n,γ) reactions inside and outside the tank, a passive shielding consists of lead (to reduce γ) and boron (to reduce neutron) [58]. Outside the passive shielding, we installed a geo-magnetic cancellation coil, which helps increase the efficiency of photoelectron collection [59]. The whole detector is currently operated at a constant temperature of 2 ^{0}C degrees in order to increase the light output of CaF_2(pure) [59].

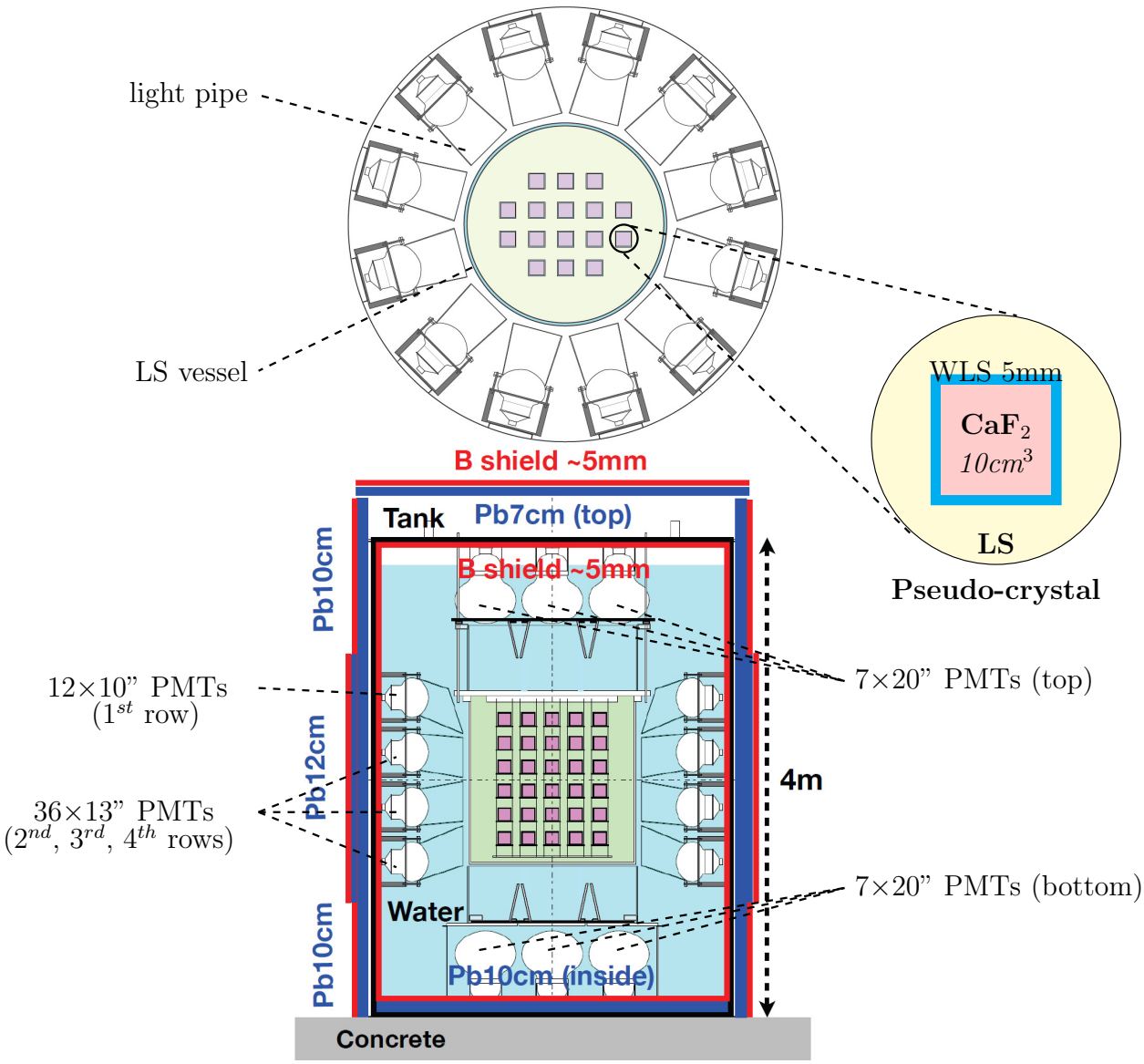

Figure 2.4: Experimental setup CANDLES III detector (top view - top figure, side view - bottom figure) with CaF_2 crystals submerged in a vessel filled with 2,000 L of liquid scintillator. There are 62 PMTs (12×10", 36×13", 14×20") surrounding the vessel. The vessel and PMTs are housed inside a cylindrical water tank ($4^h \times 3^\phi$ m). Between the PMTs and LS vessel, light pipes are installed to increase photo-coverage. A passive shield composed of Pb and Boron is installed to reduce the background from (n,γ) reactions [58].

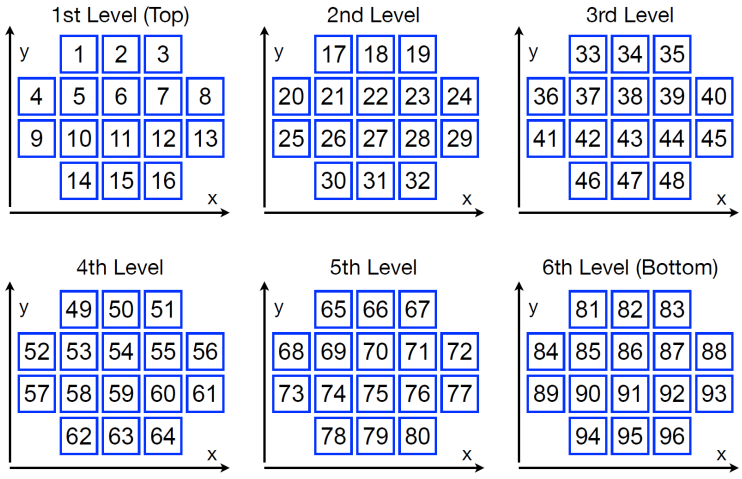

Figure 2.5: Layout of 96 CaF_2(pure) crystals in CANDLES III. These crystals are placed in a mounted-jig with 6 levels and 16 crystals per level.

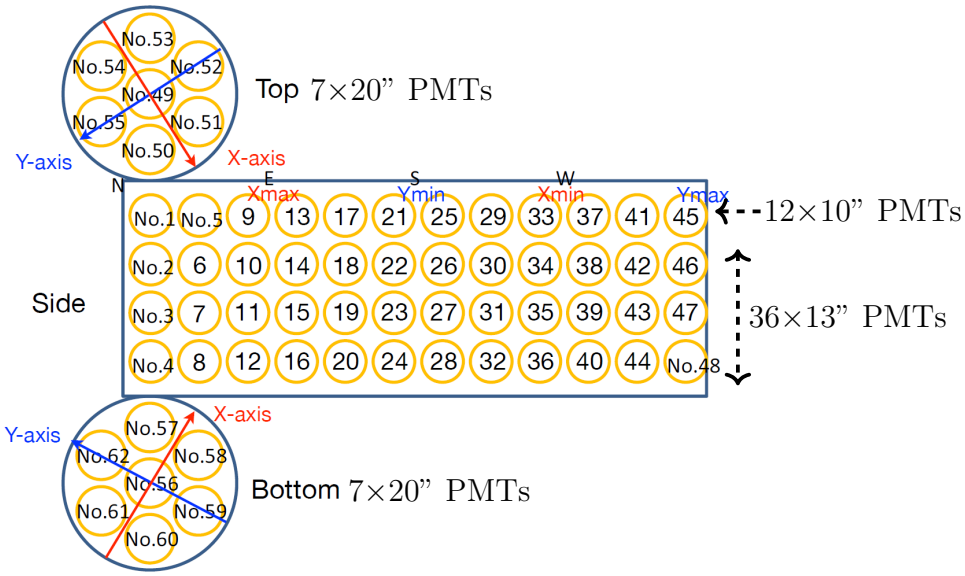

Figure 2.6: Layout of 62 PMTs in CANDLES III detector.

2.2.3 Scintillator

A. CaF_2(pure) and Wavelength Shifter

In ELEGANT VI, there were twenty-three CaF_2(Eu) crystals, each having the size of 45 mm. In CANDLES, to increase the sensitivity, it is decided to

Table 2.1: Characteristics of PMTs used in CANDLES

PMT Diameter	253 mm (10 inch)	332 mm (13 inch)	508 mm (20 inch)
Product Name	Hamamatsu R7081-100 [55]	Hamamatsu R8055 [56]	Hamamatsu R7250 [56]
Photo-cathode	Bialkali	Bialkali	Bialkali
Dynode	10 stage Box&Line	10 stage Box&Line	10 stage Box&Line
Spectral Response	300 to 650 nm	300 to 650 nm	300 to 650 nm
Peak Wavelength	420 nm	420 nm	420 nm
Gain	1.0×10^7 (at 2 000V)	1.0×10^7 (at 2 000V)	5.0×10^7 (at 2 000V)

Table 2.2: Compare CaF_2(Eu) scintillator used in ELEGANT VI and CaF_2(pure) scintillator used in CANDLES [60].

CaF_2(Eu)	**CaF_2(pure)**
• Commonly used as scintillator	• Commonly used as lens
• Self absorption	• Good transparency
• 24 photons/keV	• about 10 photons/keV
• $\lambda_{emission}$ = 420 nm	• $\lambda_{emission}$ = 285 nm
⇒ ***well-matched with PMTs***	⇒ ***need Wavelength Shifter***

scaled up in three-dimensional by introducing 96 cubic crystals of CaF_2(pure) crystals, each having the size of 10 cm. CaF_2(pure) is selected as the scintillator material due to its long attenuation length of 10 m, longer than the attenuation length of 10 cm of CaF_2(Eu).

However, CaF_2(pure) has a disadvantage of emission wavelength. The emission wavelength of CaF_2(pure) is 285 nm, while CaF_2(Eu) emits blue-light wavelength of 420 nm (Table 2.2). The scintillation photons reach the photocathodes of PMTs and produce photoelectrons needed for our experiment. The quantum efficiency (Q.E.) is highest at the blue-light wavelength. To compensate this problem, the Wavelength Shifter (WLS) is introduced. The WLS can convert the UV photon from CaF_2(pure) to the blue-light photon. The WLS (with 5 mm thickness) is used to coat outside the CaF_2(pure) crystal to form a pseudo-crystal (Figure 2.4). Measured results of the emission wavelength of CaF_2(pure) and Q.E. of PMTs are plotted, respectively, in Figure 2.7-a and Figure 2.7-b. Figure 2.7-c shows the transparency of various detector components such as acrylic resin of LS vessel, acrylic resin of pseudo-crystal, solvent, as well as CaF_2. The details of WLS and LS are

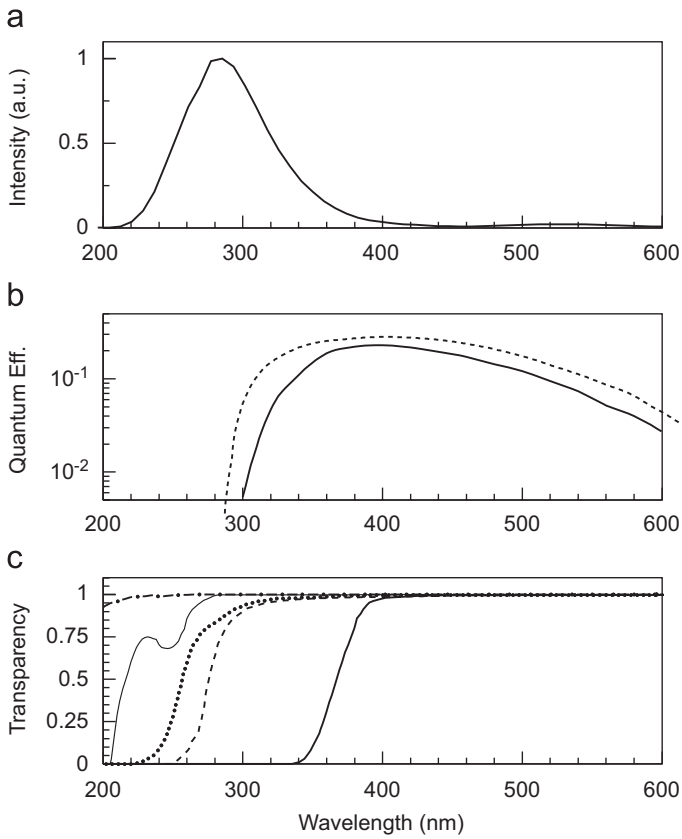

Figure 2.7: Optical properties of different components in CANDLES [61].
a. Spectrum of emission wavelength of CaF_2(pure);
b. Spectrum of Quantum Efficiencies of PMTs in CANDLES (dashed) and commercial PMTs (solid);
c. Transparency curves, from right to left, of UV-nontransparent acrylic resin used for the LS vessel (thick-solid), UV-transparent acrylic resin for pseudo-crystals (dashed), Paraol250 as a base solvent (dotted), quartz used for LS container in test experiments (thin-solid), and CaF_2 (dot-dashed).

also discussed elsewhere [60].

B. Liquid Scintillator

If $0\nu\beta\beta$ event occurs, the scintillation photons are produced inside the CaF_2 crystals. Therefore, the photons produced inside the LS are generated from unexpected radiations, which are γ-rays (inside and outside the tank) or cosmic rays. The decay constants of CaF_2 and LS are 1 μsec and 10

nsec, respectively (Figure 2.8). Therefore, we can discriminate the CaF_2 waveform, that is needed for Double Beta Decay study, from the LS waveform and CaF_2+LS waveform by using FADC and pulse shape discrimination. There are a lot of LS events in CANDLES III, and we developed our Data Acquisition (DAQ) system to reject LS events and select CaF_2 events using recorded waveform (section 2.2.4).

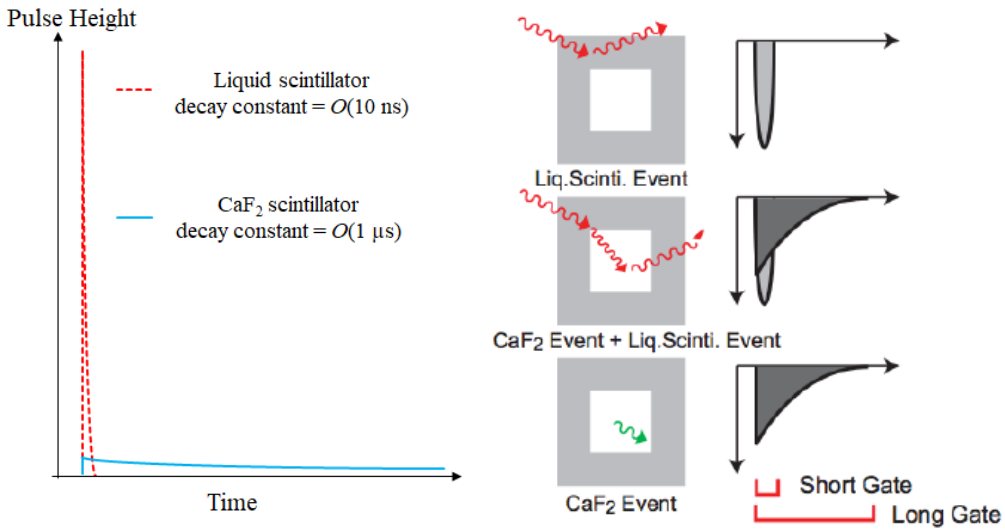

Figure 2.8: Typical pulse shapes obtained in the CANDLES III detector. Pulse Shapes of LS and CaF_2 [63] (left). Typical pulse shapes (from top to bottom) of the obtained waveform when incident radiation interacts with LS, LS+CaF_2 and CaF_2, respectively [62] (right). The Dual Gate trigger was introduced in the DAQ system [63] [65] to reject LS events.

2.2.4 Data Acquisition system

A. Micro Telecommunications Architecture Data Acquisition

Since 2016, a Micro Telecommunications Architecture Data Acquisition (μTCA DAQ) system with SpaceWire-to-GigabitEthernet network and eight event buffers was installed in CANDLES (*B. T. Khai et al.* [65]). The schematic view of our μTCA DAQ system is shown in Figure 2.9. The system includes 37 Advanced Mezzanine Cards FADCs (AMC-FADCs) with two input channels and eight event-buffers for each channel. We are using ADC0850DL, a product of Texas Instrument [66], with 8-bit resolution, 500 MHz sampling speed, and the Effective Number Of Bits (ENOB) is 7.5 bits

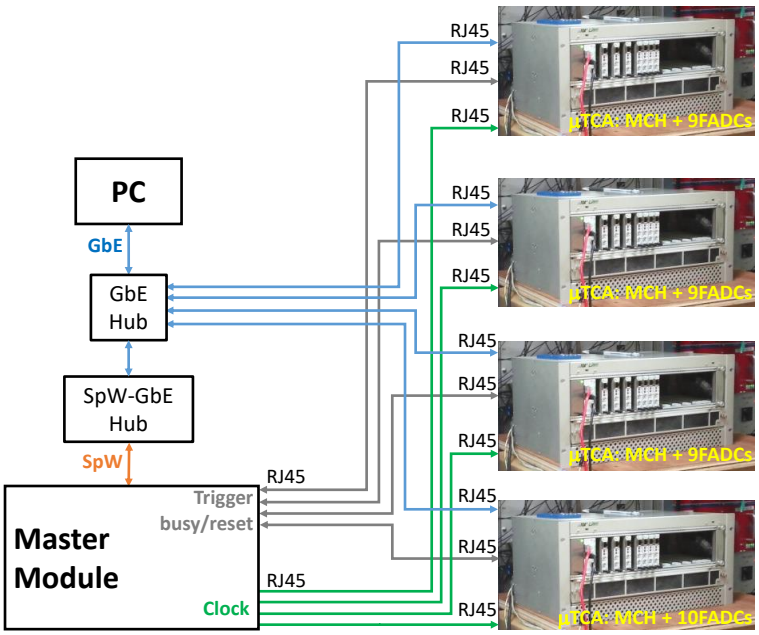

Figure 2.9: The μTCA DAQ system consists of Master Module, MCHs, and AMC-FADCs [65]. The PC can access to the DAQ system via Gigabit Ethernet.

at 125 MHz input and 500 MHz sampling speed. These AMC-FADCs are mounted in 4 μTCA crates; each crate contains 9 (or 10) AMC-FADCs and 1 μTCA carrier hub (MCH). The MCH is used for data readout, clock distribution, and trigger control of all AMC-FADCs in the same crate. A Master Module developed under Nuclear Instrument Module (NIM) standard is introduced for synchronizing clock and trigger signals of all AMC-FADCs via 4 MCHs.

B. Trigger in CANDLES

The high-level trigger decision made by the MCH is produced by the local trigger logic of each FADC [65]. In addition to 62 FADC channels for recording waveform of each PMT, there are 12 FADC channels used to record the sum signals for trigger purposes. The local trigger is made based on the analog sum of 62 PMTs. The trigger decision is made mainly to select CaF_2 events, which are the most interested in CANDLES, by performing a dual gate trigger with prompt-delay window coincidence [63]. In addition to the Dual Gate trigger, the trigger decisions are also produced for other monitoring triggers:

- Low Threshold Dual Gate trigger: is made to select the CaF_2 events at the lower threshold;
- Minimum Bias trigger: is made to select LS events;
- Cosmic trigger: is made to select cosmology by using coincidence of PMTs on the top and bottom;
- Clock trigger (constant 3 cps): is made for monitoring pedestal and single photoelectron charge from the dark current.

To not cause the deadtime for recording the CaF_2 events, the number of decisions for Low Threshold Dual Gate trigger and Minimum Bias trigger is prescaled by a factor of 1/80 and 1/2000, respectively, inside the trigger system. After the construction of passive shielding [58], the trigger rate of CANDLES is about 10 cps.

C. Event data size

As signals of all PMTs are fed to the AMC-FADCs, the time windows of the digitized waveform are set at 8.96 μsec. To reduce the data size, the AMC-FADC is developed with a summation function [67, 68]. The waveform is digitized every 2 nsec with 8-bit/sample in the first 768 nsec; after that, 64-nsec digitized values are integrated and recorded as 16-bit strings [63, 64, 65]. The data size of one waveform in each FADC is 640 Bytes, including 384 Bytes of 8-bit points and 128 Bytes of 16-bit points. Thus, the total data size, including waveform informationof one CANDLES event and other trigger information, is nearly 50 kBytes. Table 2.3 is the comparison of data format in CANDLES III (currently used) and Photon Counting (this thesis, discussed in Chapter 6).

Table 2.3: Compare the data format in CANDLES III (current) and Photon Counting (this thesis)

	CANDLES III	**Photon Counting**
2 nsec (8 bits) points	384 points	2044 points
64 nsec (16 bits) points	128 points	2 points
Time window	8960 nsec	4216 nsec
Size/FADC	640 Bytes	2048 Bytes
Size/Event	49,552 Bytes	153,774 Bytes
Size/24hour @10cps	~43 GBytes	~133 GBytes

Filename format and Detector development

Every day, the data taken from our detector is recorded as raw data with the filename format as follow:

Run[**RunNo.**]-[**SubRunNo.**]-[**SubSubRunNo.**].dat

where:

- **RunNo.** is the Run Number used to indicate the detector developments, which is explained in the next paragraph.
- **SubRunNo.** is the Sub Run Number (SRun). It is used to differentiate the data taken on different dates.
- **SubSubRunNo.** is the Sub Sub Run Number (SSRun) introduced to divide the data taken in one day into many data files. The size of one Sub Sub Run is 2 GBytes (about 4×10^4 events/SSRun).

As the plan to achieve the detector with high performance in energy resolution and background subtraction, there are several developments carried out in Kamioka Underground Observatory. These developments are indicated by the Run number in the raw data file name. The Run numbers corresponding to the detector developments are listed as below:

- Run001 - Run006: test runs
- Run007: installation of magnetic coil and rearrangement of the CaF_2(pure) crystals
- Run008: installation of cooling system
- Run009: installation of lead shield and boron shield inside and outside of the water tank, installation of 10-inch PMTs at 1st row on the tank side, introduction of the μTCA DAQ system.
- Run010: introducing one more μTCA crate with one MCH and six AMC-FADCs for the measurement of cosmic-ray induced background in CANDLES III detector [72].

2.3 Background

Although most of the background can be removed by passive and active shielding, there are still background events around the Q-value region. The remained background events in CANDLES are originated from the event from $2\nu\beta\beta$, the external background from (n,γ) reactions, the background from ^{49}Ca, the β-decay events from ^{208}Tl, and the sequential BiPo decays.

2.3.1 The $2\nu\beta\beta$ events

The $2\nu\beta\beta$ is an irreducible background in the CANDLES experiment and it is proportional to the mass of ^{48}Ca. It is discussed in Chapter 3.

2.3.2 The external background from (n, γ) reactions

The external background from (n, γ) reaction was the most dominant background in CANDLES III. In an underground laboratory, the environmental neutrons are mainly produced by the (α, n) reactions with elements inside the rock, with α are emitted from uranium and thorium decay chains [69]. In Kamioka site, the environmental neutron flux is in the order of 10^{-5} cm^{-2}s^{-1} (either thermal or fast neutron) [70], while the muon-induced neutron flux emerging from the rock is much smaller (in the order of 10^{-8} cm^{-2}s^{-1}) [71]. As the neutron from the environment captures on the material (such as stainless steel and rock) near our detector, γ-rays with high energy (up to 10 MeV) are produced and observed in the detector. The estimated background from (n,γ) reactions is 74$\pm$10 events/year/96crystals [58]. A passive shield containing Pb (to absorb γ-ray) and Boron (to absorb neutron) was installed inside and outside of the tank (Figure 2.1) to reduce this background. After installing the passive shield, the (n,γ) background is expected to be 1 events/year/96crystals [58].

2.3.3 Background from ^{49}Ca

When performing the measurement with enriched $^{48}CaF_2$ crystals, in addition to $2\nu\beta\beta$ background, we also have the background events originated from ^{49}Ca. The ^{49}Ca background events mainly come from the cosmic-ray [72]. As the cosmic-ray interacts with detector material and produces neutrons, these neutrons capture on ^{48}Ca and create ^{49}Ca isotopes. With high $Q_{\beta+\gamma}$ of 5262 keV, the β-decay from ^{49}Ca behave as background in $Q_{\beta\beta}$ of ^{48}Ca, especially, after enrichment process in CANDLES V, which is explained in section 2.5. According to previous research [72], when carrying out the measurement with CANDLES V detector, the background from ^{49}Ca is estimated as about 0.8 counts/year, which is higher than expected background (Table 2.4). A Monte Carlo simulation as conducted to study the method for the reduction of this background. As a result, using smaller crystals (cubic size 10 cm down to 5 cm) and active shielding can reduce the background from ^{49}Ca down to 0.04 counts/year [72]. Notably, either reducing crystal size or introducing active shielding is not sufficient to reduce $2\nu\beta\beta$ background within the region of interest.

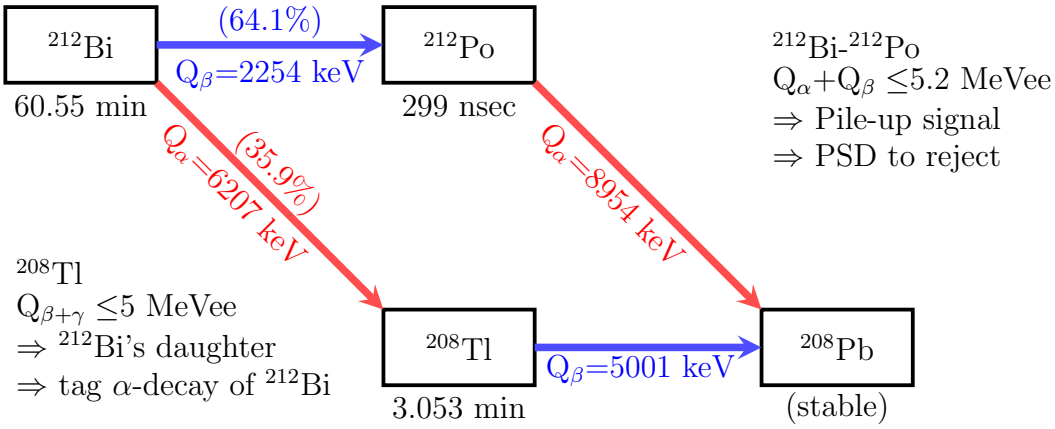

Figure 2.10: The decay chain of impurities as background in CANDLES III. There are two background components: β-decay from ^{208}Tl and ^{212}Bi-^{212}Po.

2.3.4 The β-decay events from ^{208}Tl

The β-decay from ^{208}Tl has $T_{1/2}$ ≈3 min and $Q_{\beta+\gamma}$ ≈5 MeV (Figure 2.10), which can contribute as background in $Q_{\beta\beta}$ region of ^{48}Ca. As this decay occurs after the α-decay of ^{212}Bi, to remove it, we can tag the preceding α-decay. For high tagging efficiency, the deadtime of our DAQ system must be minimized at the trigger rate [65]. The details of background rejection of β-decay from ^{208}Tl by offline analysis are explained elsewhere [73]. In reference [73], the contamination of ^{208}Tl (after background reduction) was estimated as:

$$^{208}\text{Tl: } 9.2\text{-}11.9 \pm 0.1 \text{ (stat.)} \pm 1.2 \text{ (syst.) events/129.5days.}$$

2.3.5 The BiPo sequential decay

The ^{212}Bi^{212}Po is the sequential decay of β-decay (Q_β=2254 keV) from ^{212}Bi and α-decay (Q_α=8954 keV) from ^{212}Po (Figure 2.10). Due to the short half-life of ^{212}Po (about 300 nsec), these two decays can be obtained in the same waveform as a pile-up event. The visible energy of α-decay from ^{212}Po is reduced by a factor 1/3 due to the quenching effect. Thus, the visible energy of this pile-up event is Q_β+Q_α ≤ 5.2 MeV, which acts as a background in $Q_{\beta\beta}$ region of ^{48}Ca. We can reject this background by using waveform analysis. The details of background rejection of BiPo sequential decays are explained elsewhere [73]. In reference [73], the contamination of ^{212}Bi-^{212}Po (after background reduction) was estimated as:

^{212}Bi-^{212}Po: 18.1 ± 0.1 (stat.) ± 0.7 (syst.) events/129.5days.

At this moment, the background events from ^{208}Tl and ^{212}Bi-^{212}Po are the dominant background in CANDLES detector. Since both of them are the daughter of ^{232}Th which is contaminated inside the CaF_2(pure) crystals, the better sensitivity can be achieved if we have more purify crystals. Currently, the average radioactivity contamination of ^{232}Th is 18.7 μBq/kg, and there are only 26 crystals (in 96 crystals) that have low radioactive contamination (less than 10 μBq/kg). The CaF_2(pure) with less contamination is being prepared for the upcoming measurements.

2.4 Enrichment

In order to compensate the demerit of rare natural abundance, a practical method to enrich ^{48}Ca is a must. So far, there has been no method to enrich ^{48}Ca with high efficiency and low cost because there is no gaseous compound of Calcium at room temperature to conduct the centrifugal separation. The only way for mass separation is using an ion beam, and it may cost about 10 MJPY/g. Therefore, CANDLES collaboration are now studying different enrichment methods: Resin method [76, 77], Micro Reactor [78], Multi-Channel Counter-Current Electrophoresis [79] and Laser method [81, 81]. We expect to introduce highly enriched $^{48}CaF_2$ crystals in the future generations of the CANDLES detector.

2.5 CANDLES: current and future prospect

As mentioned, CANDLES III is the current detector setup in Kamioka; CANDLES IV and CANDLES V are the future generations. Table 2.4 indicates the difference in detail setup and targets in neutrino mass sensitivity and expected background. To improve the sensitivity for $0\nu\beta\beta$ research, the strategy of CANDLES is increasing the mass of ^{48}Ca while reducing the background events near Q-value region. We currently running with 305 kg CaF_2(pure) crystals (no enrichment) at the temperature of 2 ^{0}C.

At the moment, we aim to achieve a sensitivity of neutrino mass of 0.5 eV with 300 kg of non-enriched CaF_2 crystals running at a temperature of 2 ^{0}C. In future detectors, we aim to achieve a much-improved sensitivity of neutrino mass, which is 80 meV and 9 meV in CANDLES IV and CANDLES V, respectively. To do that, we are carrying out developments in background rejection, isotope enrichment and energy resolution. For energy resolution,

Table 2.4: Series of CANDLES detector: current and future [82]

	CANDLES III	**CANDLES IV**	**CANDLES V**
CaF_2 crystal	305 kg	2 ton	2 ton
Abundance	0.187 %	2 %	50 %
Mass of ^{48}Ca	350 g	25 kg	610 kg
Resolution (σ/E)	2.6 %	1.2 %	0.4 %
Expected background ($2\nu\beta\beta$, ^{212}Bi, ^{208}Tl)	0.27/year	<0.7/3year	<0.2/9year
$<m_\nu>$	0.5 eV	80 meV	9 meV
	no enriched, 2^0C *(current)*	**2% enriched, cooling *(future)***	**50% enriched, bolometer *(future)***

scintillation bolometer detector, which is operated at about 10 mK, for CaF_2 crystals is under development process in different approaches:

- Scintillator Bolometer for CaF_2(pure): a prototype is setup in Korea in cooperation with AMORE collaboration [83],
- Scintillator Bolometer for CaF_2(Eu): a prototype is setup in Korea in cooperation with AMORE collaboration [84],
- Scintillator Bolometer for CaF_2(pure): a prototype is setup in Osaka University [85].

Chapter 3

Background of $2\nu\beta\beta$ and Energy resolution

Background events affect on the sensitivity when searching for the $0\nu\beta\beta$ events. Among the background events discussed in section 2.3, $2\nu\beta\beta$ acts as an irreducible background in CANDLES experiment. Additionally, the $2\nu\beta\beta$ background is a significant matter when we use enriched scintillation crystals in the future generations of CANDLES. In the energy spectrum, the $0\nu\beta\beta$ can be distinguished from $2\nu\beta\beta$ by improving energy resolution. In this chapter, the $2\nu\beta\beta$ background events and energy resolution, which are the two essential aspects of this thesis, are discussed. Moreover, the chance to improve the energy resolution of CANDLES III is indicated at the end of this chapter.

3.1 Overview of $2\nu\beta\beta$ background

The background events of CANDLES are mentioned in section 2.3. Passive shielding, pulse shape discrimination, adjustment of crystal size, and active veto can remove background from (n,γ) reactions, BiPo sequential decay, ^{208}Tl β-decay and ^{49}Ca β-decay, but not $2\nu\beta\beta$. In $0\nu\beta\beta$ experiment, we obtain double beta decay events including $0\nu\beta\beta$ and $2\nu\beta\beta$ events. The difference between $2\nu\beta\beta$ and $0\nu\beta\beta$ is the emission of $\overline{\nu_e}$. Since CANDLES detector cannot observe $\overline{\nu_e}$, it is impossible to discriminate $0\nu\beta\beta$ from $2\nu\beta\beta$ by particle identification or waveform analysis. The kinetic energy of 2 β^- is deposited as a continuous spectrum with the endpoint of Q-value. On the other hand, as $0\nu\beta\beta$ emits no $\overline{\nu_e}$, the kinetic energy of 2 β^- deposited as a discrete energy peak. Therefore, improvement of energy resolution is the only way to distinguish $0\nu\beta\beta$ and $2\nu\beta\beta$ events.

Table 3.1: Comparison of $2\nu\beta\beta$ background rate with different mass of ^{48}Ca and energy resolution using simulation

^{48}**Ca Mass**	$\sigma/\mathbf{E} = \mathbf{2.6}$ %	$\sigma/\mathbf{E} = \mathbf{1.2}$ %	$\sigma/\mathbf{E} = \mathbf{1.0}$ %
M=0.3 kg (CANDLES III)	0.12×10^{-1} (counts/year)	0.1×10^{-1} (counts/year)	0.3×10^{-2} (counts/year)
M= 25 kg (CANDLES IV)	1.0×10^{1} (counts/year)	0.1×10^{1} (counts/year)	2.6×10^{-1} (counts/year)
M=610 kg (CANDLES V)	2.5×10^{2} (counts/year)	2.7×10^{1} (counts/year)	0.6×10^{1} (counts/year)

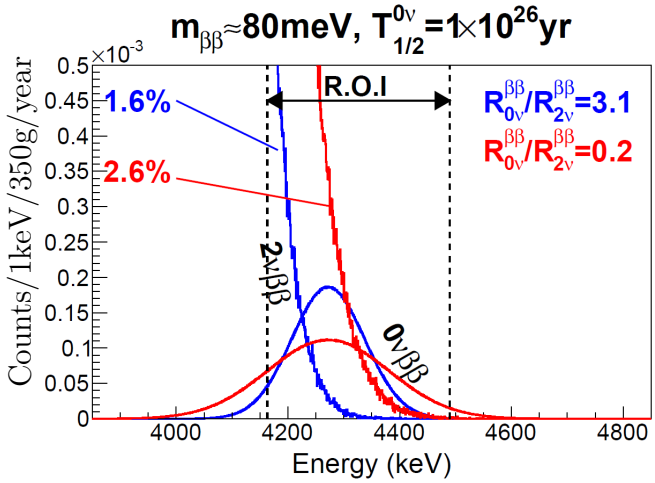

Figure 3.1: Simulation histograms of $0\nu\beta\beta$ and $2\nu\beta\beta$ with different energy resolutions. The energy resolutions used in this simulation are 2.6 % (red), which is the energy resolution at Q-value in Run009, and 1.6 % (blue), which is the statistical fluctuation of CANDLES III. The region of interest (ROI) is marked with dashed black lines.

The number of $2\nu\beta\beta$ events can be estimated as following the Taylor expansion equation:

$$N_{events} \approx N_A \frac{M(^{48}Ca)}{48} \times \ln 2 \frac{t}{T^{2\nu}_{\beta\beta}} \tag{3.1}$$

where N_{events} is number of $2\nu\beta\beta$ events,

N_A is the Avogadro number,

$M(^{48}Ca)$ is mass of ^{48}Ca (g),

t is measurement time (year),

$T^{2\nu}_{\beta\beta}$ is half-life of $2\nu\beta\beta$ of ^{48}Ca (= 4.2×10^{19} year [86, 87]).

According to the above equation, the background events from $2\nu\beta\beta$ is proportional to the mass of ^{48}Ca. The estimated $2\nu\beta\beta$ rates with different ^{48}Ca masses and energy resolutions are reported in Table 3.1. With more amount of ^{48}Ca used in the future CANDLES generations by introducing enriched crystals, the $2\nu\beta\beta$ will become a severe background. According to the table, as the energy resolution improved, the rate of $2\nu\beta\beta$ is reduced. Figure 3.1 shows the simulation spectra with the energy resolutions of 2.6 % (energy resolution in Run009) and 1.6 % (current statistical fluctuation) for the measurement of 350 g of ^{48}Ca in 1 year. The simulation was done with assumptions of the $0\nu\beta\beta$ half-life of ^{48}Ca is 10^{26} years and no natural background. Within the region of interest around Q-value, as the energy resolution improved from 2.6 % to 1.6 %, the ratio of $0\nu\beta\beta$ and $2\nu\beta\beta$ can be increased about 15 times. Due to the capability of increasing the $0\nu\beta\beta$ over $2\nu\beta\beta$ ratio, a study of the energy resolution of CANDLES detector is carried out in this thesis.

3.2 Energy resolution in CANDLES III

3.2.1 Energy resolution of a scintillator detector

The detection process of a radiation in one scintillator detector can be explained as sequential processes [88, 89, 90]:

⟨1⟩ The $\beta\beta$-ray observed in the crystal and, then, scintillation photons are emitted. The emission of photons can be affected by the inhomogeneity of the crystal and temperature dependence of light output. According to our measurement, the light output of CaF_2(pure) increases 1.35 times when reducing the temperature from 20 ^{0}C to 0 ^{0}C [73]. It is also the reason why we keep the temperature stable for CANDLES III (section 2.2). Additionally, the temperature is recorded as "slow" data during Physics Run for monitoring purposes.

⟨2⟩ The scintillation lights are collected in photocathode. Losing scintillation photons results in reducing the number of photoelectrons. Therefore, light pipes were installed between scintillator and PMTs to increase the collection efficiency (section 2.2).

⟨3⟩ The photoelectrons are produced at photocathode. Photoelectron emission depends on the wavelength of the incident photons. Since quantum efficiency is highest at the blue-light wavelength, the WLS is introduced to convert UV-light emitted from CaF_2(pure) to blue-light (section 2.2).

⟨4⟩ The photoelectrons are collected at the first dynode: The collection efficiency at the first dynode affects signal integration. The geomagnetic field can affect the collection efficiency at the first dynode so that the magnetic cancellation coil was introduced (section 2.2).

⟨5⟩ The electrons are multiplied by PMT dynodes. The multiplication (or gain factor) depends on the supplying high voltage. Therefore, high voltages of all PMTs are monitored every day during Physics Run. Additionally, the dark current emitted from cathode and dynodes can be multiplied and recorded during data taking; thus, it also affects the energy resolution.

⟨6⟩ With the multiplication of dynodes, a bunch of electrons forming into a signal is collected at PMT anode. The signal is recorded by the DAQ system; thus, it can be affected by electronic noises. In Chapter 4, some noises are found to be severe effects in the CANDLES III detector.

The electrons collected at the PMT anode are shaped into a signal which contains the energy information. Therefore, the fluctuation of the electrons at the anode affects energy resolution, and it can be derived as:

$$\left(\frac{\sigma_{\mathrm{A}}}{\mathrm{N_A}}\right)^2 = \left(\frac{\sigma_{\mathrm{p.e.}}}{\mathrm{N_{p.e.}}}\right)^2 + \left(\frac{\sigma_{\mathrm{scin}}}{\mathrm{N_{scin}}}\right)^2 + \left(\frac{\sigma_{\mathrm{pmt}}}{\mathrm{N_A}}\right)^2 + \left(\frac{\sigma_{\mathrm{DC}}}{\mathrm{N_A}}\right)^2$$

where σ_{A} is the fluctuation of $\mathrm{N_A}$ electrons collected at PMT anode.

$\sigma_{\mathrm{p.e.}}$ is the fluctuation of $\mathrm{N_{p.e.}}$ photoelectrons generated at PMT cathode by the incident scintillator photons. It is statistical fluctuation and it is defined as $1/\sqrt{\mathrm{N_{p.e.}}}$.

σ_{scin} is the non-statistical fluctuation of scintillator photons. It is also called the intrinsic resolution of scintillator.

σ_{pmt} is the fluctuation caused by PMT dynodes of $\mathrm{N_A}$ electrons collected at PMT anode. This fluctuation is related to the number of dynodes and multiplication of each dynode.

σ_{DC} is the fluctuation caused by the occurrence of dark current in cathode and dynodes when collecting $\mathrm{N_A}$ electrons.

As the signal is recorded by electronics system, the energy resolution at an energy peak (E) measured by a spectrometer including scintillator coupled to a PMT can be written as:

$$\left(\frac{\sigma_{\mathrm{E}}}{\mathrm{E}}\right)^2 = \left(\frac{\sigma_{\mathrm{p.e.}}}{\mathrm{N_{p.e.}}}\right)^2 + \left(\frac{\sigma_{\mathrm{scin}}}{\mathrm{N_{scin}}}\right)^2 + \left(\frac{\sigma_{\mathrm{pmt}}}{\mathrm{N_A}}\right)^2 + \left(\frac{\sigma_{\mathrm{DC}}}{\mathrm{N_A}}\right)^2 + \left(\frac{\sigma_{\mathrm{noise}}}{\mathrm{E}}\right)^2 (+\cdots) \tag{3.2}$$

where σ_{E} is the energy resolution at the energy peak E;

σ_{noise} is fluctuation coming from the noise.

Equation 3.2 is derived assuming all factors are independent. In the ideal case, the energy resolution is equal to the statistical fluctuation. The non-statistical fluctuations are affected by the scintillation process and the PMT gain. Therefore, the temperature and the supplied high voltage are monitored during data taking for checking the detector stability. In addition to these factors, there may be other factors contributing to the energy resolution.

3.2.2 The current energy resolution of CANDLES III

In previous research [73] using data of Run009, the energy resolutions at different energy peaks were obtained. These energy peaks included:

- ^{40}K (γ-ray): 1461 keV, which is obtained as natural background
- ^{208}Tl (γ-ray): 2615 keV, which is obtained as natural background
- ^{88}Y (γ-ray): 1836 keV, which is obtained in ^{88}Y calibration
- (n,γ) reaction on ^{1}H: 2223 keV, which is obtained in neutron calibration
- (n,γ) reaction on ^{28}Si: 3539 keV and 4934 keV, which is obtained in neutron calibration
- (n,γ) reaction on ^{56}Fe: 7631 keV, which is obtained in neutron calibration
- (n,γ) reaction on ^{58}Ni: 8534 keV and 8994 keV, which is obtained in neutron calibration
- α-rays of ^{220}Rn and ^{215}Po ($\times$ Quenching-Factor$\approx$0.3), which are obtained as natural background

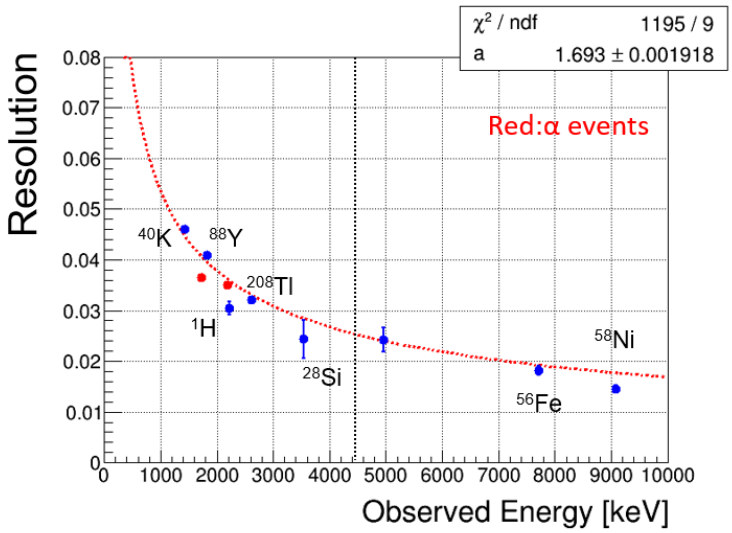

Figure 3.2: The energy resolution of CANDLES III [73]. These data points are obtained from fitting energy spectra of α (red points) and β events (blue circles). The dashed red line is the fitting function: $\sigma/\mathrm{E} = \mathrm{a}/\sqrt{\mathrm{E}}$. The energy resolution at Q-value of ^{48}Ca is 2.6 %.

All energy resolutions were plotted and fitted with below function:

$$\mathrm{Resolution(E)} = \frac{\sigma}{\mathrm{E}} = \frac{\mathrm{a}}{\sqrt{\mathrm{E}}} \tag{3.3}$$

where the value of a was obtained as 1.693 by fitting. Figure 3.2 shows the obtained energy resolutions and the fitting function. As a result, the energy resolution at Q-value was about 2.590±0.003 % [73]. The energy resolution in Run010 obtained was 2.4±0.2 % [74]. The difference in resolutions and the uncertainties may come from various sources, such as the adjustment of the pedestal (mentioned in Chapter 4) or the different analyses.

3.2.3 Statistical fluctuation

The statistical fluctuation is calculated as $1/\sqrt{\mathrm{N_{p.e.}}}$. Assuming the energy is linearly proportional to the number of p.e., the energy scale factor is estimated as:

$$\text{Energy Scale Factor (p.e./keV)} = \mathrm{N_{p.e.}}/\text{Energy}$$

where $\mathrm{N_{p.e.}}$ is the total p.e. obtained in one event. This number is calculated as the total charge obtained in the signal divided by the charge of a single

photoelectron. The scale factor obtained is 0.91 p.e./keV from Physics Run data in Run010. This scale factor is discussed in more details in section 4.2.1. Thus, the number of p.e. at Q-value is

$$N_{p.e.}(^{48}Ca) = 4272 \text{ keV} \times 0.91 \text{ p.e./keV} \approx 3888 \text{ p.e.},$$

hence, statistical fluctuation at Q-value is about $1/\sqrt{3888} \approx 1.6$ %.

3.2.4 Crystal dependence

In CANDLES, the light outputs of each CaF_2 crystals are different. The energy calibration is carried for each crystal using the γ-peak (1836 keV) of ^{88}Y. The β+LS accidental events can be contaminated around the 1836 keV γ-peak. Therefore, the peak positions in calibration and Physics Run are different, and the difference depends on the crystal [73]. Figure 3.3 shows the crystal dependence of the peak positions at the γ-peak of ^{208}Tl (2614 keV). At 2614 keV, the standard deviation of peak positions of 96 crystals is about 60 keV (equivalent to 2.3 %) due to the accuracy of the calibration [73]. In the current analysis, the crystal dependence is corrected for each layer. After correction, the standard deviation is reduced to 8 keV (equivalent to 0.3 %), negligible, at 2614 keV [73].

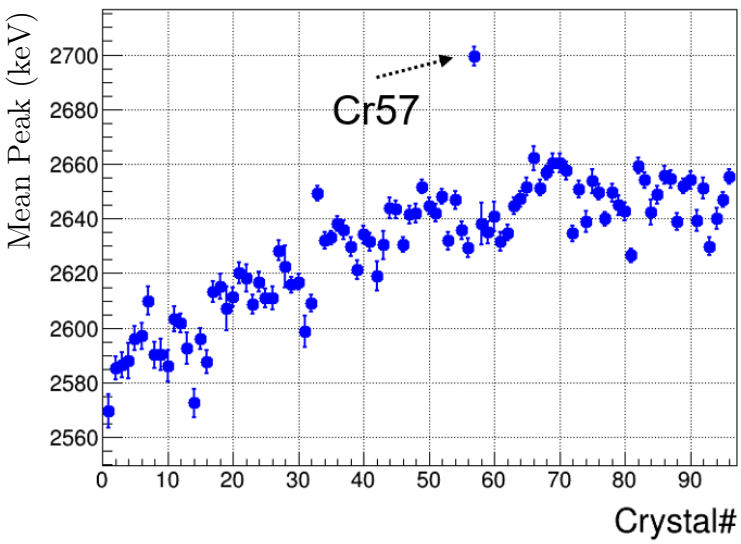

Figure 3.3: The crystal dependence of mean value of ^{208}Tl γ-peak [73].

3.2.5 Improve the energy resolution

After many efforts, which are recalled in processes ⟨1⟩ to ⟨5⟩ in section 3.2.1, to improve the detector performance, the energy resolution (σ_E/E) of CANDLES III is obtained as 2.6 % at Q-value in Run009 and 2.4 % in Run010. However, the statistical fluctuation (σ_{stat}/E) is only 1.6 %. It means there should be other fluctuation(s) affecting the energy resolution. As mentioned in section 2.2.4, the waveform in every PMT is recorded with a window gate of 8.96 μsec, and the sum waveform is then produced by combining the digital waveform of 62 PMTs (Figure 3.4). In the current analysis, because the CaF_2 scintillator has a long decay constant of 1 μsec, we make a signal integration of 4 μsec of the sum waveform to calculate the deposited energy:

$$\text{Energy} \propto \text{Signal Integration} = \sum_{i=0}^{2000} (\text{Pedestal} - \text{Signal[i]}) \tag{3.4}$$

where Pedestal is corresponding to the baseline of the waveform,

Signal[i] indicates the value of the waveform at i^{th} timebin (2 nsec/timebin).

Due to the long period integral, the fluctuation from the baseline affects the energy, and it causes other fluctuations factor contributing to the energy

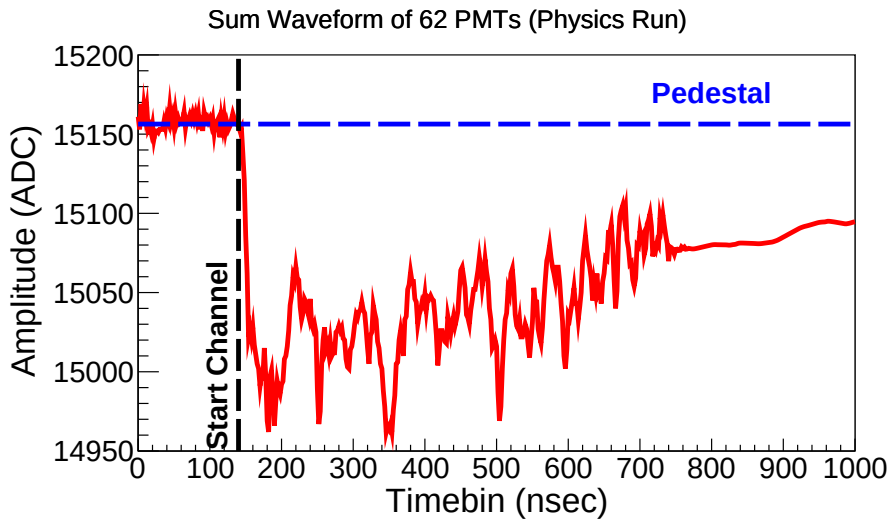

Figure 3.4: The sum waveform in CANDLES with a CaF_2 event. The vertical axis is in unit of ADC, and the horizontal axis is in unit of timebin (2nsec/timebin). Values at first bins of waveform are used to calculate the pedestal. The integral of the waveform is proportional to the energy.

resolution. These baseline fluctuation is proved and estimated in Chapter 4. The research motivations of this thesis are studying the baseline fluctuation effect in the energy resolution of the CANDLES detector and developing a new analysis method to reduce these fluctuations. The goal is removing the baseline fluctuation as much as possible to improve the energy resolution on the CANDLES III detector for searching of $0\nu\beta\beta$ from ^{48}Ca.

Chapter 4

Baseline fluctuation in CANDLES III

As discussed in the previous chapter, the energy resolution depends on the following factors:

- Statistical fluctuation: It depends on the number of photoelectrons and the multiplication of PMT dynodes. The fluctuation of the number of photoelectrons is the main contribution to the energy resolution of the scintillation detector. It is essential to increase the number of photoelectrons by improvements of photon collection efficiency and to increase the light yield by low-temperature measurement.

- Detector stability: The scintillation process is affected by the temperature. The PMT gain is affected by the supplied high voltage. Their change makes the energy resolution worse. In CANDLES, the temperature and high voltage are monitored as "slow data" for necessary adjustment.

- Error of charge measurement: It is caused by the noise and the error of the baseline measurements.

Since the signal is integrated for a long interval of 4000 nsec, the dark current and the errors of charge measurement can be accumulated. The errors of charge measurement in a long interval include the noises in baseline, the digitization error and the error in pedestal measurement. In this chapter, the dark current and the errors of charge measurement are discussed.

4.1 Dark Current

The photoelectrons are obtained from the scintillator. Besides, we may detect the electrons of the Dark Current during the waveform recording. The Dark Current influences the energy resolution. In this section, the effect of Dark Current on the energy resolution of CANDLES is estimated. An analysis is carried out to estimate the rate of Dark Current signal in every PMT. Clock events (random trigger) are used in this analysis to avoid the photoelectrons from the scintillator. However, small scintillation photons may be accidentally collected in this analysis. To estimate the rate of dark current (and small scintillation photons), a threshold is set individually for each PMT to count the number of photoelectrons. The details of thresholds are discussed in section 6.1.1. The counting rate is shown as the count in

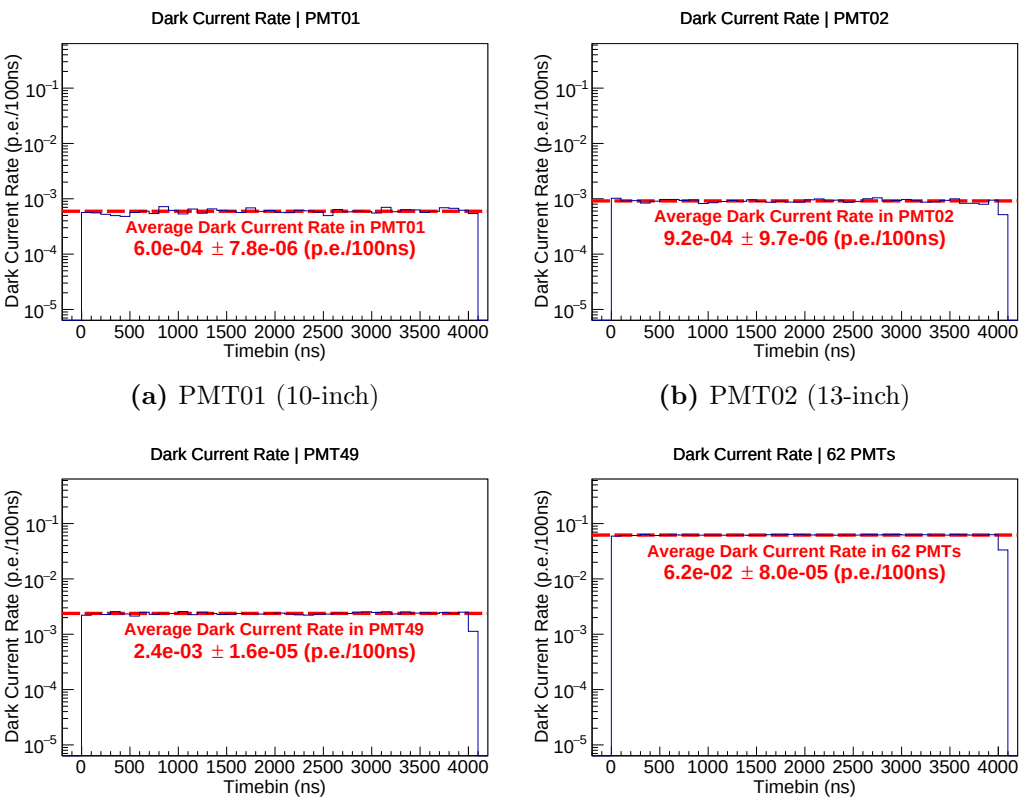

(a) PMT01 (10-inch) **(b)** PMT02 (13-inch)

(c) PMT49 (20-inch) **(d)** All PMTs

Figure 4.1: Check of Dark Current Rate at every 100 nsec in the waveform of PMT01 (a), PMT02 (b), PMT49 (c), and sum waveform (d). The red-dashed lines indicate the mean dark current rate obtained in each PMT.

every 100 nsec. The dark current in the sum waveform is a sum of the dark current rate of 62 PMTs. Figure 4.1 shows the uniform distributions of dark current rates in the waveform of PMT01 (10-inch), PMT02 (13-inch), PMT49 (20-inch), and the sum waveform of 62 PMTs. The red-dashed lines indicate the mean dark current rates. In the sum waveform, the mean rate of dark current is 6.2×10^5 p.e./sec. Figure 4.2 shows the mean rates of dark current of all PMTs. All dark current rates are in the order of 10^4 p.e./sec. The dark

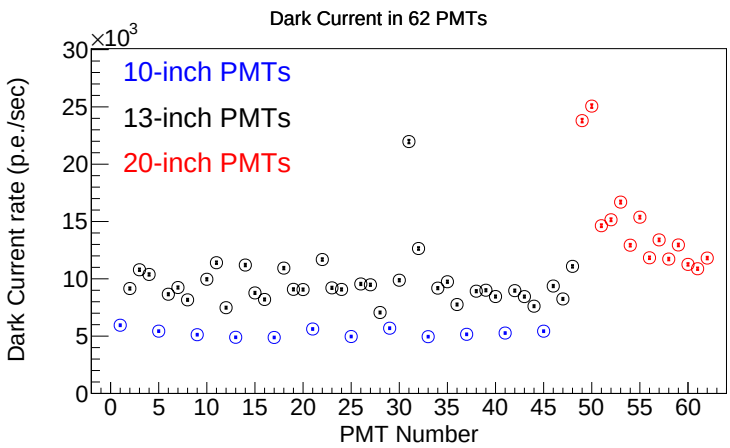

Figure 4.2: Dark Current Rate of 10-inch PMTs (blue), 13-inch PMTs (black) and 20-inch PMTs (red).

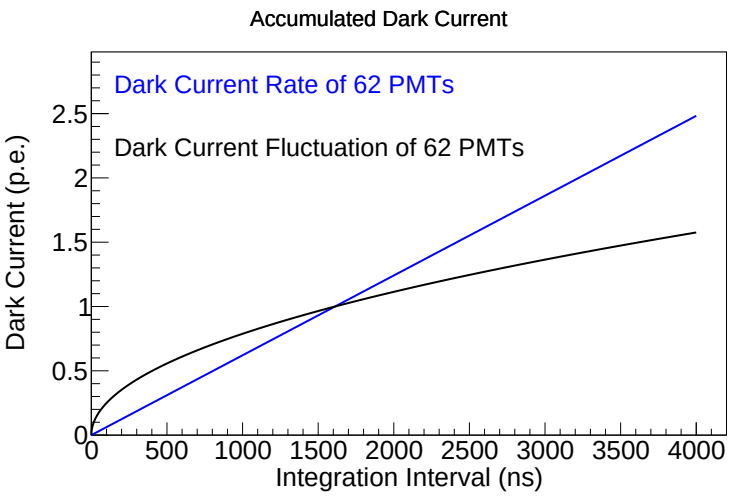

Figure 4.3: Dark Current Rate accumulated in the sum waveform of 62 PMTs (blue line) linearly corresponds to the integration interval. The statistical fluctuation of Dark Current is plotted with black line.

current rates of 10-inch PMTs are lowest.

The mean of dark current of 62 PMTs (μ_{DC}) is accumulated in a integration interval T. It is estimated as:

$$\mu_{\mathrm{DC}} = \text{Dark Current Count} = \frac{\text{Mean Rate}^{\mathrm{SUM}}}{100\mathrm{ns}} \times \mathrm{T}.$$

The mean value and the fluctuation of dark current are plotted in Figure 4.3. At the integration interval of 4000 nsec, the average number of dark current in one event is about 2.5 p.e., and the fluctuation of dark current (σ_{DC}) in one event is about 1.6 p.e. The contribution of dark current to the energy resolution is negligible:

- at the γ-peak of ^{40}K ($\sim$1329 p.e.), the $\sigma_{\mathrm{DC}}/\mathrm{E}$ is about 0.1 %;
- at the γ-peak of ^{208}Tl ($\sim$2379 p.e.), the $\sigma_{\mathrm{DC}}/\mathrm{E}$ is about 0.06 %;
- at the Q-value of ^{48}Ca ($\sim$3838 p.e.), the $\sigma_{\mathrm{DC}}/\mathrm{E}$ is about 0.04 %.

4.2 Digitization Error

4.2.1 Introduction of digitization error

In CANDLES, we are using the 500MHz-8bits ADC08DL502 from Texas Instrument [66] to record the waveform with 7.5 Effective Number Of Bits (ENOB). The pedestal is calculated as the average value of several first data points in the waveform. The digitization error is the difference of the measured pedestal and the true pedestal due to the Least Significant Bit (LSB) of the ADC. Assuming the distribution of true pedestal is Gaussian with the mean (μ_{A}) and the standard deviation (σ_{A}) (Figure 4.4), the probability to record a digitized values "n" can be expressed as:

$$\mathrm{P_n} = \int_{\mathrm{n}-0.5}^{\mathrm{n}+0.5} \frac{1}{\sqrt{2\pi}\sigma_{\mathrm{A}}} \exp\left(\frac{(\mathrm{x}-\mu_{\mathrm{A}})^2}{2\sigma_{\mathrm{A}}}\right) \mathrm{dx} \tag{4.1}$$

The measured pedestal is calculated as:

$$\text{Measured Pedestal} = \langle \mathrm{n} \rangle = \sum (\mathrm{n} \times \mathrm{P_n}) \tag{4.2}$$

Using these two equations 4.1 and 4.2, one can plot the measured pedestal as a function of true pedestal (Figure 4.5-a), and the digitization error as a

function of measured pedestal (Figure 4.5-b). The digitization error is calculated as the true pedestal subtracting the measured pedestal. The calculations in these figures were made with three σ_A values of 0.1 ADC, 0.2 ADC and 0.3 ADC. The digitization error is zero at the data points at 244

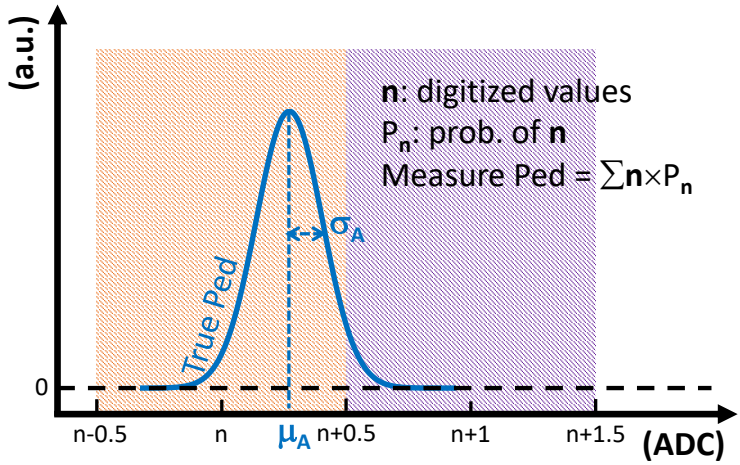

Figure 4.4: The Gaussian distribution of true pedestal. Measure pedestal is obtained by calculating the average of digitized values.

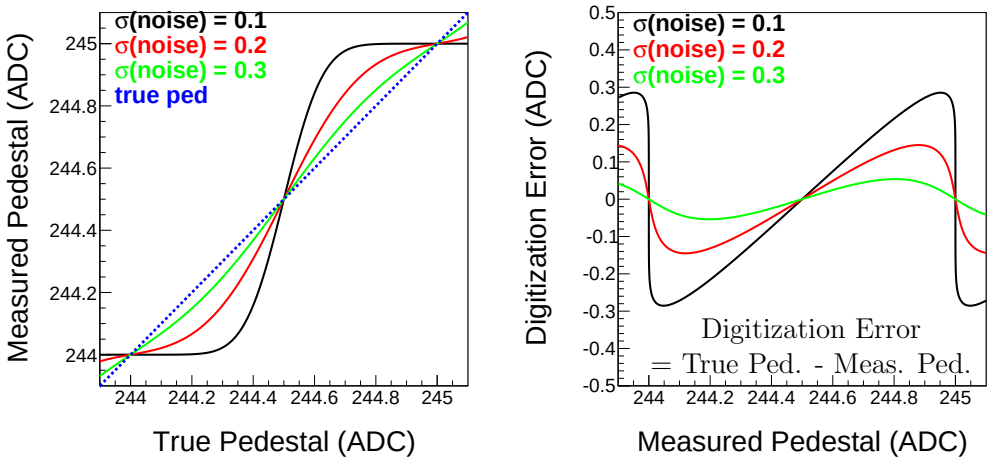

(a) Measured Pedestal vs True Pedestal (calculation) **(b)** Digitization Error vs Measured Pedestal (calculation)

Figure 4.5: The theoretical plots of Measured Pedestal as a function of True Pedestal (a); and the theoretical plots of Digitization Error as a function of Measured Pedestal (b) with 3 different σ_A values of 0.1 ADC, 0.2 ADC and 0.3 ADC.

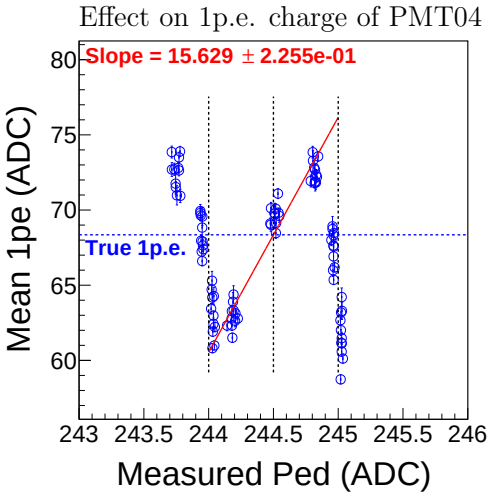

Figure 4.6: The 1p.e. charge value is plotted as a function of the measured pedestal. The vertical dash lines indicate the measured pedestal values of 244 ADC, 244.5 ADC and 245 ADC. The solid-red line is the linear fitting function. Value of True 1p.e. (horizontal dash line) is estimated at the measured pedestal of 244.5 ADC using the linear function.

ADC, 244.5 ADC, and 245 ADC. From the figures, we can see the digitization error approaches to zero if the σ_{A} is large. The ENOB of an ADC can be determined by the σ_{A} [91]. For an 8-bit ADC, σ_{A} is proportional to $2^{8-\mathrm{ENOB}}$. The ENOB is reduced if σ_{A} is increased; thus, the digitization error becomes smaller. In CANDLES, the ADCs with 8-bit resolution are selected for further analysis related to energy spectrum and pulse shape discrimination.

To calculating the charge of single photoelectron (1p.e.), the measured pedestal is subtracted from 1 p.e. waveform ($\sum_{\mathrm{i}}(\mathrm{Ped} - \mathrm{Signal[i]})$). For the waveform integration, the digitization errors are randomly summed, the average digitization error is about zero [92]. On the other hand, the digitization error is accumulated in the measured pedestal. The digitization error is accumulated in the width of 1p.e. signal. The digitization error effect on the 1p.e. charge of every PMT was reported in previous research [93]. The correlation of 1p.e. charge and measured pedestal is assumed to be linear with measured pedestal ranging from 244.1 to 244.9 ADC [93]. Figure 4.6 shows the 1p.e. charge of PMT04 as a function of measured pedestal. The σ_{A} in PMT04 was estimated to be 0.23 ADC. The red-solid line is the linear correlation, and the vertical black-dashed lines mark the measured pedestals of 244 ADC, 244.5 ADC, and 245 ADC. The true value of 1p.e. charge calculated at the measured pedestal of 244.5 ADC is indicated with the horizontal

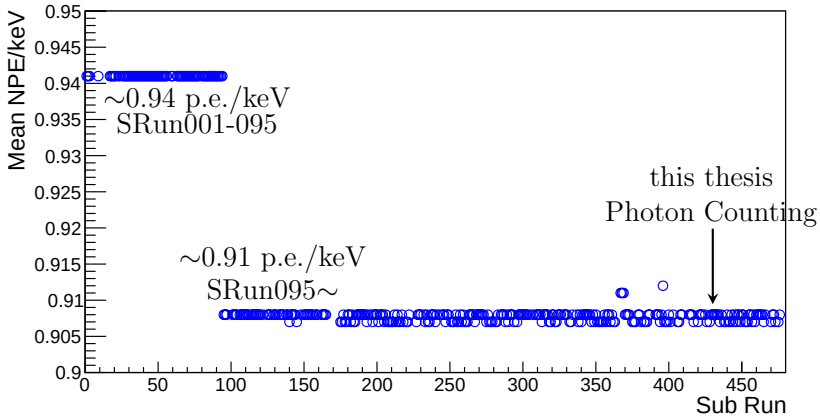

Figure 4.7: The energy scale factor is plotted as a function of time. The horizontal axis indicates SubRun in Physics Run. The scale factor is changed from SRun095 from ∼0.94 to ∼0.91 p.e./keV due to the pedestal adjustment.

blue-dashed line. When the measured pedestal fluctuates, the maximum fluctuation of digitization error is about ±0.5 ADC (Figure 4.5-b). Since the digitization error is accumulated when calculating the charge of 1p.e. signal, the fluctuation of of 1p.e. charge value, in Figure 4.6, is much more than the fluctuation of digitization error. From SRun095 in Physics Run, the pedestals of all PMTs are adjusted to 244.5 ADC to reduce the digitization error. Due to the digitization error effect, the 1p.e. charge is shifted after the pedestal adjustment, and it results in the change of energy scale factor from 0.94 to 0.91 p.e./keV (Figure 4.7). The research in this thesis was carried out after SRun430; hence, the energy scale factor of 0.91 p.e./keV is used to estimate the statistical fluctuation in this thesis.

4.2.2 Estimate the effect of digitization error

A. Estimate Digitization Error in energy spectrum

The effect of digitization error on the energy resolution of CANDLES III is discussed in this section. A CaF_2 signal contains many photoelectrons, and the digitization error of a 1p.e. signal is accumulated at the signal points. If the 1p.e. signals overlap each other, the number of signal points is reduced, and the digitization error is adjusted with a reduction factor. The calculations of overlap probability of 1p.e. signals and the reduction factor are mentioned in appendix C and appendix D. The digitization error effect

in CaF_2 signal is calculated as:

$$\Omega = \sum_{1}^{62} \mathrm{n}_{\mathrm{p.e.}}^{\mathrm{iPMT}} \times \gamma^{\mathrm{iPMT}} \times \frac{\mathrm{Slope}^{\mathrm{iPMT}} \times \left(\mathrm{Ped}^{\mathrm{iPMT}} - 244.5\right)}{\mu_{\mathrm{p.e.}}^{\mathrm{iPMT}}} \tag{4.3}$$

where Ω: the digitization error effect in a CaF_2 signal (p.e.);

$\mathrm{n}_{\mathrm{p.e.}}^{\mathrm{iPMT}}$: the number of photoelectrons in the ith PMT;

γ^{iPMT}: the reduction factor of the ith PMT. The estimation of reduction factor is described in appendix C;

$\mathrm{Slope}^{\mathrm{iPMT}}$: the slope of linear correlation between digitization error of 1p.e. charge and measured pedestal in the ith PMT. It was determined in previous research [93];

$\mathrm{Ped}^{\mathrm{iPMT}}$: the measured pedestal of the ith PMT,

$\mu_{\mathrm{p.e.}}^{\mathrm{iPMT}}$: the mean value of 1p.e. charge of the ith PMT. It is obtained by measuring the charge of dark current in Physics Run.

To estimate the digitization error in the energy spectrum, one can calculate the number of photoelectrons and measured pedestal from experimental data.

Figure 4.8 shows the dependence of digitization error on the number of photoelectrons. The histogram is produced using the data taken with the same trigger condition as in the Physics Run. With this trigger condition, the natural background spectrum is observed with γ-peaks emitted from ^{40}K (1460 keV) and ^{208}Tl (2614 keV). In the Figure 4.8, the digitization error increases with more number of photoelectrons. The circles and the error bars indicate the mean and the uncertainty of estimated digitization error at ^{40}K and ^{208}Tl peaks.

The digitization errors on ^{40}K and ^{208}Tl peaks are estimated. The energy cut ($\mu \pm 1\sigma$) for each peak is determined with the peak position (μ) and energy resolution (σ) obtained by the fitting. The distributions of the estimated digitization error effect on these two peaks are shown in Figure 4.9. At a determined number of photoelectrons, fluctuating pedestal causes the fluctuation of digitization error. The mean value (μ_{DE}) and the root mean square (σ_{DE}) of the obtained distribution affect on the peak position and energy resolution, respectively. The mean and width of digitization error distribution are increasing at higher energy with more photoelectrons; therefore, the shift of peak position and fluctuation at higher energy is more severe. The digitization error is strongly related to the shift of peak positions

in the Physics Run of CANDLES (appendix D). For the effect of digitization error on the energy resolution, it is studied in the next section.

B. The dependence on Integration Interval

The digitization error depends on the number of photoelectrons. The CaF_2 signal, including many photoelectrons, can be expressed as an exponential function. As the integration interval is shortened, we obtain less number of p.e., and the fluctuation of digitization error is reduced as well. The signal is integrated with different intervals ranging from 4000 nsec down to 500 nsec to study the interval dependence of the fluctuation of digitization error. In this analysis, the energy histograms constructed by "partial photon counting", which is introduced in Chapter 6, with improved resolution are used to make the energy cut. The estimated fluctuations of digitization error at ^{40}K and ^{208}Tl peaks are plotted as a function of integration interval, as shown in Figure 4.10. The fluctuations of digitization error at these two peaks are attenuated as the integration interval reduced. At the interval of 4000 nsec, we obtain a small contribution of σ_{DE} on the energy resolution of these two peaks:

- at the γ-peak of ^{40}K, the σ_{DE} is 7.3 p.e., equivalent to $\sigma_{\mathrm{DE}}/\mathrm{E} \approx 0.55\%$;

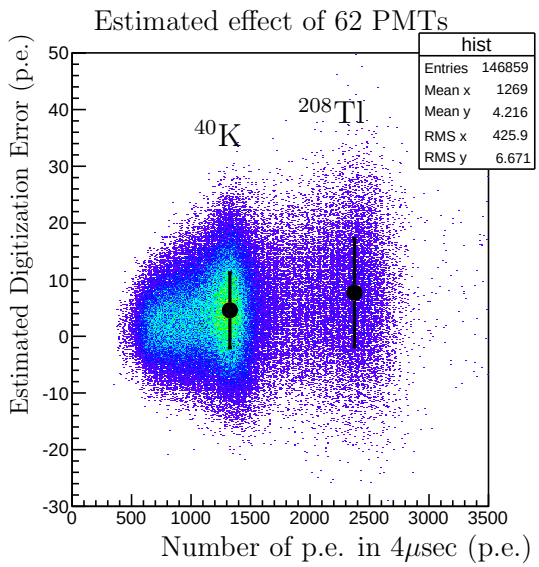

Figure 4.8: The estimated digitization error effect on the energy spectrum. The dependence of digitization error on the number of photoelectrons. The black filled-circle points are the estimated mean values of digitization error effects on the ^{40}K and ^{208}Tl γ-peaks. The error bars are the estimated fluctuations of digitization error effects on two γ-peaks.

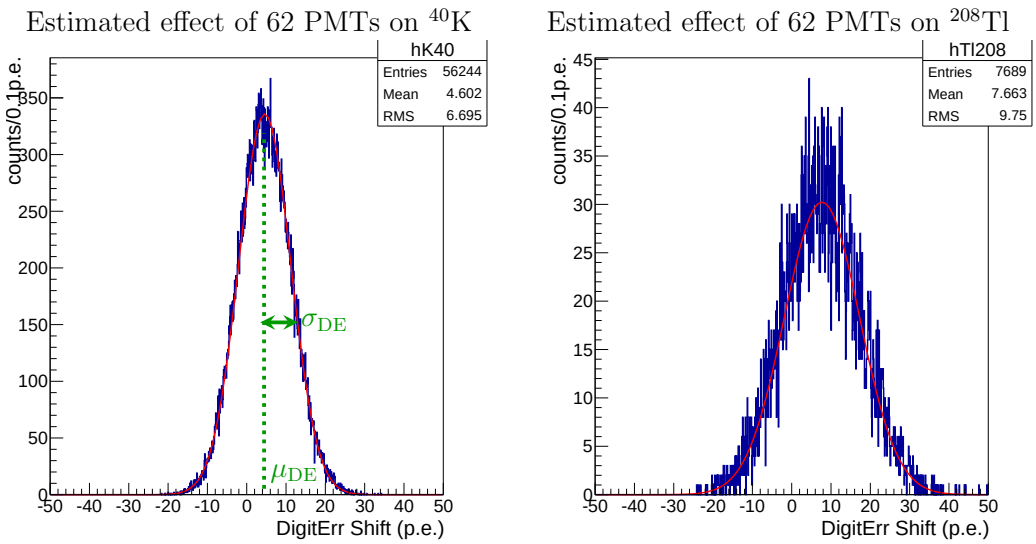

(a) Effect on ^{40}K peak **(b)** Effect on ^{208}Tl peak

Figure 4.9: The estimated digitization error at the ^{40}K (a) and ^{208}Tl peaks (b). The fluctuation of digitization error (σ_{DE}) contributes to the energy resolution, while the mean value (μ_{DE}) affects the peak position. The solid-red line is the Gaussian fitting to obtain σ_{DE} and μ_{DE}.

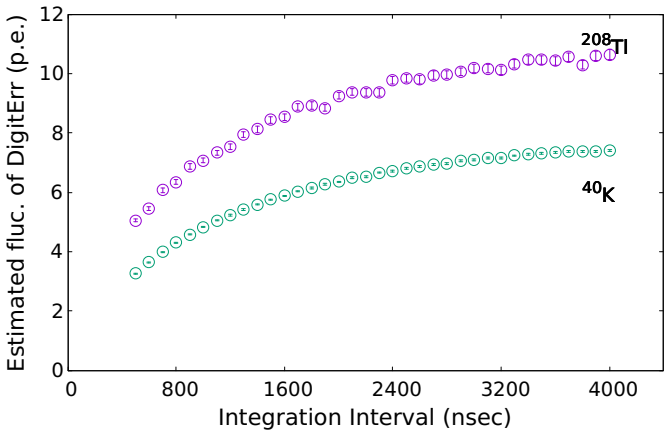

Figure 4.10: Estimated fluctuation of digitization error at ^{40}K (green) and ^{208}Tl (violet) peaks as a function of integration interval.

- at the γ-peak of ^{208}Tl, the σ_{DE} is 10.4 p.e., equivalent to $\sigma_{DE}/E \approx 0.44\%$.

At Q-value of ^{48}Ca, the contribution of digitization error on the energy resolution should be small.

4.3 Noise in 62 PMTs of CANDLES

4.3.1 Noise Analysis

As discussed, the pedestal values of all PMTs in CANDLES III are set at 244.5 ADC to minimize the effect of digitization error. However, at the pedestal of 244.5 ADC, another problem rising up is the noise [94, 95]. Every PMT baseline selected by Clock trigger is fitted with the following sine function to obtain the noise amplitude and cycle:

$$\mathrm{A(t)} = \mathrm{Offset} + \mathrm{A0} \times \sin\left(2\pi \frac{\mathrm{t} - \varphi}{\mathrm{T}}\right) \tag{4.4}$$

where A(t): is the amplitude of the sine-wave noise in ADC unit at timebin t of the waveform,

Offset: is equivalent to the pedestal value (ADC),

A0: is the amplitude of sine-wave noise at the beginning of the waveform (ADC),

T: is the cycle of sine-wave noise (nsec),

φ: is the phase factor of sine-wave noise (nsec).

Figure 4.11-a shows the fitting functions of PMT01's baseline; and Figure 4.11-b shows the fitting function of the sum baseline of twelve 10-inch PMTs. The noise cycles and amplitudes of 62 PMTs are plotted in Figure 4.12. In most of PMTs, the noise amplitudes are small. For 10-inch PMTs, the noise amplitudes are high, especially at PMT01, PMT05, PMT09, PMT25, and PMT29. The noise cycles in these 10-inch PMTs are around 730 nsec. The sum baseline of 10-inch PMTs is used to study the noise effect. Figure 4.13 shows the event-by-event distribution of the noise amplitude and the event-by-event distribution of the noise cycle obtained from fitting. As a result, the amplitude of the sum baseline is 0.726 ADC (equivalent to about 3 mV in FADC input), and the cycle is about 730 nsec (equivalent to the frequency of 1.37 MHz). Each PMT signal is amplified 10 times before it is fed into each FADC channel. The noise amplitude of the sum baseline of twelve 10-inch PMTs might be about 0.3 mV. The noise amplitude and cycle in the sum baseline are also plotted in Figure 4.12 for comparison. The higher amplitude of the sum baseline compared to the amplitudes of twelve 10-inch PMTs indicates the coherence of noise in 10-inch PMTs.

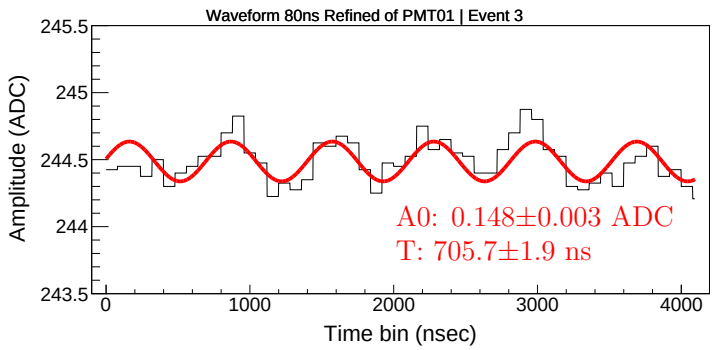

(a) PMT01 as one of 10-inch PMTs

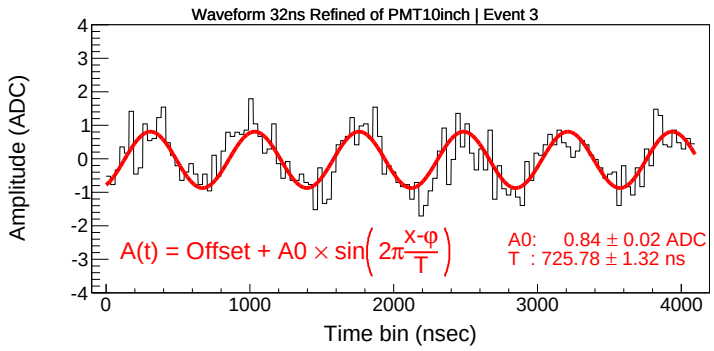

(b) Sum of twelve 10-inch PMTs

Figure 4.11: Fitting function on the baseline of PMT01 (a) and sum baseline of 10-inch PMTs (b).

4.3.2 Effect of noise in 10-inch PMTs

In this section, the effect of 730 nsec noise in the integration of CaF_2 signal is estimated. With the integration interval of 4000 nsec, the 730 nsec noise is not canceled in signal integration. To estimate the effect of 730 nsec noise in CaF_2 signal is not easily practical because the phase factor (mentioned in equation 4.4) in the sine function is random. The maximum effect of 730 nsec noise is estimated, and its dependence on the integration interval is also discussed. The effect of the 730 nsec noise in p.e. unit on the integration of CaF_2 signal can be calculated as:

$$\begin{aligned}\mathrm{Effect_{noise}} &= \frac{1}{\bar{\mu}_{\mathrm{p.e.}}}\int_0^{\mathrm{T_{INT}}} \mathrm{A}\times\sin\left(2\pi\frac{\mathrm{t}-\varphi}{\mathrm{T}}\right)\mathrm{dt} \\ &= \frac{\mathrm{AT}}{\pi\bar{\mu}_{\mathrm{p.e.}}}\sin\left(\pi\frac{\mathrm{T_{INT}}}{\mathrm{T}}\right)\sin\left(\pi\frac{\mathrm{T_{INT}}-2\varphi}{\mathrm{T}}\right)\end{aligned}$$

where $\mathrm{T_{INT}}$: is the integration interval (nsec),

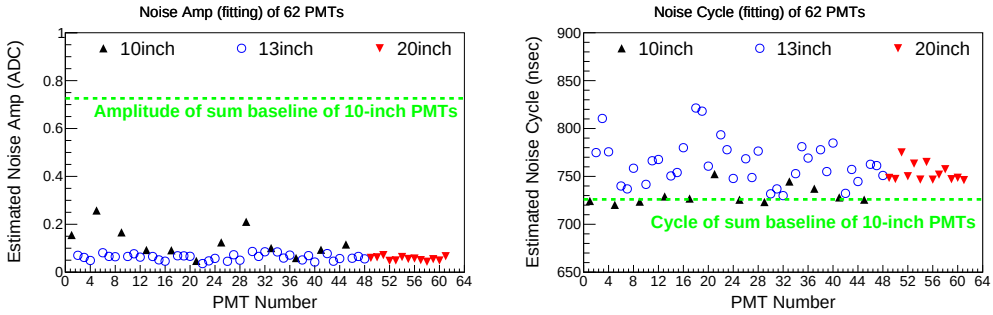

(a) Noise Amplitudes of 62 PMTs **(b)** Noise Cycles of 62 PMTs

Figure 4.12: Noise amplitude and noise cycle obtained by fitting of 62 PMTs. The results of 10-inch, 13-inch, and 20-inch PMTs are respectively plotted with black up-triangles, blue circles, and red down-triangles. Most of the noises have small amplitudes; the noise amplitudes in 10-inch PMTs are significantly higher.

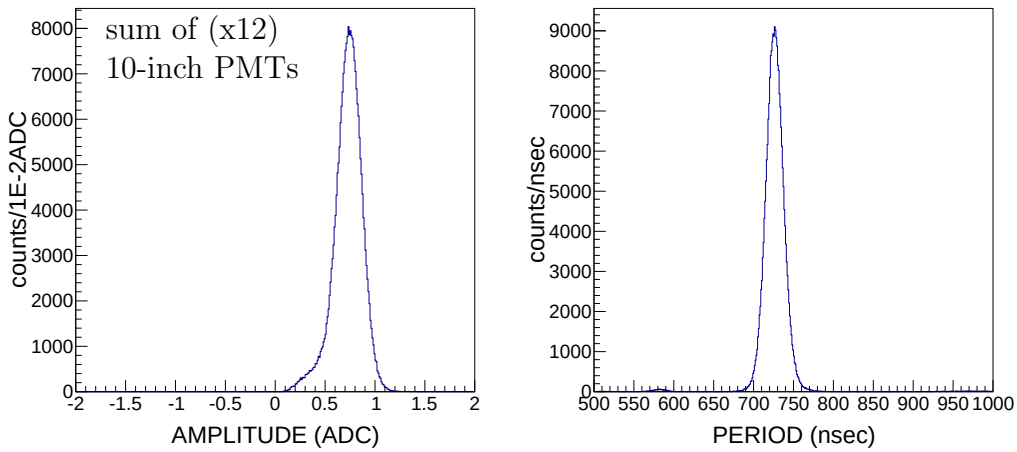

(a) Noise Amplitude **(b)** Noise Cycle

Figure 4.13: Distributions of the amplitude and cycle of 730 nsec noise by fitting the sum baseline of 10-inch PMTs (using Clock events). The data is taken in a one-day measurement.

$\bar{\mu}_{\text{p.e.}}$: is the average 1p.e. charge of 62 PMTs (ADC/p.e.),

A: is the amplitude of the 730 nsec noise (ADC),

T: is the noise cycle (730 nsec),

φ: is the phase of 730 nsec noise (nsec).

Figure 4.14 shows the distributions of $\mathrm{Effect_{noise}}$ with different integration intervals. The $\mathrm{Effect_{noise}}$ is a sine wave function, and the peak-to-peak amplitude is the full width of $\mathrm{Effect_{noise}}$ distribution. The maximum fluctuation induced by 730 nsec noise is the full width of $\mathrm{Effect_{noise}}$ distribution divided by $2\sqrt{2}$, and it is a function of an integration interval T:

$$\sigma_{\mathrm{noise}}(\mathrm{T}) = \frac{\mathrm{AT}}{\sqrt{2}\pi\bar{\mu}_{\mathrm{p.e.}}}\left|\sin\left(\pi\frac{\mathrm{T_{INT}}}{\mathrm{T}}\right)\right| \tag{4.5}$$

The maximum fluctuation (σ_{noise}) is canceled at the integration interval which is a multiple of the noise cycle, and it is maximized at the integration interval which is a multiple of a half of the cycle. Figure 4.15 shows the maximum effect of the 730 nsec noise as a function of the integration interval. The circle points are the results of σ_{HF} estimated from the $\mathrm{Effect_{HF}}$ distributions with different integration intervals, and the red-solid line is the theoretical plot using equation 4.5.

In summary, the noise from 10-inch PMTs with a cycle of 730 nsec has a high amplitude. From the estimation, the effect of noise on the waveform depends on the integration interval. At the integration interval of 4000 nsec, the maximum fluctuation caused by 730 nsec noise is about 2 p.e. At high energy peaks, the effect of 730 nsec noise to the energy resolution is negligible:

- at the γ-peak of ^{40}K, the 730 nsec noise effect is $\sigma_{\mathrm{noise}}/\mathrm{E} \leq 0.15$ %;
- at the γ-peak of ^{208}Tl, the 730 nsec noise effect is $\sigma_{\mathrm{noise}}/\mathrm{E} \leq 0.08$ %;

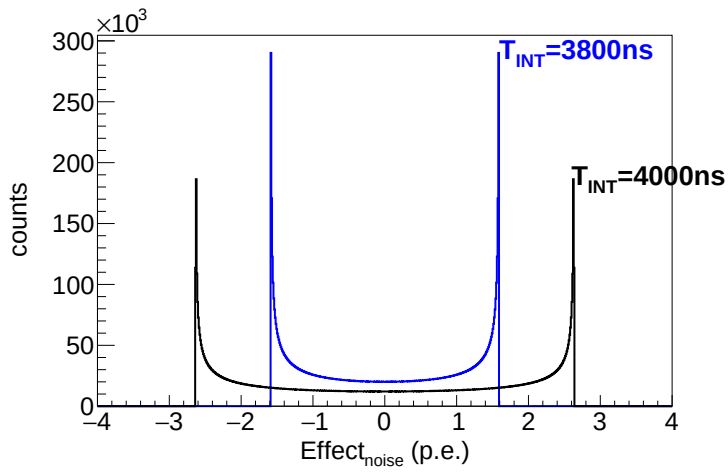

Figure 4.14: The $\mathrm{Effect_{noise}}$ distributions are plotted with different integration intervals of 3800 nsec (blue) and 4000 nsec (black).

- at the Q-value of ^{48}Ca, the 730 nsec noise effect is $\sigma_{\mathrm{noise}}/\mathrm{E} \leq 0.05$ %.

4.4 Error of baseline measurements

In the above sections, several sources of the baseline fluctuations are checked. The dark current and noises in baseline are both negligible, and the fluctuation of digitization error is estimated to be small. In this section, the error of baseline measurement is found to be the most severe fluctuation in 4 μsec signal integration of CaF_2 signal.

4.4.1 Uncertainty of pedestal value

In this thesis, the pedestal of each PMT is calculated as the average value of the first 40 data points, which are equivalent to 80 nsec, of the waveform. The measurement of the pedestal distributes as a binomial distribution of 40 trials and the obtained value is 244 ADC or 245 ADC in each trial. The probability P(r) to obtained r times of 245 ADC in N trials is expressed as:

$$\mathrm{P(r)} = \frac{\mathrm{N!}}{\mathrm{r!(N-r)!}}\mathrm{p^r(1-p)^{N-r}} \tag{4.6}$$

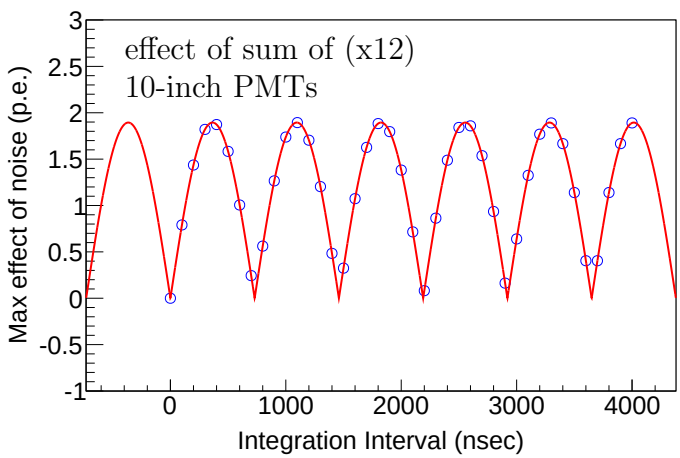

Figure 4.15: The fluctuation from 730 nsec noise as a function of the integration interval. The circles mark some random values from 0 nsec to 4000 nsec. The red line is plotted using equation 4.5.

With the mean ($\langle r \rangle$) and standard deviation (σ_r) of the distribution, the measured pedestal is obtained as the average of 40 data points:

$$\text{Measured Pedestal} = 244 + \frac{\langle r \rangle}{N} = 244 + p,$$

and the uncertainty of measured pedestal of one PMT is:

$$\sigma^{iPMT}_{PedStat} = \frac{\sigma_r}{N} = \frac{\sqrt{Np(1-p)}}{N} = \sqrt{\frac{p(1-p)}{N}} \tag{4.7}$$

The $\sigma^{iPMT}_{PedStat}$ in equation 4.7 is the statistical uncertainty of pedestal value. If the waveform is affected by noise, the obtained σ_{ped} is bigger than the statistical uncertainty. For more details of the pedestal uncertainty affected by noise, on can check appendix E.

Figure 4.16 shows the statistical uncertainties and measured uncertainties of pedestal as a function of measured pedestals using data from 62 PMTs. The measured uncertainties are bigger than the statistical uncertainties. It may be because of the noise affecting the baseline. The pedestal uncertainty of sum waveform of 62 PMTs is:

$$\sigma^{sum}_{PedErr} = \sqrt{\sum_{iPMT} (\sigma^{iPMT}_{PedErr})^2} \tag{4.8}$$

4.4.2 Error accumulation of the signal integration

The signal integration is calculated as $N \times Ped - \sum_i^N Signal[i]$, where N is the number of data points. For a 4000 nsec integration, the number of data points is 2000. The accumulated fluctuation of pedestal uncertainty of a PMT is interpreted as:

$$\sigma'^{iPMT}_{PedErr} = N \times \sigma^{iPMT}_{PedErr} \tag{4.9}$$

where σ'^{iPMT}_{PedErr}: the pedestal uncertainty accumulated in signal integration of the ith PMT,

σ^{iPMT}_{PedErr}: the pedestal uncertainty of the ith PMT.

More points of integration causes the larger error. The pedestal uncertainty in signal integration of each PMT can be probed by making the baseline integration. Figure 4.17 shows the baseline fluctuation in PMT27 as a function of integration interval. A linear fitting is applied to estimate the fluctuation.

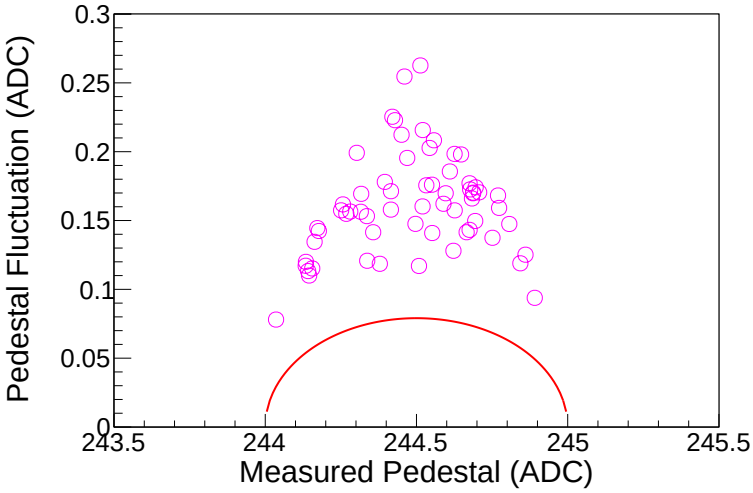

Figure 4.16: The σ_{Ped} of pedestal is plotted as a function of measured pedestal with 40 data points using measured and theoretical values of 62 PMTs. The red-solid line is the theoretical function in equation 4.7. The magenta circles are the measured σ_{PedErr}.

At interval of 4000 nsec, the accumulated fluctuation of pedestal uncertainty in the baseline of PMT27 is about 4 p.e.

In the sum waveform of many PMTs, the fluctuation uncertainty of

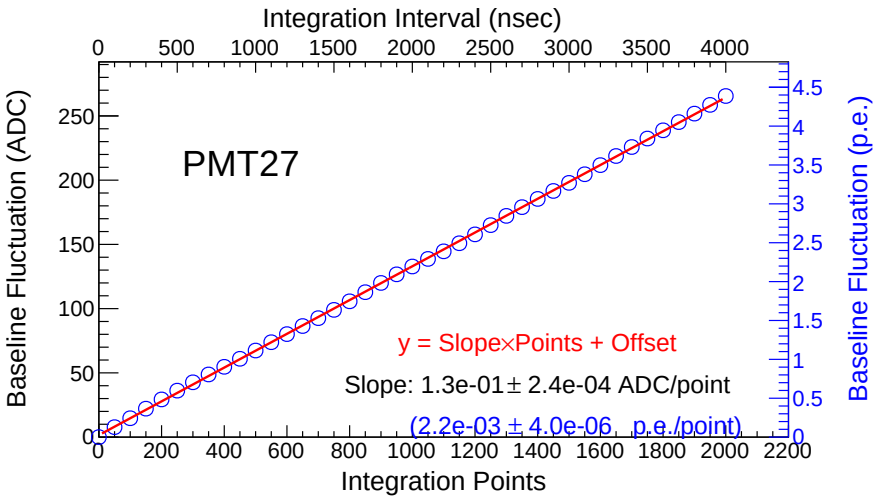

Figure 4.17: The accumulated fluctuation estimated by baseline integration in the waveform of PMT27 as a function of integration interval.

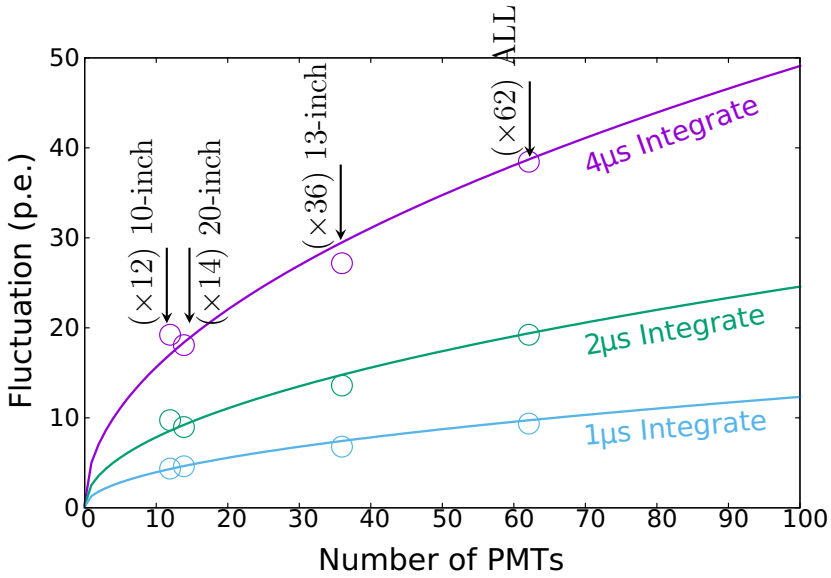

Figure 4.18: The pedestal fluctutaion as a function of number of PMTs in different integration intervals. The circles are the data of 10-inch PMTs, 13-inch PMTs, 20-inch PMTs and 62 PMTs. The solid line is the calculation of $\sqrt{\mathrm{N_{PMT}}} \times \bar{\sigma}_{\mathrm{PedErr}}$, with $\bar{\sigma}_{\mathrm{PedErr}}$ is estimated from the fluctuation of 62 PMTs.

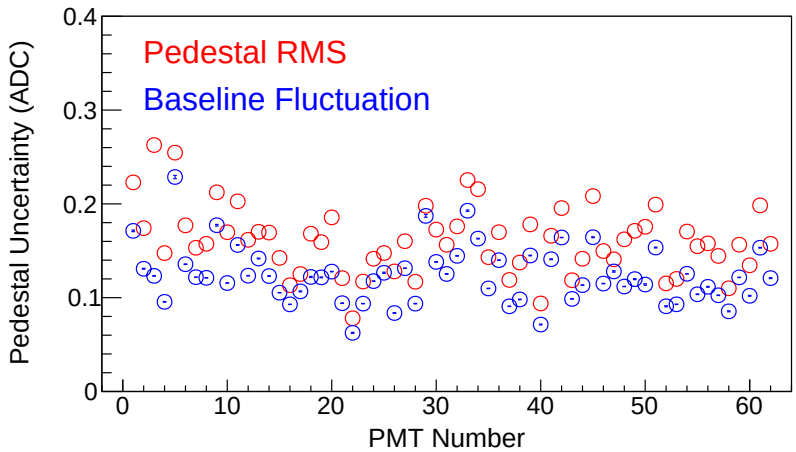

Figure 4.19: Compare the uncertainties from pedestal measurements and fitting for all PMTs.

pedestal is amplified as $\sqrt{\mathrm{N_{PMT}}} \times \bar{\sigma}_{\mathrm{PedErr}}$, where $\mathrm{N_{PMT}}$ is the number of PMTs, and $\bar{\sigma}_{\mathrm{PedErr}}$ is the average fluctuation of pedestal in one PMT. Figure 4.18 shows the accumulated fluctuation in the sum waveform of 10-inch

PMTs, 13-inch PMTs, 20-inch PMTs and 62 PMTs with different integration intervals of 1 μsec, 2 μsec and 4 μsec. As the fluctuation depends on the number of PMTs, the fluctuation of twelve 10-inch PMTs is close to the fluctuation of fourteen 20-inch PMTs, and lower than the fluctuation of thirty-six 13-inch PMTs and 62 PMTs. It should be noticed that the baseline integration includes the noise effect, which is negligibly small compared to the uncertainty of pedestal. The baseline fluctuation should be close to the pedestal uncertainty estimated in section 4.4.1. Figure 4.19 shows the comparison of these two values for all PMTs. The estimated values obtained by fitting are quite consistent with the expected uncertainty. The accumulated fluctuation of 62 PMTs is about 38.6 p.e. at an integration interval of 4000 nsec. As the accumulated pedestal uncertainty affects in the same way on the CaF_2 signal, the effect of accumulated pedestal uncertainty at different energy peaks is estimated:

- at ^{40}K peak, σ_{PedErr}/E is 2.8 %;
- at ^{208}Tl peak, σ_{PedErr}/E is 1.6 %;
- at Q-value of ^{48}Ca, σ_{PedErr}/E is 1 %;

Comparing to the statistical fluctuations (2.7 % at ^{40}K, 2.0 % at ^{208}Tl, 1.6 % at Q-value of ^{48}Ca), this fluctuation causes a severe effect on the energy resolution.

4.5 Summary of baseline fluctuations

The energy resolution can be affected by the baseline fluctuation. In the experiments with short decay constant scintillator, this baseline fluctuation is negligible. In CANDLES, due to the long decay constant of CaF_2, the signal is integrated with the 4000 nsec interval to estimate the obtained energy. The baseline fluctuation is accumulated and affects the energy resolution of the CANDLES detector. In this chapter, the dark current (section 4.1) and the baseline fluctuations are discussed: the digitization error (section 4.2), the 730 nsec noise (section 4.3), and the pedestal uncertainty (section 4.4).

All of these fluctuations depend on the integration interval. Figure 4.20 shows the fluctuations caused by dark current (σ_{DC}), digitization error (σ_{DE}), noises in baseline (σ_{noise}), and pedestal uncertainty (σ_{PedErr}). According to the analysis, σ_{DE}, σ_{DC} and σ_{PedErr} are attenuated when the integration interval is shorten. Table 4.1 indicates the statistical fluctuation, and all fluctuations discussed in this chapter at the integration interval of 4000 nsec. In the

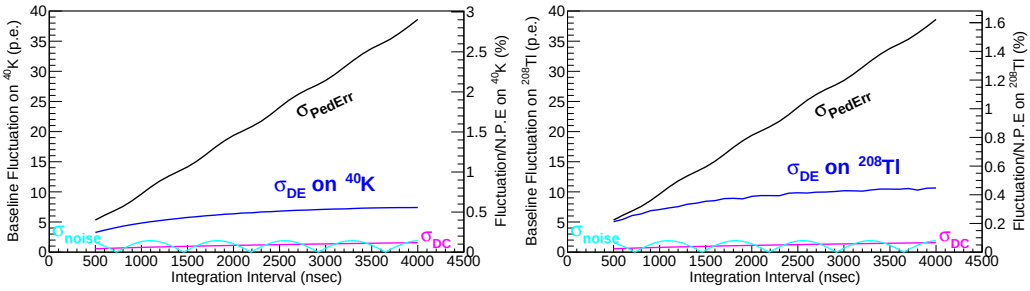

(a) Fluctuation in baseline at ^{40}K peak **(b)** Fluctuation in baseline at ^{208}Tl peak

Figure 4.20: The baseline fluctuation at ^{40}K peak (a) and ^{208}Tl peak (b) as a function of integration interval. Fluctuations from dark current, digitization error, error in baseline measurement and maximum fluctuation of 730 nsec noise are respectively plotted with magenta, blue, black and cyan lines.

Table 4.1: The statistical fluctuation ($\sigma_{\mathrm{p.e.}}$), and all factors of baseline fluctuation (σ_{DE}, σ_{HF}, σ_{DC} and σ_{PedErr}) on energy resolutions.

	^{40}K peak 1460.822 keV	**^{208}Tl peak 2614.511 keV**	**^{48}Ca Q-value 4272 keV**
$\sigma_{\mathbf{p.e.}}$ ($\sigma_{\mathbf{p.e.}}/\mathrm{N}_{\mathbf{p.e.}}$)	36.5 p.e. (2.7 %)	48.8 p.e. (2.0 %)	62.3 p.e. (1.6 %)
$\sigma_{\mathbf{DC}}$ ($\sigma_{\mathbf{DC}}/\mathrm{N}_{\mathbf{p.e.}}$)	1.6 p.e. (0.1 %)	1.6 p.e. (0.06 %)	1.6 p.e. (0.004 %)
$\sigma_{\mathbf{noise}}$ ($\sigma_{\mathbf{noise}}/\mathrm{N}_{\mathbf{p.e.}}$)	$\leq$2 p.e. ($\leq$0.15 %)	$\leq$2 p.e. ($\leq$0.08 %)	$\leq$2 p.e. ($\leq$0.05 %)
$\sigma_{\mathbf{DE}}$ ($\sigma_{\mathbf{DE}}/\mathrm{N}_{\mathbf{p.e.}}$)	7.3 p.e. (0.6 %)	10.41 p.e. (0.4 %)	N/A (small)
$\sigma_{\mathbf{PedErr}}$ ($\sigma_{\mathbf{PedErr}}/\mathrm{N}_{\mathbf{p.e.}}$)	38.6 p.e. (2.9 %)	38.6 p.e. (1.6 %)	38.6 p.e. (1.0 %)

table, the digitization error at Q-value is not estimated, but its contribution to the energy resolution should be negligible.

Among the fluctuations in a long integration interval, the error in pedestal measurement (σ_{PedErr}) is the most dominant factor on the energy resolution, the contributions of σ_{DE} and σ_{DC} are small. As the non-negligible baseline fluctuation is accumulated in signal integration, an alternative way is needed to calculate the energy instead of signal integration. Photon counting method is a common technique used in the experiments with a long decay constant scintillator to avoid the fluctuations from the baseline. In this thesis, this

technique is introduced for the first time in CANDLES to minimize the effect from the baseline fluctuation. The DAQ setup and the data analysis for this method are discussed in Chapter 5 and Chapter 6, respectively.

Chapter 5

Measurement at Kamioka Underground Observatory

The baseline fluctuation discussed in Chapter 4 has a non-negligible effect on the energy resolution. In the current data analysis, baseline fluctuation is accumulated in long signal integration. The photon counting method is used in the CANDLES detector to avoid this fluctuation. In this chapter, the DAQ setup for photon counting and parameters for further offline analysis are introduced.

5.1 DAQ setup for photon counting

5.1.1 DAQ setup for photon counting

The photon counting method has been used widely in nuclear and particle physics experiments. In this research, the waveform is recorded, and the 1p.e. signals are counted in offline analysis. The widths of 1p.e. signals are all less than 50 nsec (Figure D.3). As mentioned in section 2.2.4, the waveform contains eight-bits data points, which are recorded every 2 nsec in the first 768 nsec, and 128 sixteen-bits data points, which are the sum of 64 nsec digitized values. With this FADC setting, it is impossible to see the 1p.e. signals if they rise after 768 nsec. Thus, the region for recording 2 nsec data should be maximized. Due to the limit of event buffer size, the FADC setting is adjusted to 2044 points of eight-bits data and 2 points of sixteen-bits data for photon counting measurement. The summary of the FADC setting for photon counting is indicated in Table 2.3. The total data size for photon counting data-taking is three times larger than the size of Physics Run data, while the waveform interval of photon counting data is 4216 nsec, shorter

than the Physics Run interval of 8960 nsec. The photon counting is carried out with the same trigger conditions in Physics Run.

The DAQ software must be modified for maximizing the 2 nsec data region to carry out the measurement. Figure 5.1 shows the DAQ Middleware setup for Physics Run (a) and the setup for Photon Counting measurement (b). Thanks to previous developments [64, 65], only the Fast Reader component reading data from μTCA modules in the DAQ Middleware has to be modified for this purpose. Since it is the first time that photon counting is carried out in CANDLES, only the most necessary components are used for Photon Counting measurement. An event monitor is not prepared in Photon Counting measurement; thus, the sum waveform of 62 PMTs is checked every 15 minutes by the offline analysis. Figure 5.2 shows the difference of the waveform taken in Physics Run (red) and Photon Counting measure-

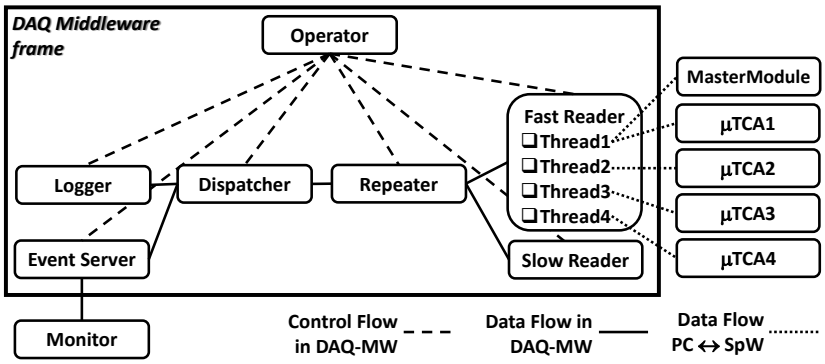

(a) DAQ Middleware for Physics Run

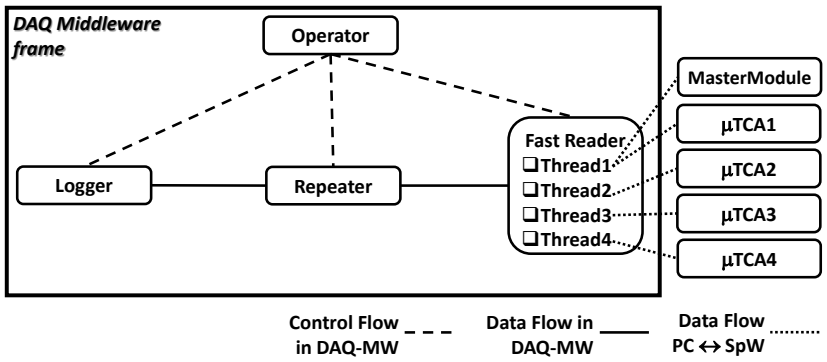

(b) DAQ Middleware for Photon Counting

Figure 5.1: The DAQ Middleware configuration for Physics Run of CANDLES (a) and Photon Counting (b). The Fast Reader component in Photon Counting is adjusted to maximize 2 nsec data region.

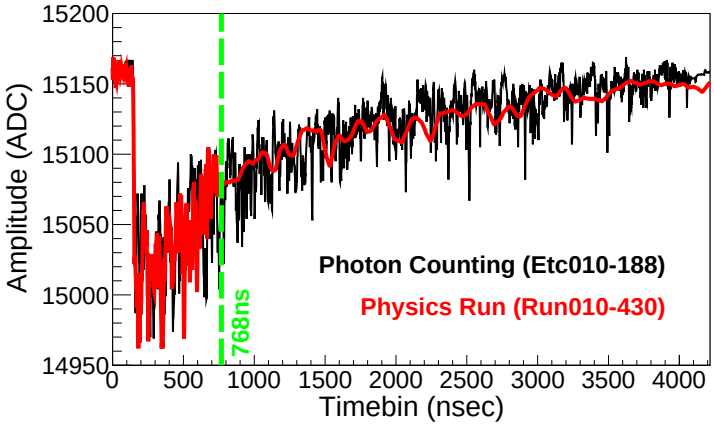

Figure 5.2: The different waveforms in Photon Counting and Physics Run measurements. Each waveform is selected from raw data with the same cut conditions of signal integration, charge ratio, trigger condition. In Physics Run, the waveform is recorded every 2 nsec up to 768 nsec (green-dashed line), and the remaining part is recorded as sum data in every 64 nsec. In Photon Counting, the waveform up to 4088 nsec is recorded at 2 nsec/sample.

ment (black). These two signals are chosen with the same cut conditions of signal integration, charge ratio for Pulse Shape Discrimination, and Dual-Gate trigger condition. After the first 768 nsec, the Physics Run waveform is smoother than the Photon Counting waveform because the data in this region is taken average for every 64 nsec. The photon counting measurement was carried out with 3 Sub Runs in total real time of about 70 hours (from December 4th to 6th, 2017).

5.1.2 Data taking efficiency in photon counting measurement

As the data size is extended three times larger in photon counting measurement, the DAQ readout time is extended. The readout time consists of the readout time of small-size registers and waveform data, and it can be estimated using data in previous research [65]. Figure 5.3 shows the readout time as a function of data size [65]. From these data, the readout time of the photon counting can be estimated as 20 msec, which is two times longer than the readout time in Physics Run. The data taking efficiency can be calculated as a function of the number of event buffers, readout time, and the trigger rate [65]. Figure 5.4 shows the data taking efficiencies calculated with one and eight event buffers are plotted as a function of trigger rate.

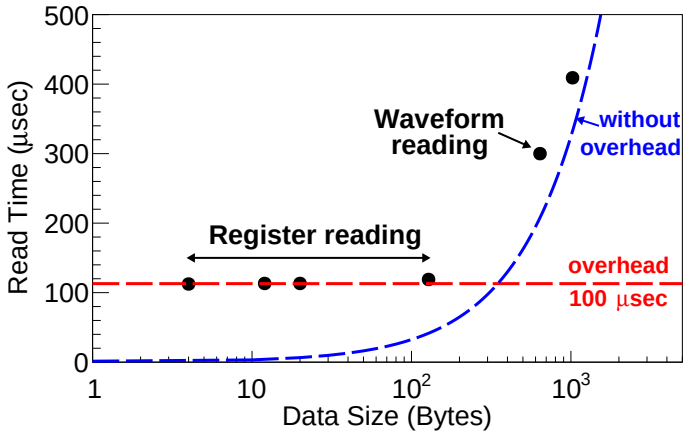

Figure 5.3: The read time at every packet size was measured. There is an overhead due to the long waiting-reply time [65]. The waveform reading in Physics Run is 640 Bytes (shown in the above graph), and it is 2048 Bytes in Photon Counting measurement.

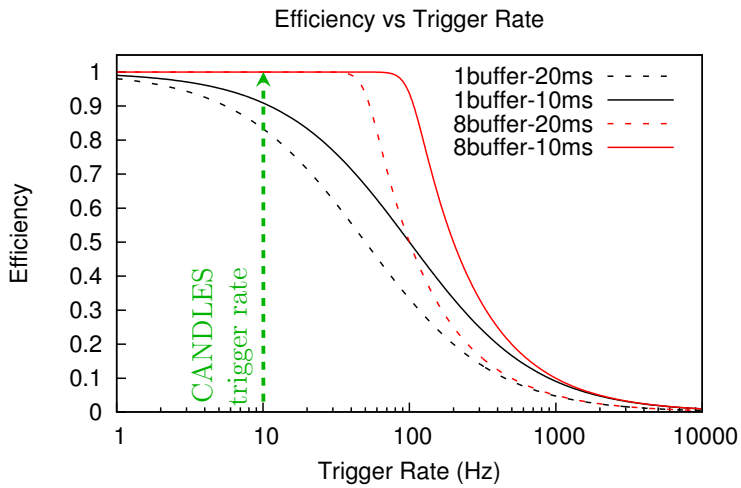

Figure 5.4: Estimated data-taking efficiency as a function of trigger rate with different number of event buffers and readout times. Using eight event buffers, the data taking efficiencies with the readout times of 10 msec and 20 msec are about 100 % at the trigger rate of 10 cps.

The readout times in the Physics Run (10 msec) and in Photon Counting measurement (20 msec) are used in this calculation. The data efficiency is reduced at the longer readout time, but enhanced with more event buffers.

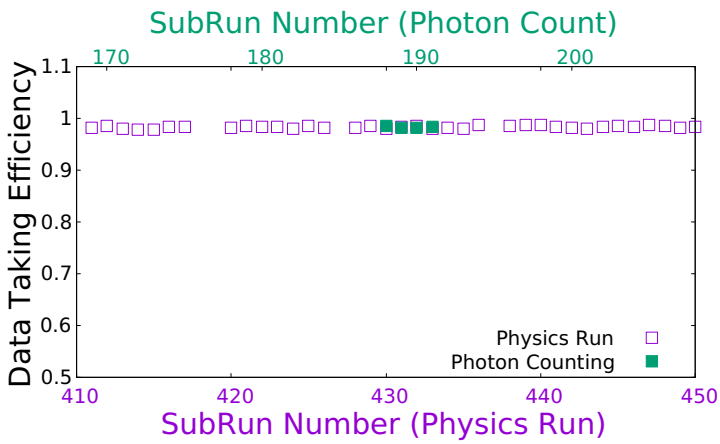

Figure 5.5: The obtained data taking efficiency as division of recorded events by incident events. The violet and green squares are the efficiencies obtained in Physics Run and Photon Counting measurement, respectively.

With eight event buffers, the calculated efficiencies with both readout times are almost 100 % at the current CANDLES trigger rate of 10 cps.

The data taking efficiency is evaluated by the number of recorded events divided by the number of incident events. The efficiencies in Physics Run and Photon Counting measurement are plotted in Figure 5.5. The efficiencies in both measurements are nearly 100 % as it is expected. With the current CANDLES detector setup, we can conclude the efficiency of data taking in Photon Counting is the same in the Physics Run at the random trigger rate of 10 cps. However, one should note that the big data size per event is the disadvantage of Photon Counting measurement, and its readout time also results in the DAQ speed as 50 cps, which is two times slower than the DAQ speed in Physics Run.

5.2 Event Reconstruction for Photon Counting measurement

As discussed in the previous chapter, the signals of double beta decay inside CaF_2 crystals are preferable events. However, during data taking, many unexpected events may be obtained. In order to construct the energy histogram, those unexpected events are rejected in offline analysis. In CANDLES, the raw data taken by the DAQ system is sequentially analyzed by two analysis tools, which are PreAnalysis and CANDLES Analysis Tool (CAT). In order to make a ready-to-use analysis, the photon counting analysis is im-

plemented in these 2 tools for counting photoelectrons (PreAnalysis), energy reconstruction (CAT), and other analyses. The details of photon counting analysis is introduced in Chapter 6. In this section, the parameters used for event reconstruction are discussed. These parameters are discussed in details elsewhere [62, 73]; however, since the waveform in photon counting measurement is different, it is needed to recheck these parameters.

5.2.1 Data Quality check

All waveforms are reconstructed after timing correction, which is explained elsewhere [73]. An good example of CaF_2 events can be seen in Figure 5.2, and Figure 5.6 shows the examples of bad events. These bad events cannot be avoided by our trigger system, and they consist of:

- Saturated event: the signal's peak is exceeded the dynamic range of FADC as it shown in Figure 5.6-(a),
- Overshoot event: a part of the waveform crosses over the baseline as it shown in Figure 5.6-(b),

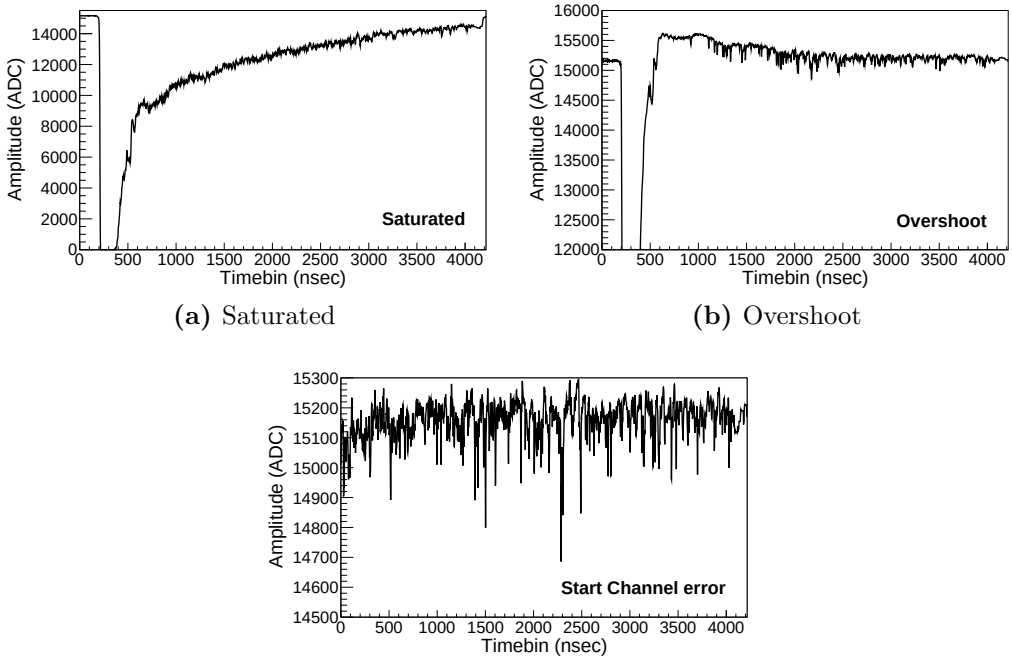

(a) Saturated **(b)** Overshoot

(c) Start Channel error

Figure 5.6: Bad waveform examples: Saturated (a), Overshoot (b), and Start Channel error (c).

- Start Channel error event: there is no Start Channel found as it shown in Figure 5.6-(c).

Fortunately, these bad events can be identified and rejected by the waveform analysis in the PreAnalysis tool.

5.2.2 Pulse Shape Discrimination by Charge Ratio

The dual-gate trigger is introduced to the select the CaF_2 events; however, other backgrounds can be accidentally selected. These background events consist of the CaF_2+LS events, which are mostly generated by the γ-ray from the external background, and the α-ray events, which are generated by the impurities inside the crystals. In current CANDLES analysis, the Pulse Shape Discrimination (PSD) proceeds by fitting each waveform with the reference waveform of α-event, β-event, and β+LS-event [62, 73]. The χ^2_β, χ^2_α, $\chi^2_{\beta+\mathrm{LS}}$ obtained from the fitting are used to select different events. Due to the difference of waveform intervals, the reference pulses, and the χ^2_{PSD} (PSD is α, β or β+LS) parameters should be studied to identify different events in Photon Counting measurement. It requires many events to construct the reference pulses [62], but the data obtained in Photon Counting measurement is not enough for the PSD study. Thus, it is decided to use other ways to reduce the number of unexpected events.

In this research, the energy spectrum of γ-ray deposited inside CaF_2 is used to study the energy resolutions; hence, α-events and CaF_2+LS events should be removed. The impurities in some crystals in CANDLES are much

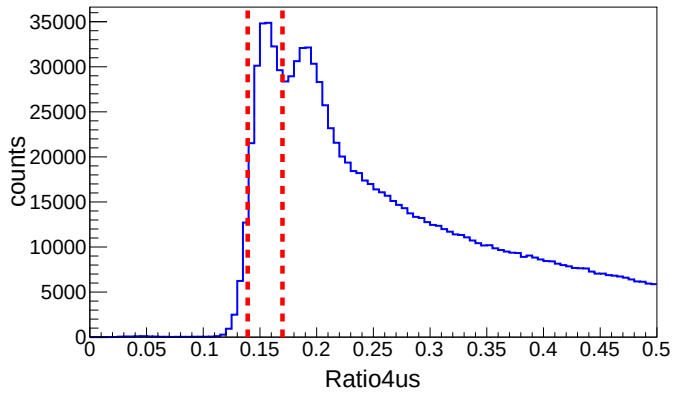

Figure 5.7: Distribution of Charge Ratio, which is equivalent to the ratio of the signal integration in the first 200 nsec and the integration in 4000 nsec. The red-dashed lines mark the range of charge ratio for selecting CaF_2 events.

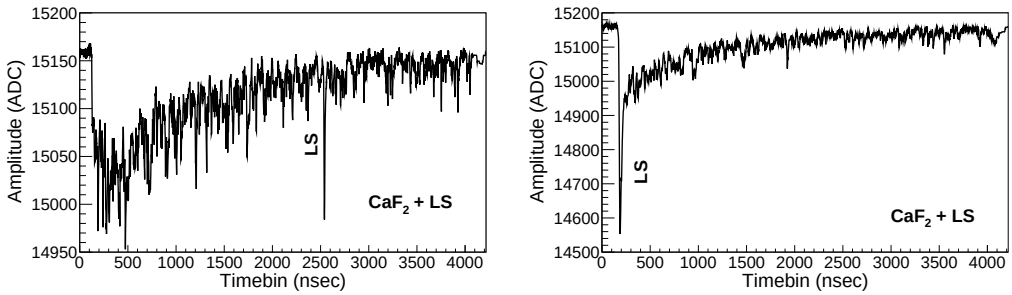

(a) CaF_2 + LS: Ratio4us<0.14 **(b)** CaF_2 + LS: Ratio4us>0.17

Figure 5.8: Examples of CaF_2+LS signals with LS signal in the tail part of CaF_2 signal (a), and LS signal in the prompt part of CaF_2 (b). The charge ratio can reject all of these events.

higher compared to the other [73]. The low-impurity crystals are selected using event position reconstruction, which is introduced in section 5.2.5, to reduce the α-events. The CaF_2+LS events are reduced using the charge ratio obtained by dividing the signal integration in the first 200 nsec by the integration in 4000 nsec. The distribution of charge ratio is plotted in Figure 5.7. Figure 5.8 shows two examples of CaF_2+LS signal accidentally recorded by the Dual-Gate trigger: LS signal in the tail part (a) and the prompt part (b). The CaF_2+LS events mentioned above are selected using the charge ratio of less than 0.14 and more than 0.17, respectively. The charge ratio cut from 0.14 to 0.17 is used to reduce the CaF_2+LS events.

5.2.3 Start Channel

The integration interval of 4000 nsec is used to study the improvement of energy resolutions using the photon counting method (chapter 6). In Photon Counting measurement, the waveform interval is only $\sim$4.2 μsec. If the start channel of the sum waveform of 62 PMTs exceeds 200 nsec, the waveform is not successfully integrated in 4000 nsec. The distribution of start channel is plotted in Figure 5.9 with cut conditions of event data quality, charge ratio, and the dual-gate trigger. The maximum start channel is about 200 nsec; thus, the signal integration of 4000 nsec can be performed in photon counting measurement.

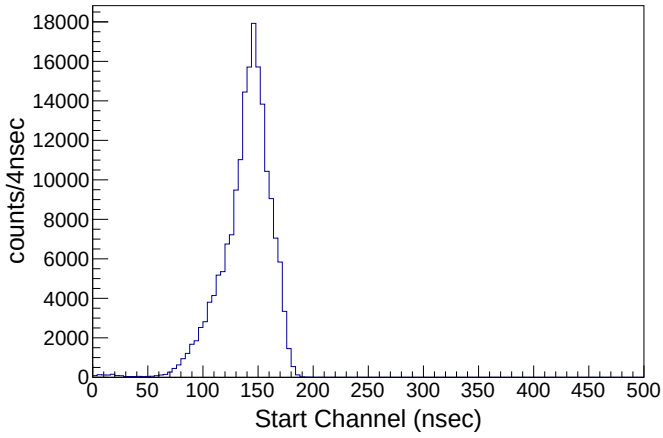

Figure 5.9: Distribution of the start channel of the sum waveform of 62 PMTs. The maximum start channel is about 200 nsec.

5.2.4 Charge of single photoelectron

The charge of 1p.e. (in ADC unit) is essential to estimate the number of photoelectrons obtained in every PMT for every event. The charge of 1p.e. is estimated by making the integration of 120 nsec around 1p.e. signal (60 nsec on the left side and the right side of the signal peak). The 1p.e. values in Run010-429, which is taken one day before the photon counting measurement, is used. Figure 5.10 shows the values of 1p.e. charge of 62 PMTs. All charge values are ranging from 50 to 80 ADC. These values are used in section 4.2 to estimate the number of photoelectrons.

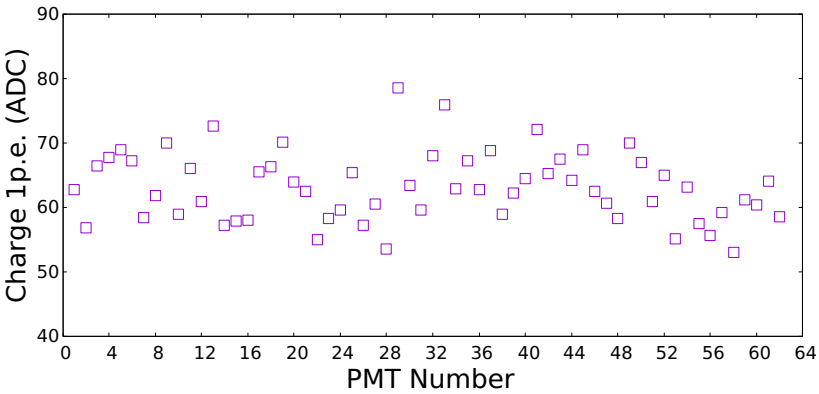

Figure 5.10: Charge of single photoelectron of 62 PMTs.

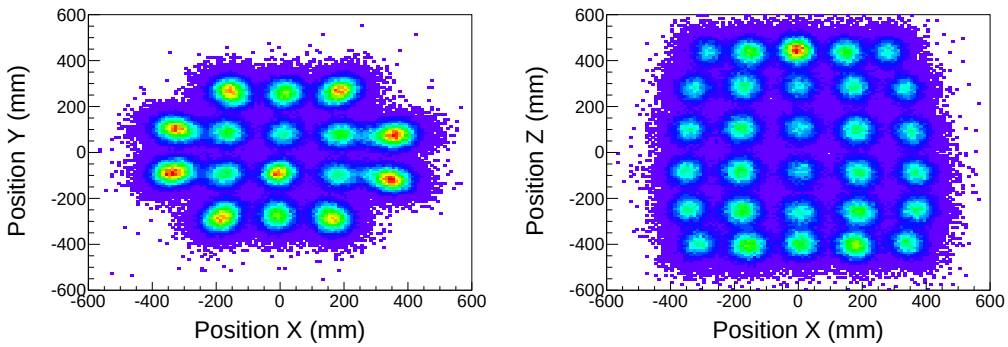

(a) Position Y -vs- Position X **(b)** Position Z -vs- Position X

Figure 5.11: Two-dimensional distributions of event positions in CaF_2 crystals. We may see events generated from 96 crystals arranged in 6 layers (a) and 16 crystals in each layer (b).

5.2.5 Event Position Reconstruction

The energy deposited in a crystal n is calculated by following equation Energy $= F_n \times \sum_{i=1}^{62} n^i_{p.e.}$. The $n^i_{p.e.}$ is the number of photoelectrons of ith PMT. F_n is the energy calibration factor, depends on the light yield. The light yield of each CaF_2 crystal is different. Thus, reconstruction of event position is crucial in CANDLES for calculating the energy. To determine the event position, we use the weight-mean method of the number of photoelectrons as expressed in the following equation:

$$\vec{r} = \frac{\sum_i n^i_{p.e.} \times \overrightarrow{pmt^i}}{N_{p.e.}}$$

where $\vec{r}$: is the position vector (x, y, z),

i: is the ith PMT,

$n^i_{p.e.}$: is the number of photoelectrons in the ith PMT,

$\overrightarrow{pmt^i}$: is the position vector of the ith PMT,

$N_{p.e.}$: is the total photoelectrons obtained in 62 PMTs.

Figure 5.11 shows the event positions in Y and X axes (a), and Z and X axes (b). The Figure 5.11-(a) is the crystals arrangement in each layer as it shown in Figure 2.5, and Figure 5.11-(b) shows 6 layers of crystals distributed

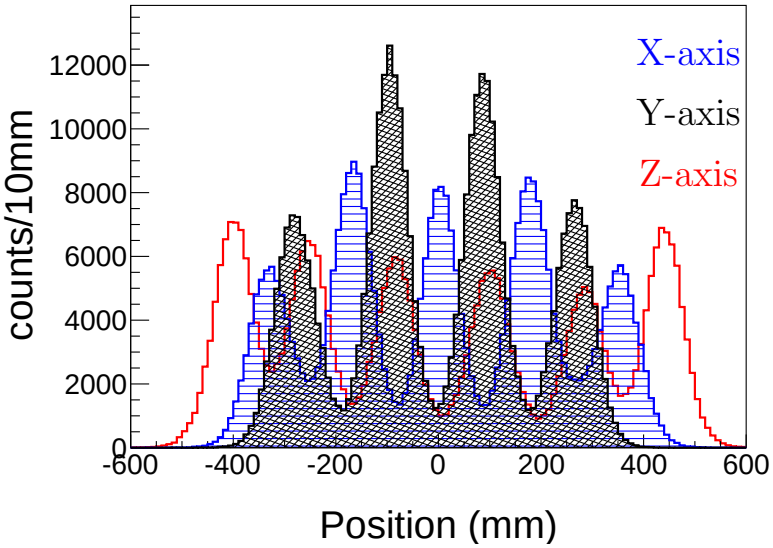

Figure 5.12: Distributions of event positions in X-, Y-, Z- axes. There are five peaks in X-dimension, four peaks in Y-dimension, and six peaks in Z-dimension.

vertically. Figure 5.12 shows the distributions of X, Y and Z axes. According to the crystal layout, there are five peaks in X-dimension, four peaks in Y-dimension, and six peaks in Z-dimension.

Using the above method, one can select the events occurring in one specific crystal using a position table of 96 crystals in CANDLES. The volume around the center of each crystal can be selected as 0.5σ, 1σ, 2σ, or 3σ (σ of each X-, Y-, Z- axis is about 3 cm [73]). The event position reconstructed from this method is used to reject the events from following bad crystals:

- Crystal 11 is the most contaminated of ^{238}U and ^{232}Th [73];
- The housing module of crystal 57 is reported to have the contaminated air [73];
- Crystal 54 is reported to have the largest quenching factor, which makes the α-peak of ^{215}Po to be isolated, so that it is difficult to estimate the background events in this crystal [73].

Thus, in this research, to reduce the effect of α-events, events from all crystals (except crystal 11, crystal 54, and crystal 57) with 2σ precision are accepted.

Conditions for energy reconstruction

In summary, the β-events in this thesis are selected using the following cut conditions:

- Data Quality is used to remove saturated, overshoot, start channel error events;
- Charge Ratio ranging from 0.14 to 0.17 is used to select β-like events;
- Dual-Gate Trigger condition, stored in Master Module's registers, is used to select CaF_2 events;
- Crystal selection is used to select the events from all crystals within 2σ precision, but not crystal 11, crystal 54, and crystal 57.

For every event, the above conditions are used to select the β-like events of CaF_2 crystals to construct the energy histogram.

Chapter 6

Photon Counting Analysis

In this chapter, the photon counting method as a solution for the baseline fluctuation is described. The data with fine sampling, mentioned in chapter 5, is used for analysis. The single photoelectron signals can overlap each other in CaF_2 waveform. Due to signal overlapping, there are many photoelectrons lost in photon counting. The loss of photoelectrons makes the energy resolution worse. Thus, partial photon counting is introduced to reduce baseline fluctuation and avoid the loss of photoelectrons. With this alternative method, it results in the improvement of energy resolution. The ^{40}K and ^{208}Tl peaks are used to evaluate the improvement of energy resolution with partial photon counting.

6.1 Threshold for Photon Counting Analysis in CANDLES

The summed waveform of CaF_2 signal is formed by many photoelectrons, which are generated in 62 PMTs, and the waveform of each PMT contains less amount of photoelectrons (Figure 6.9). The overlap of single photoelectrons causes the inefficiency in photon counting. If there are many photoelectrons, the overlap probability is increased. For instance, at the γ-peak of ^{40}K, there are about 1330 p.e. obtained in 62 PMTs, and there are about 21 p.e. in each PMT. In the spectrum of natural background of CANDLES, the γ-peak of ^{40}K (1460 keV) is most dominant. The decay constant of CaF_2 is about 1000 nsec. The photoelectron rate in the summed waveform of 62 PMTs is about $1330/1000 \approx 1.3$ p.e./nsec. The average photoelectron rate of one PMT is about 0.02 p.e./nsec. As the rate of photoelectron in each PMT is small, the overlap of photoelectron signals in each PMT is reduced.

For photon counting, a threshold is set for each PMT, and the photoelec-

trons are counted if they cross the threshold. The signal at every timebin is counted as 1p.e. if it crosses the threshold. The number of photoelectrons is proportional to the obtained energy. Since there is no need to integrate, the baseline fluctuation is avoided. The threshold is determined by using the peak of the single photoelectron signal of each PMT. In this section, determination of the threshold for photon counting is indicated, and the discrimination of 1p.e. from 0p.e. using the threshold is discussed.

6.1.1 Threshold for photon counting

The 1p.e. waveform of one PMT is different one by one (Figure D.4). Therefore, the threshold for photon counting is set individually for each PMT. Figure 6.1 shows the pulse height distribution of 1p.e. signal of PMT01 using LED data taken in the previous research [93]. The threshold for photon counting is set as:

$$\text{Threshold} = \text{Pedestal} - (\mu_{\text{peak}} - \text{n}\sigma_{\text{peak}}),$$

where μ_{peak} and σ_{peak} are the mean and deviation of this distribution, respectively. Different thresholds are applied to the experimental data to evaluate the performance in the separation of 1p.e. signals from the baseline. The green-solid line in Figure 6.2 shows the distribution of signal integration

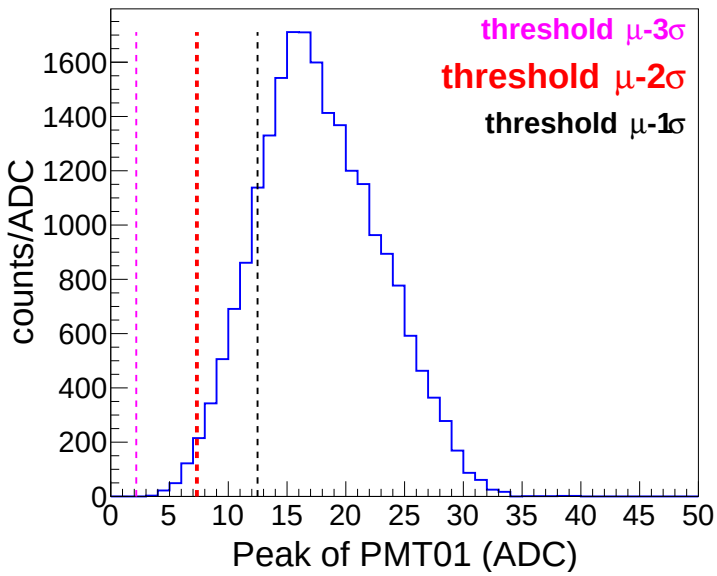

Figure 6.1: Distribution of the peak of 1p.e. signal of PMT01. The threshold for photon counting is set at $\mu - 2\sigma$, where μ and σ are respectively, the mean and deviation of peak distribution.

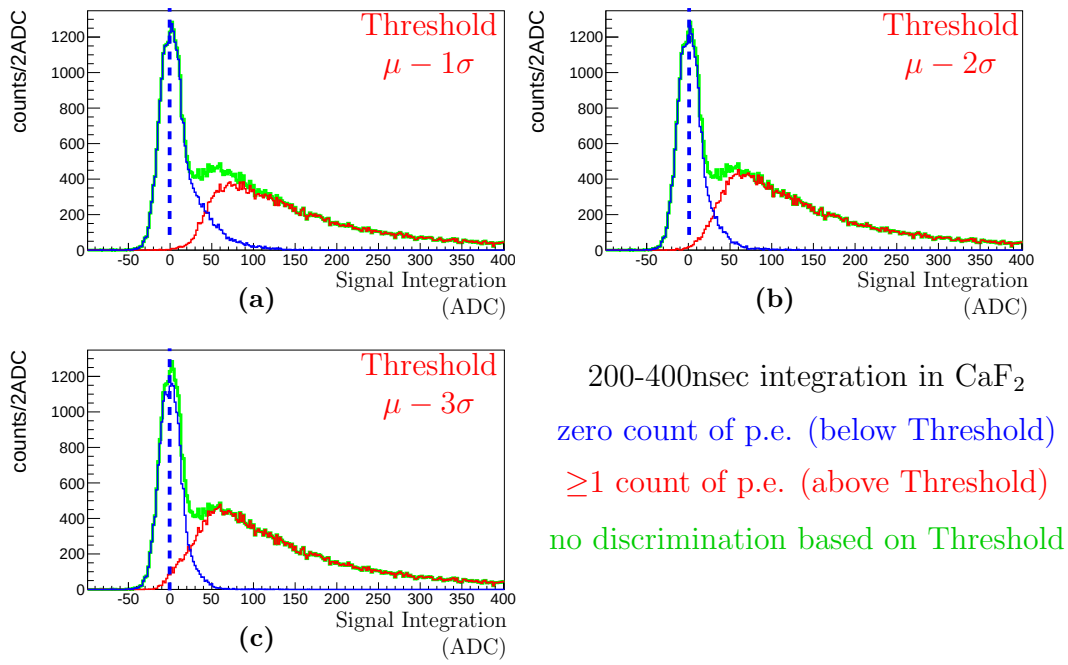

Figure 6.2: Distribution of signal integration (from 200-400 nsec) in PMT01 (green-solid line). Different thresholds are applied to discriminate the 0p.e. signals (blue-solid line) and 1p.e. signals (red-solid line).

between 200-400 nsec of PMT01 using CaF_2 events. Three thresholds of $(\mu_{\text{peak}} - 1\sigma_{\text{peak}})$, $(\mu_{\text{peak}} - 2\sigma_{\text{peak}})$ and $(\mu_{\text{peak}} - 3\sigma_{\text{peak}})$ are tested. Using the thresholds, the 1p.e. signals within 200-400 nsec are identified. If there is no count of photoelectron, the signal integration is equivalent to the integration of 0p.e. If the number of counted photoelectrons is more than or equal to one, the signal integration is the integration of 1p.e. and multi p.e. The separation performance can be checked by comparing the histograms of 0p.e. and 1p.e signals with different thresholds for photon counting:

- For the threshold of $(\mu_{\text{peak}} - 1\sigma_{\text{peak}})$: Because the threshold is high, some photoelectron signals are not counted as 0p.e. signals. The right tail of 0p.e. histogram overlay on the 1p.e. histogram.
- For the threshold of $(\mu_{\text{peak}} - 3\sigma_{\text{peak}})$: Because the threshold is low, noises in the baseline are counted as 1p.e. signals. The left tail of 1p.e. histogram overlay on the 0p.e. histogram.
- For the threshold of $(\mu_{\text{peak}} - 2\sigma_{\text{peak}})$: The threshold is enough to distinguish the 1p.e. signals from the noises in the baseline. It results in the best separation of 0p.e. and 1p.e.

In this research, the threshold of $(\mu_{\text{peak}} - 2\sigma_{\text{peak}})$ is chosen as the threshold for photon counting analysis.

6.1.2 Charge of single photoelectron obtained by photon counting

The photoelectrons can be distinguished from the baseline using the above threshold. The charge of single photoelectron is useful information to evaluate the performance of identification of 1p.e. To get the charge information of every 1p.e. signal, we need to identify the 1p.e. signals and determine the time window to get the 1p.e. signal integration. An upper threshold (UD) is used to identify the 1p.e. signals. As discussed in previous section, for every event, the upper threshold is set as Pedestal $-$ $(\mu_{\text{peak}} + 2\sigma_{\text{peak}})$ is set individually for every PMT. To determine the left and right bins for 1p.e. signal integration, a lower threshold (LD) is set as Pedestal $-$ 0.5ADC. Figure 6.3 shows an example of 1p.e. signal with the upper threshold (red-dashed line) for identification of 1p.e. signals and the upper threshold (green-dashed line) to determine the window for 1p.e. signal integration.

The charge of signal counted as 1p.e. is studied for every PMT. The charge distributions of 1p.e. in CaF_2 signal and dark current events in PMT01 are compared (Figure 6.4). Since the CaF_2 waveform has many photoelectrons, the charge distribution of single photoelectron in CaF_2 waveform has the contribution from the charge of multi photoelectron signals. On the

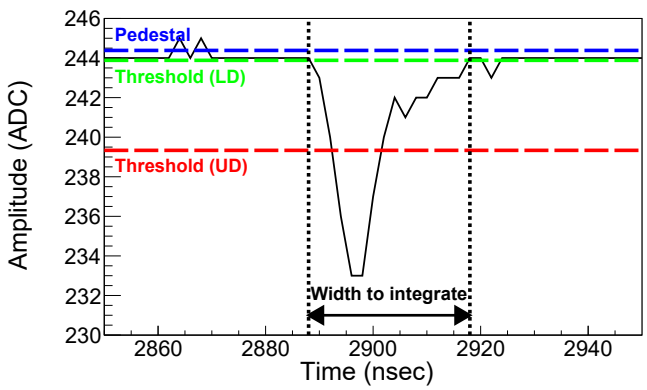

Figure 6.3: The waveform of 1p.e. signal (black-solid line). Threshold Upper Limit (red-dashed line) = Pedestal$-(\mu_{\text{peak}} - 2\sigma_{\text{peak}})$ is set to count the photoelectrons. Threshold Lower Limit (green-dashed line) = Pedestal$-$0.5ADC is set to determine the left and right bins for integrating 1p.e. signal.

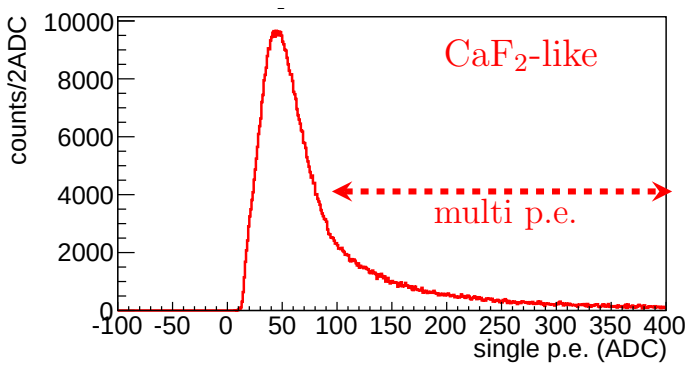

(a) CaF_2-like events

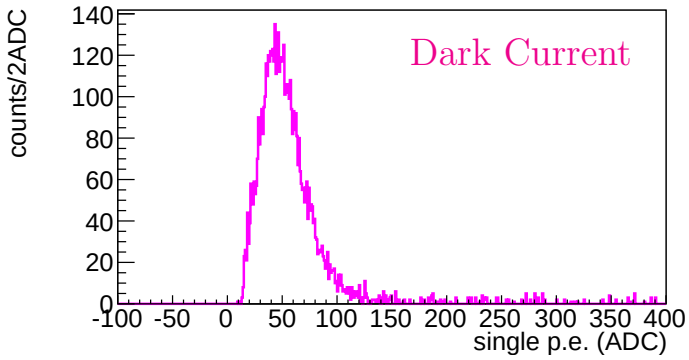

(b) Dark Current events

Figure 6.4: Charge distributions of photoelectron signals in CaF_2 waveform (a) and dark current (b) in PMT01. The charge distribution of photoelectron signals in the CaF_2 waveform has the contribution of single and multi photoelectron signals. Due to the low rate of dark current, the charge of multi photoelectrons signals is rarely obtained.

other hand, as the low rate of dark current, the occurrence of multi photoelectron signals in dark current is rare, and the charge distribution obtained is mainly from 1p.e. By analyzing 62 PMTs, the applied threshold are proved to be good enough for photon counting purpose.

6.2 Overlap of single photoelectron signals in Photon Counting

The multi photoelectron signal forms the overlap of single photoelectron signals. It causes the loss of counts during photon counting. With more photoelectrons obtained, the overlap probability increases. The overlap of

two 1p.e. signals depends on their time interval. If their time interval is too short, it is impossible to separate these two signals, and these two signals are detected as a single photoelectron. SIGNAL INTERVAL is used to name the minimum time interval for distinguishing these two 1p.e. signals in photon counting. The SIGNAL INTERVAL depends on the threshold set for photon counting and the width of 1p.e. signal. With the smaller value of SIGNAL INTERVAL, the overlapping probability and the loss of photoelectrons are reduced. The inefficiency of photon counting can be seen with the 2-dimensional distribution of counted photoelectrons and true photoelectrons. Figure 6.5 shows those distributions of PMT07 and PMT21. For PMT07 (13-inch PMT), due to signal overlapping, the number of counted photoelectrons is saturated as many photoelectrons obtained in the PMT. The overlap in PMT07 is similar to the overlap in other 13-inch and 20-inch PMTs. The widths of 1p.e. signals of 13-inch and 20-inch PMTs are much wider than the widths of 1p.e. signals of 10-inch PMTs. For PMT21 (10-inch PMT), the correlation of counted photoelectrons and true photoelectrons tends to be linear due to the narrow width of 1p.e. signal. For 10-inch PMTs, there is reflection of 1p.e. signal with low amplitude (Figure D.4). In a multi photoelectron signal, the reflection is amplified, and it may be counted as a 1p.e. signal. At Q-value, the number of photoelectrons in each PMT is about

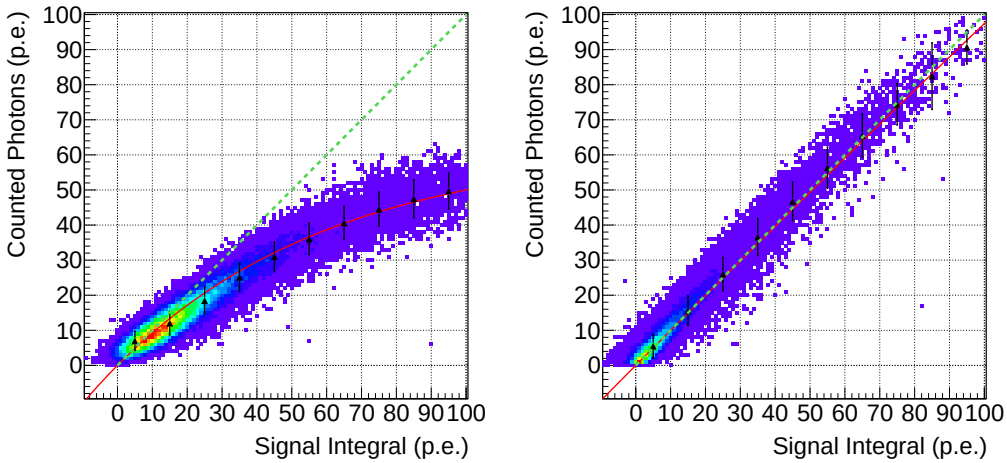

(a) PMT07 (13-inch) **(b)** PMT21 (10-inch)

Figure 6.5: Signal overlapping in photon counting is checked using the correlation of counted photoelectrons and signal integration in PMT07 (a) and PMT21 (b). The green-dashed line is the expected linear correlation, and the red-solid is the estimated correlation due to 1p.e. overlapping.

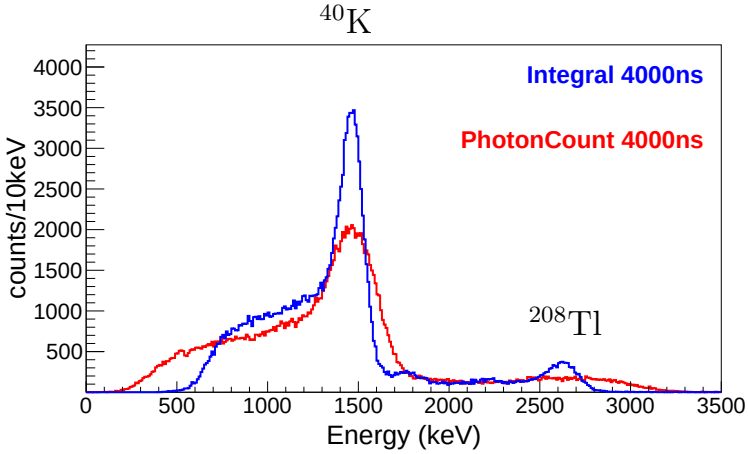

Figure 6.6: Energy histograms of full signal integration (blue) and full photon counting (red). The photon counting histogram has a terrible energy resolution due to the less number of photoelectrons. The number of photoelectrons is reduced because of signal overlapping in photon counting.

62 p.e. Using the estimation of counting efficiency (red-solid lines in Figure 6.5), and we can estimate the inefficiency of photon counting using 62 PMTs is 30 % at Q-value. Therefore, the overlap can result in many photoelectrons lost at Q-value. The discussion of overlap of 1p.e. signals in photon counting is mentioned in appendix F.

The loss of photoelectrons due to overlap of 1p.e. signals is found in all 62 PMTs. The loss of photoelectrons reduces the statistical resolution, and it makes the worse energy resolution. The energy histogram created by photon counting is compared to the histogram created by signal integration in Figure 6.6. The photon counting histogram has much worse energy resolution compared to the one of the signal integration histogram. In the photon counting histogram, the ^{40}K γ-peak (1460 keV) is broader, and the ^{208}Tl γ-peak (2614 keV) is not visible. The photon counting is a solution for baseline fluctuation; however, it results in a worse energy resolution due to the overlap of 1p.e. signals.

6.3 Partial Photon Counting

In general, there are two ways for calculating the obtained energy in scintillator: signal integration is used in short decay constant scintillator (e.g., $\tau_{\mathrm{NaI(pure)}}$ = 60 nsec [97]) with negligible effect of baseline fluctuation; and photon counting is used in long decay constant scintillator (e.g. $\tau_{\mathrm{CaWO_4}}$ = 8000 nsec [97]) to avoid the baseline fluctuation. The decay constant of $\mathrm{CaF_2}$

($\tau_{CaF_2} = 1$ μsec) is something in between. The 4 μsec signal integration used in CANDLES to calculate the energy of CaF_2 signal leads to the accumulated baseline fluctuation (as discussed in chapter 4). Therefore, photon counting is considered as a method to reduce the baseline fluctuation. However, as discussed in section 6.2, photon counting in CaF_2 signals results in the overlap of 1p.e. signals and the loss of photoelectrons. Consequently, the resolution of the photon counting energy spectrum is worse than the spectrum obtained by signal integration. Therefore, an alternative method needs to be studied for the reduction of baseline fluctuation and avoiding the loss of photoelectrons.

6.3.1 Distribution of photoelectron charge by timebin

The multi photoelectron signals, which are formed by many single photoelectron signals, are the demerit for photon counting. In section 6.2, it is probed that the overlap probability in CaF_2 depends on the number of obtained photoelectrons and the signal interval of a PMT. In this section, the rate of multi photoelectron signals depending on the timebin in the recorded waveform is discussed since it is a useful approach to the partial photon counting method introduced in section 6.3.2.

The charge distribution of single photoelectron by timebin of CaF_2 events and dark current in PMT01 are plotted respectively in Figure 6.7. In the case of dark current, most of the events obtained are single photoelectron signals distributed uniformly in all timebin. The projection on the horizontal axis of the dark current histogram is analyzed in section 4.1 to estimate the dark current rate. On the other hand, due to the exponential-decay shape of the CaF_2 waveform, many multi photoelectrons are found near the rising edge of the CaF_2 signal. The probability of finding these multi photoelectron signals is decreased near the tail of the waveform. The charge distributions at the head (signal integration of 800-1200 nsec) and the tail (signal integration of 3600-4000 nsec) of the waveform are plotted in blue color in Figure 6.8 to compare with the charge distribution of dark current plotted in magenta color. Comparing distributions of 1p.e. charge at the head and tail of the waveform, it is clear that the overlap of single photoelectrons is much reduced at the signals near the tail of the waveform. Therefore, in opposition to the head of the waveform, the photon counting can perform well at the tail part of the waveform. The partial photon counting is introduced in section 6.3.2 making use of this characteristic.

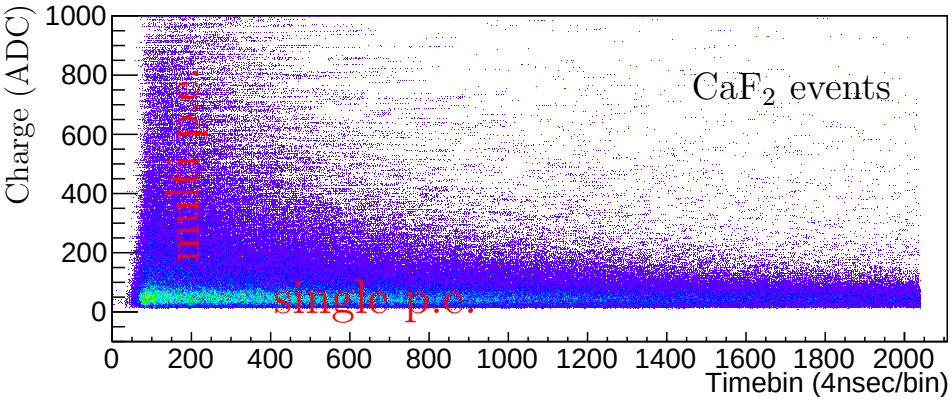

(a) CaF_2 events

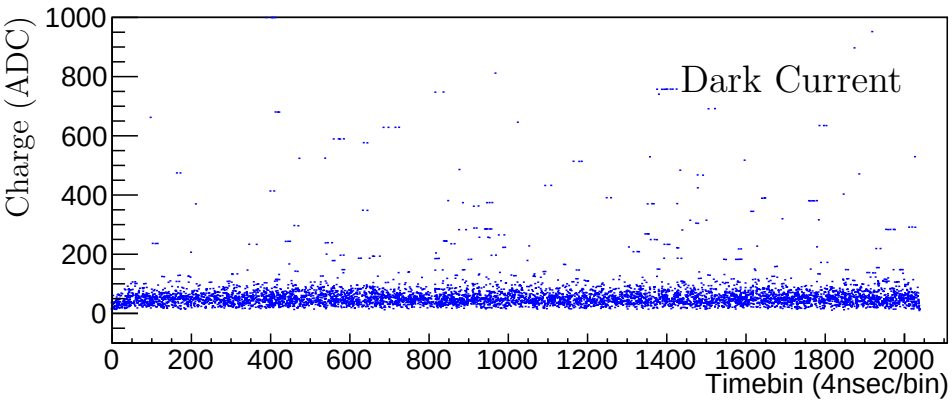

(b) Dark Current

Figure 6.7: Charge of photoelectron signals distributed by the timebin in CaF_2 (a) and Dark Current (b) events. The multi photoelectrons are found near the start (or the rising edge) of the CaF_2 waveform.

6.3.2 Partial Photon Counting

A. Introduction of partial photon counting

Photon counting is not useful at the rising edge of CaF_2 waveform as the multi photoelectron signals dominate in this region, but it can perform at the tail of the waveform with low overlap probability of single photoelectrons. The partial photon counting is introduced using the dependence of overlap probability on the timebin. Figure 6.9 shows the idea of the partial photon counting method. In partial photon counting, for every PMT, the waveform in 4000 nsec is divided into two areas:

- The head part (near the rising edge of the waveform) contains many

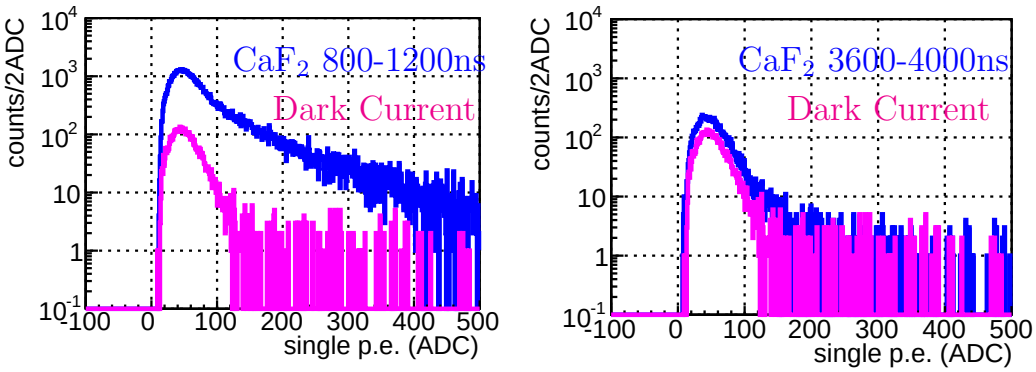

(a) Distribution from 800-1200 nsec **(b)** Distribution from 3600-4000 nsec

Figure 6.8: Charge distribution of photoelectron signals of CaF_2 signals plotted in blue-solid line at timebin of 800-1200 nsec (a) and 3600-4000 nsec (b). The distribution of dark current signals is plotted in magenta color for comparison. The single photoelectrons are mainly detected near the tail of the CaF_2 waveform.

multi photoelectron signals. Signal integration is carried out for this area to calculate the obtained photoelectrons to avoid the loss of photoelectrons.

- The tail part (near the tail of the waveform) contains less multi photoelectron signals. The photon counting is performed to count the obtained photoelectrons to avoid the baseline fluctuation.

The intervals for signal integration and photon counting are, respectively, T_{INT} and T_{COUNT}, and the sum of T_{INT} and T_{COUNT} is fixed at 4000 nsec. The energy of the waveform is equivalent to the total photoelectrons obtained in the head and tail parts.

B. Calibration of histograms built with partial photon counting

The energy spectrum from the natural background is obtained in Photon Counting measurement. In this thesis, different mixtures of T_{INT} and T_{COUNT} are applied to construct the energy histograms in order to find the mixtures providing the best energy resolutions at ^{40}K and ^{208}Tl peaks. Figure 6.10-(a) shows the obtained histograms of the number of photoelectrons using partial photon counting method with cut conditions mentioned in chapter 5. In the partial photon counting method, the number of photoelectrons is still lost, depending on the interval of photon counting. To expand the interval of

photon counting results in the decrement of the number of photoelectrons. For checking this decrement, the graphs of the number of photoelectrons observed at ^{40}K and 208Tl peaks as a function of T_{INT}, which is ranging from 500 to 4000 nsec, are plotted in Figure 6.10-(b). For further analysis, these histograms are calibrated using the referred values of two energy peaks ^{40}K (1460.822 keV [98]) and ^{208}Tl (2614.511 keV [98]). Some energy histograms after calibration are plotted in Figure 6.11-(a), and the number of photoelectrons after calibration is plotted as a function of integration interval in Figure 6.11-(b).

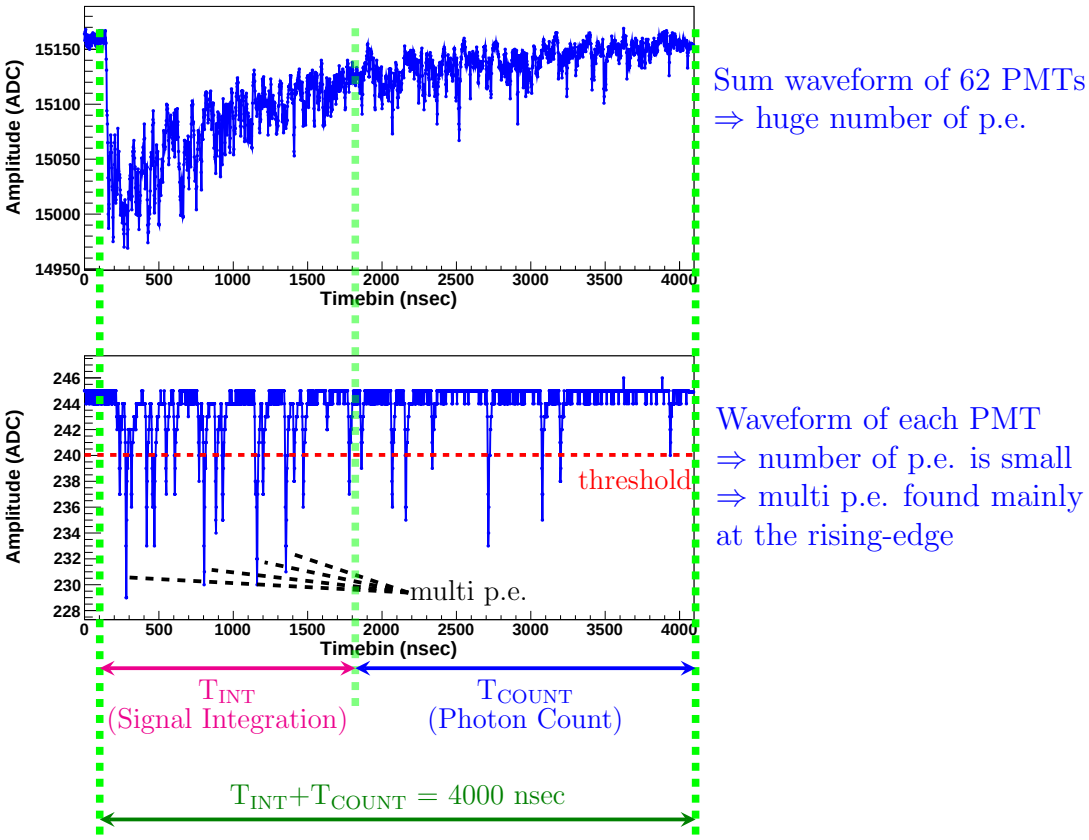

Figure 6.9: Sum waveform of 62 PMTs (top) and waveform of one PMT (bottom). The sum waveform contains many photoelectrons, but there are not so many photoelectrons in one PMT. In partial photon counting, the 4000 nsec waveform of every PMT is divided into two areas: the head one for signal integration, and the tail one for photon counting.

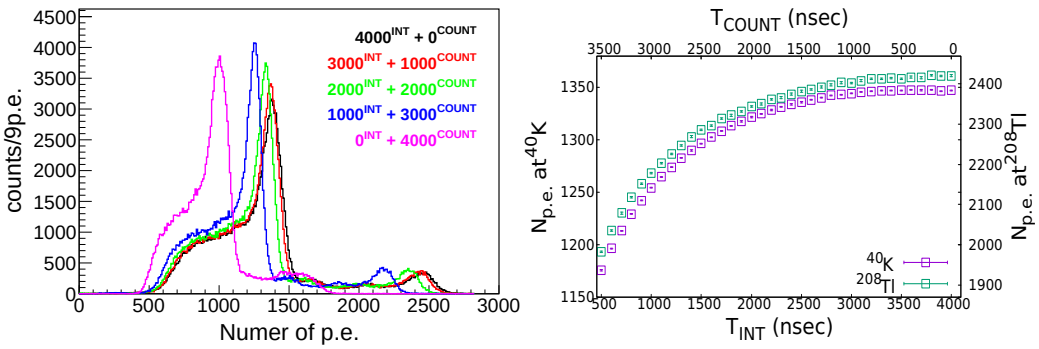

(a) Energy histograms before calibration **(b)** Peak positions before calibration

Figure 6.10: Histograms of the number of photoelectrons built with partial photon counting method before calibration. Different mixtures of T_{INT} and T_{COUNT} are marked with different colors. The number of photoelectrons is decreased when the photon counting interval is increased.

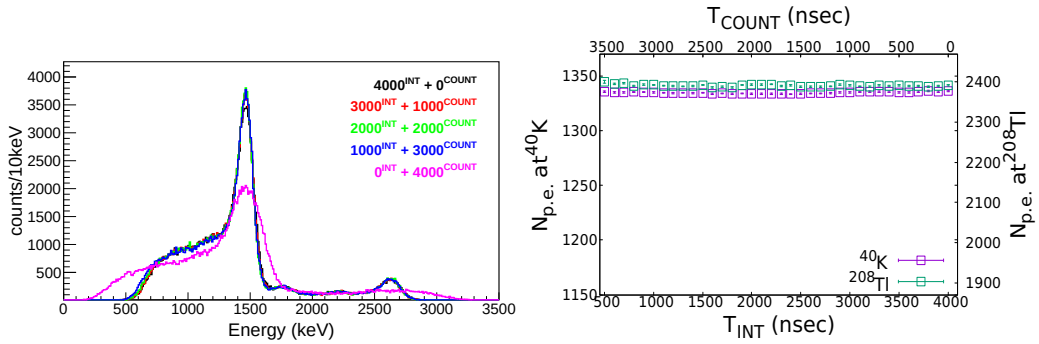

(a) Energy histograms after calibration **(b)** Peak positions after calibration

Figure 6.11: Energy histograms built with partial photon counting method after calibration.

C. Energy resolution with partial photon counting

In partial photon counting, expanding the T_{INT} (T_{COUNT}) results in the improvement of statistical resolution (reduction of baseline fluctuation). In other words, expanding interval of photon counting or not is a "trade-off" of statistical resolution and baseline fluctuation. Thus, different results of energy resolution are obtained with a different combination of photon counting and signal integration intervals. With every energy histograms obtained from partial photon counting, a fitting function is applied to extract the energy resolutions of ^{40}K and ^{208}Tl peaks. This fitting function studied in previous

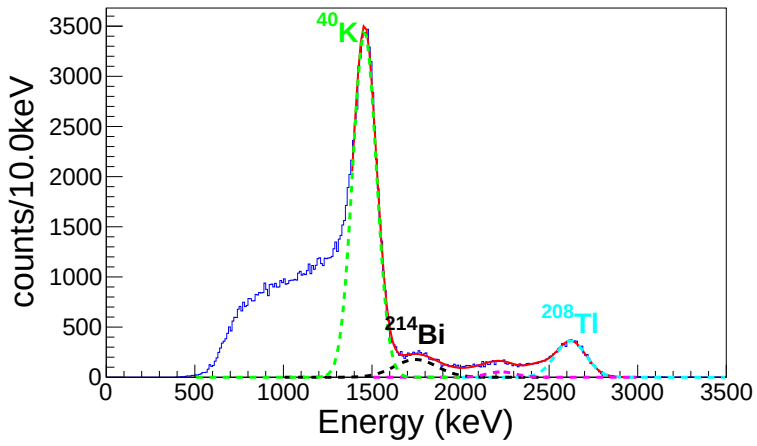

Figure 6.12: Fitting function (red-solid line) applied on every energy spectrum obtained by partial photon counting method to extract the energy resolutions of ^{40}K and ^{208}Tl peaks. The Gaussian peaks of ^{208}Tl, ^{214}Bi and ^{40}K are plotted in green, black and cyan dashed lines.

researches [74, 75] includes following functions:

- Gaussian of ^{208}Tl gamma peak at 2.6 keV,
- Gaussian of ^{214}Bi gamma peak at 1.76 MeV,
- Gaussian of ^{40}K gamma peak at 1.46 MeV,
- Error function to interpret the Compton background from ^{208}Tl (and other unknown events forming the baseline in the energy spectra).

Figure 6.12 shows the obtained energy histogram with the fitting function plotted with the red-solid line. The Gaussian peaks of ^{208}Tl, ^{214}Bi and ^{40}K are plotted in green, black and cyan dashed lines. In this section, the partial photon counting is applied to the raw data with different mixtures of photon counting and signal integration intervals, and the integration interval is ranging from 4000 nsec down to 600 nsec.

The energy resolutions (σ_{E}) at ^{40}K and ^{208}Tl peaks obtained by fitting are respectively plotted with blue circles and red squares in Figure 6.13. The results at ^{214}Bi γ-peak are not discussed due to their low statistics. At each energy peak, the errors of different mixtures of signal integration and photon counting are correlated. The error bars of ^{40}K and ^{208}Tl peaks are plotted with blue and red lines, respectively, in Figure 6.13. When the integration interval is increased, the baseline fluctuation is reduced; hence, the energy resolution is improved. Near the rising edge, the probability of

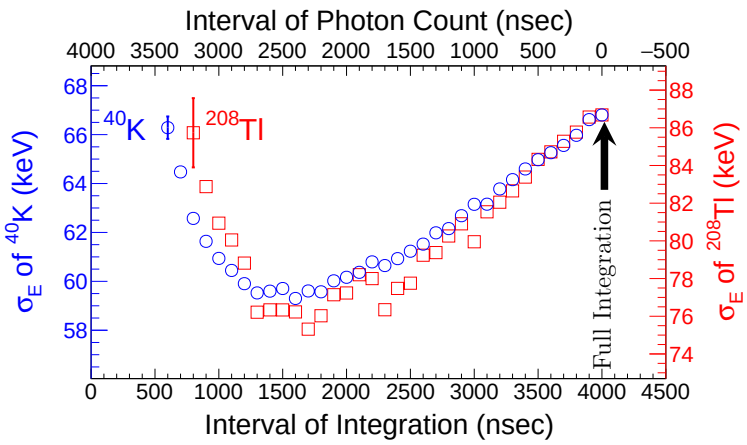

Figure 6.13: Obtained energy resolution at ^{40}K (blue circles) and ^{208}Tl (red squares) peaks as a function of integration interval.

signal overlapping is much higher than the tail part. Therefore, the resolution is rapidly increased near the rising edge. Comparing the graphs, the rising-up slope at the short integration interval of ^{208}Tl peak is steeper than the one of ^{40}K due to the more severe overlap probability at ^{208}Tl. From fitting results, we obtain the improved resolution:

- At ^{40}K peak, the deviation is improved from 66.8 keV to 59.3 keV (σ_{E}/E is improved from 4.5 % down to 4.0 %) when reducing the integral gate from 4000 nsec down to 1600 nsec.
- At ^{208}Tl peak, the deviation is improved from 86.7 keV to 75.3 keV (σ_{E}/E is improved from 3.3 % down to 2.9 %) when reducing the integral gate from 4000 nsec down to 1700 nsec.

With the improvement of energy resolution, it is expected to improve the energy resolution at the Q-value of ^{48}Ca with the same method. Consequently, the sensitivity of the CANDLES detector is enhanced in search of neutrino-less double beta decay from ^{48}Ca. The optimized integration interval to obtain the best energy resolution depends on the energy. The energy resolution of each energy peak consists of different components (as discussed in chapter 7). By studying those components, one can estimate the optimized integration interval for each energy peak.

Chapter 7

Result and Discussion

Since the baseline fluctuation studied in chapter 4 affects the energy resolution severely, the partial photon counting method mentioned in chapter 6 is introduced to reduce this fluctuation. In this chapter, the obtained energy resolution and baseline fluctuation are compared to each other and remaining fluctuation affecting the resolution is estimated. From the study of baseline fluctuation, a fitting function of energy resolution is derived, and the energy resolution at Q-value of ^{48}Ca is estimated to be improved. With the estimated energy resolution, the improvement of the $0\nu\beta\beta$ half-life limit is discussed in this chapter.

7.1 Discussion about Energy Resolution

7.1.1 Fluctuations affecting the energy resolution

As mentioned in chapter 6, the energy resolutions at ^{40}K and ^{208}Tl peaks are improved when reducing the integration intervals. In this section, these improvements are probed to be strongly related to the baseline fluctuation studied in chapter 4. Figure 7.1-(a) and (b) indicate the energy resolution at ^{40}K and ^{208}Tl peaks. Figure 7.1-(c) and (d) shows the fluctuations affecting energy resolution in CANDLES experiment as functions of integration intervals. The fluctuations consist of:

- The statistical fluctuation (σ_{Stat}) are plotted with black solid line. Reducing the integration interval (or increasing the photon counting interval), there are more photoelectrons overlapping each other. With more overlap of photoelectrons, the statistical fluctuation becomes worse because there are photoelectrons lost in counting. The loss of photoelectrons in counting is statistical. The statistical fluctuation is estimated

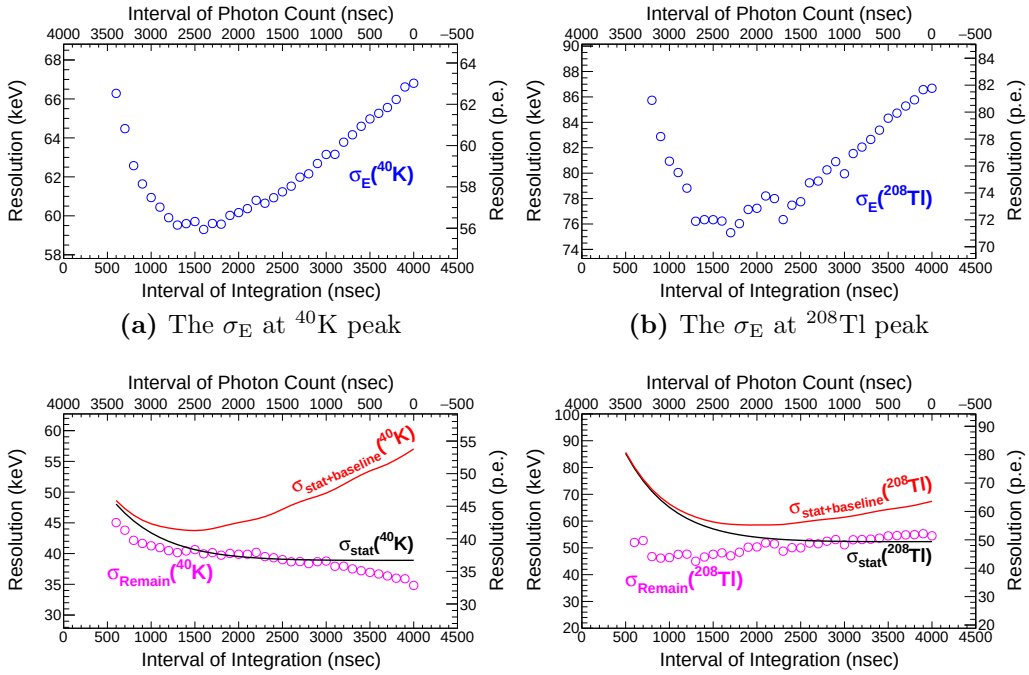

(a) The σ_{E} at ^{40}K peak

(b) The σ_{E} at ^{208}Tl peak

(c) The statistical, statistical+baseline and remaining fluctuations at ^{40}K peak

(d) The statistical, statistical+baseline and remaining fluctuations at ^{208}Tl peak

Figure 7.1: The energy resolutions, statistical, statistical+baseline, and remaining fluctuations are plotted as a function of the integration interval.

accounting the overlap of photoelectrons in photon counting by a simple mathematical model (appendix F).

- The root sum square of statistical fluctuation and baseline fluctuation ($\sqrt{\sigma_{\mathrm{Stat}}^2 + \sigma_{\mathrm{Base}}^2}$) are plotted with red line.
- The remaining fluctuation (σ_{Remain}) are plotted with magenta circles. The remaining fluctuation is calculated as $\sqrt{\sigma_{\mathrm{E}}^2 - \sigma_{\mathrm{Stat}}^2 - \sigma_{\mathrm{Base}}^2}$.

The baseline fluctuation is the sum square root of the accumulated pedestal uncertainty mentioned in section 4.4 and the digitization error mentioned in section 4.2. Since the dark current cannot be reduced by partial photon counting and its effect is too small, it is not considered in this calculation. The remaining fluctuation is almost not changed at ^{208}Tl peak from 4000 nsec down to 600 nsec integration. At the ^{40}K peak, the average remaining fluctuation is about 40 keV. The remaining fluctuation is quite different from the average remaining fluctuation at $\mathrm{T_{INT}} > 3000$ nsec or $\mathrm{T_{INT}} < 1500$ nsec. Because the overlap of photoelectrons in photon counting is estimated with a

Table 7.1: The energy resolution (σ_{E}) and the contributing fluctuations (statistical, baseline and remaining fluctuations) at ^{40}K and ^{208}Tl peaks.

	^{40}K peak 1460.511 keV	**^{208}Tl peak 2614.822 keV**
Energy Resolution ($\sigma_{\mathbf{E}}$)	66.8 ± 0.4 keV	86.7 ± 2.0 keV
Statistical Fluctuation ($\sigma_{\mathbf{p.e.}} = \sqrt{\mathbf{N_{p.e.}}}$)	38.9 ± 0.1 keV	52.3 ± 0.1 keV
Baseline Fluctuation ($\sigma_{\mathbf{Base}} = \sqrt{\sigma^2_{\mathbf{PedErr}} + \sigma^2_{\mathbf{DE}}}$)	41.7 ± 1.3 keV	42.5 ± 1.3 keV
Remaining fluctuation ($\sqrt{\sigma^2_{\mathbf{E}} - \sigma^2_{\mathbf{Stat}} - \sigma^2_{\mathbf{Base}}}$)	34.8 ± 1.8 keV	54.5 ± 3.3 keV

simple mathematical model, the statistical fluctuation may be estimated not perfectly. It leads to the reduction or increment of remaining fluctuation. In general, the remaining fluctuation is almost independent to the integration interval.

The energy resolution, statistical fluctuation, baseline fluctuation, and the remaining fluctuation of ^{40}K and ^{208}Tl peaks with an integration interval of 4000 nsec are indicated in Table 7.1. At ^{40}K peak, the baseline fluctuation contributes the most effect on the energy resolution, and the remaining fluctuation contributes the least ($\sigma_{\mathrm{Base}} > \sigma_{\mathrm{Stat}} > \sigma_{\mathrm{Remain}}$). At the ^{208}Tl peak, the baseline fluctuation has the least contribution, while the remaining and statistical fluctuations have the most contribution to the energy resolution ($\sigma_{\mathrm{Remain}} \approx \sigma_{\mathrm{Stat}} > \sigma_{\mathrm{Base}}$).

7.1.2 Discussion about the remaining fluctuation

The remaining fluctuation is assumed to be independent with the integration interval, and the source of this remaining fluctuation is unknown. If the remaining fluctuation depends on the energy, the effect of this remaining fluctuation may be more severe at the Q-value of ^{48}Ca compared to the effect at ^{40}K peak and ^{208}Tl peak. Assuming the remaining fluctuation is zero with no incident photoelectrons, we can make the graphs of remaining fluctuations a function of energy. Figure 7.2 shows the remaining fluctuations at 0 keV, ^{40}K peak and ^{208}Tl peak. The data points at ^{40}K and ^{208}Tl peaks show the average value of remaining fluctuations, in the integration interval from 600 nsec to 4000 nsec, with the standard deviations. The remaining fluctuations are quite close to the statistical fluctuations at ^{40}K and ^{208}Tl peaks. Assum-

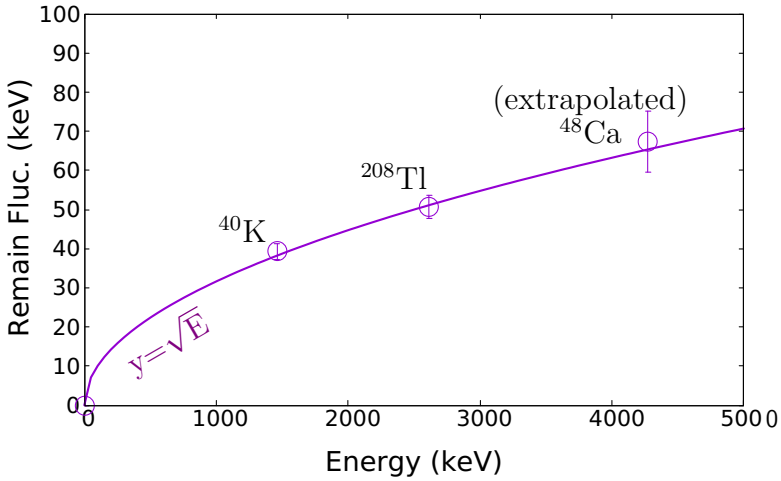

Figure 7.2: The remaining fluctuation as a function of energy. The circles are the remaining fluctuations at γ-peaks of ^{40}K, ^{208}Tl and at the Q-value of ^{48}Ca. The remaining fluctuation at Q-value is estimated assuming Remain(E) = a$\times\sqrt{\mathrm{E}}$. The solid line is the statistical fluctuation function (y=$\sqrt{\mathrm{E}}$).

ing the remaining fluctuation is zero at 0 keV, using the function Remain(E) = a$\times\sqrt{\mathrm{E}}$ is not so bad to cover remaining fluctuations at 3 data points (0 keV, ^{40}K peak and ^{208}Tl peak). Thus, the remaining fluctuation at Q-value of ^{48}Ca is extrapolated with this function. From estimation, the remaining fluctuation at Q-value of ^{48}Ca is about 60 keV to 70 keV.

7.2 Improvement of energy resolution and $0\nu\beta\beta$ half-life limit

7.2.1 Energy resolution at Q-value of ^{48}Ca

As the energy resolutions at ^{40}K and ^{208}Tl peaks are improved, the improvement of energy resolution at Q-value of ^{48}Ca is expected. In summary, four fluctuations studied in this thesis are affecting the energy resolution:

- Statistical fluctuation (σ_{Stat}) is proportional to $\sqrt{\mathrm{E}}$;
- Digitization Error (σ_{DE}) is proportional to the statistical fluctuation of number of photoelectrons obtained in each PMT. The effect is probed to be no much when pedestal is adjusted to 244.5 ADC as it is shown

in Table 4.1. According to equation 4.3, it is roughly assumed to be proportional to $\sqrt{E}$;

- Accumulated pedestal uncertainty (σ_{PedErr}) is independent with the obtained number of photoelectrons;
- Remaining fluctuation (σ_{Remain}): is assumed to be proportional to the statistical fluctuation (as mentioned in section 7.1.2).

From the above factors, the energy resolution can be expressed as a function of energy as following:

$$\begin{aligned}\sigma_E &= \sqrt{\sigma^2_{\text{stat}} + \sigma^2_{\text{DE}} + \sigma^2_{\text{PedErr}} + \sigma^2_{\text{Remain}}} \\ &= \sqrt{a_0 E + a_1 E + c^2 + a_2 E}\end{aligned}$$

$$\Rightarrow \frac{\sigma_E}{E} = \sqrt{\frac{a_0 + a_1 + a_2}{E} + \frac{c^2}{E^2}}$$

The energy resolution equation can be described as:

$$\text{Resolution}(E) = \frac{\sigma_E}{E} = \sqrt{\frac{p0}{E^2} + \frac{p1}{E}} \tag{7.1}$$

The fitting function is applied to the obtained energy resolutions obtained in [74] to study the energy resolution of Run010 to justify its accuracy. Figure 7.3 shows the obtained energy resolutions plotted with black circles and the fitting function plotted as a red-dashed line. From the fitting, the energy resolution at Q-value is $2.4\times10^{-2} \pm 3.3\times10^{-6}$. This result is very close the value of $2.4\times10^{-2} \pm 0.2\times10^{-2}$, which is estimated in previous research [74].

As the equation 7.1 is probed to be good enough for fitting, the energy resolution at Q-value is extrapolated using the resolutions of ^{40}K and ^{208}Tl peaks obtained from partial photon counting method. Figure 7.4 shows the energy resolutions at Q-value as a function of integration interval. The green, red, and blue circles respectively indicate the resolutions obtained in Run009 [73], Run010 [74], and this thesis. As we can see, at the integration interval of 4000 nsec, there is an agreement in the energy resolution obtained in this thesis and the energy resolutions obtained in Run009 and Run010. As the integration interval reduced, the energy resolution is also improved due to the reduction of baseline fluctuation, and it rises up afterward. The best energy resolution estimated at the integration of interval of 1700 nsec is

$$\sigma_E^{\text{best}}(\text{Q-value}) = (2.171 \pm 0.003)\times10^{-2}$$

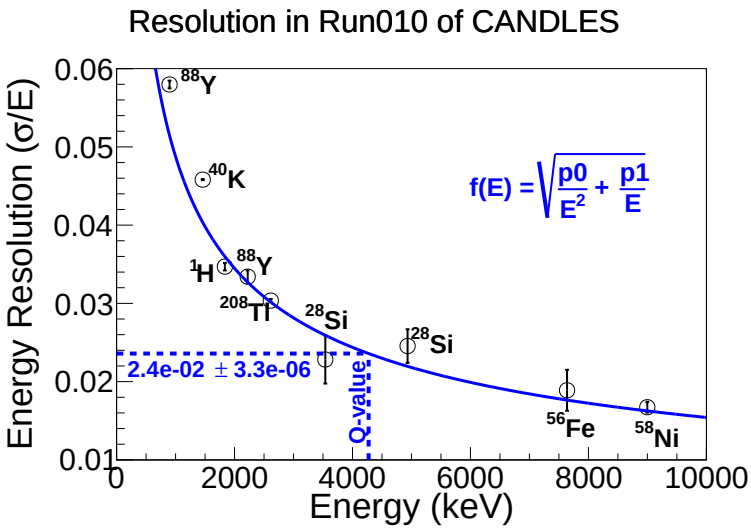

Figure 7.3: Apply the fitting function in equation 7.1 on the obtained resolutions in Run010 of CANDLES. The data points are referred from [74].

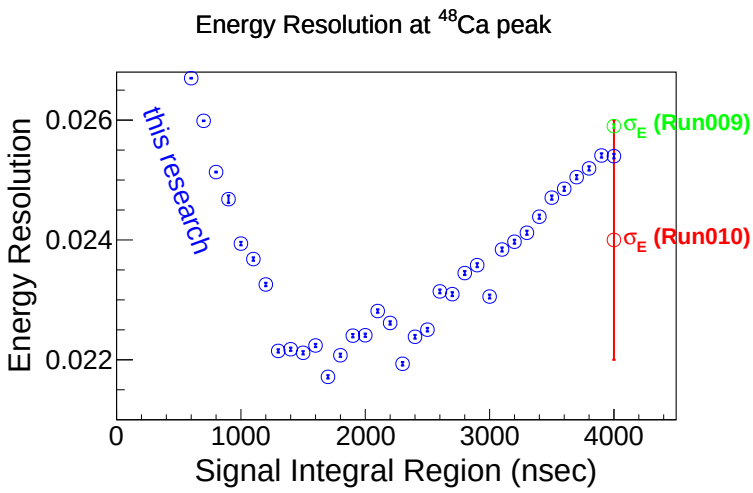

Figure 7.4: The estimated energy resolutions at Q-value using partial photon counting method. The values estimated using equation 7.1 and resolutions of ^{40}K and ^{208}Tl peaks are plotted with blue circles. The green and red circles indicate the energy resolutions obtained in Run009 and Run010, respectively.

7.2.2 Estimate the improvement of the $0\nu\beta\beta$ half-life limit of ^{48}Ca

The half-life limit of neutrino-less double beta decay can be expressed as a function of natural abundance, target mass, measurement time, background index and energy resolution:

$$\mathrm{T}_{1/2} = \ln(2)\mathrm{N_A}\frac{\varepsilon \cdot \mathrm{a}}{\mathrm{w}}\sqrt{\frac{\mathrm{M} \cdot \mathrm{T}}{\mathrm{b} \cdot \Delta\mathrm{E}}}$$

where $\mathrm{T}_{1/2}$: $0\nu\beta\beta$ half-life limit (year),

N_A: Avogadro number (=6.023×10^{23}),

ε: detection efficiency,

a: abundance of double beta decay isotope,

w: molecular mass,

M: total mass of target (kg),

T: measurement time (year),

b: background index (counts/keV/kg/year),

ΔE: energy resolution at Q-value (keV).

Table 7.2: Estimated the sensitivity of $0\nu\beta\beta$ half-life of ^{48}Ca after improvement of energy resolution from $\sigma_\mathrm{E}/\mathrm{Q}_{\beta\beta}$ of 2.6 % in Run009 to $\sigma_\mathrm{E}/\mathrm{Q}_{\beta\beta}$ of ∼2.2 % in this thesis.

	Sensitivity of $\mathbf{T}^{0\nu}_{1/2}(^{48}\mathbf{Ca})$ $\sigma_\mathrm{E}/\mathbf{Q}_{\beta\beta}$ = 2.6 %	**Sensitivity of $\mathbf{T}^{0\nu}_{1/2}(^{48}\mathbf{Ca})$ $\sigma_\mathrm{E}/\mathbf{Q}_{\beta\beta}$ = 2.2 %**
•M = 93 crystals, **•Live Time = 129.5 days,** **•No enrichment,** **(a=0.2 %)** **•Expected background** **= 27.3 - 30.0 counts**	0.44-0.50×10^{23} year (90 % C.L.) [73]	0.48-0.55×10^{23} year (90 % C.L.)

The improvement of ΔE can reduce the background in the region of interest (from 4170 keV to 4480 keV for the current CANDLES analysis) and improve the $0\nu\beta\beta$ half-life limit. The latest $0\nu\beta\beta$ half-life limit of ^{48}Ca of CANDLES is reported using data in Run009 in reference [73]. As the background of $2\nu\beta\beta$ is not dominant in the current CANDLES detector, if the energy resolution is improved to 2.2 %, the half-life limit is improved by:

$$\sqrt{\frac{\Delta\mathrm{E(Run009)}}{\Delta\mathrm{E(this\ thesis)}}} = \sqrt{\frac{2.6\% \times \mathrm{Q-value}}{2.2\% \times \mathrm{Q-value}}} \approx 1.09 \text{ times.}$$

With the improved energy resolution, the lower limit of $0\nu\beta\beta$ half-life of ^{48}Ca is estimated to be improved by about 1.09 times. In previous research [73], the sensitivity of the $0\nu\beta\beta$ half-life obtained by CANDLES is reported for the measurement with 93 CaF_2(pure) crystals, carried out in 129.5 days. With the improved energy resolution, this lower limits should be improved. Table 7.2 indicates the sensitivity of $0\nu\beta\beta$ half-life obtained in previous research [73] and the sensitivity estimated with the improved energy resolution in this thesis with the same measurement conditions. With the improvement of sensitivity, the partial photon counting method can be a useful tool to achieve a lower limit of $0\nu\beta\beta$ half-life of ^{48}Ca with current CANDLES detector.

Chapter 8

Conclusion

Neutrino-less double beta decay ($0\nu\beta\beta$) is a powerful tool to probe the Majorana nature of the neutrino, and it has not been obtained so far. This phenomenon indicates the violation of lepton number conservation. Hence, it requires new physics beyond the Standard Model. With the decay rate of $0\nu\beta\beta$, the effective neutrino mass can be determined. CANDLES detector is set up at 2700 m water equivalent underground at the Kamioka Underground observatory to detect the $0\nu\beta\beta$ from ^{48}Ca using 96 CaF_2(pure) scintillator crystals. Taking advantage of the highest Q-value (about 4.3 MeV) among all of double beta decay isotopes, it aims to achieve background-free measurement.

The two-neutrino double beta decay ($2\nu\beta\beta$) is an irreducible background, and we need to improve the energy resolution to reduce this background. In principle, the energy resolution should be equal to the statistical fluctuation of number of photoelectron ($\sigma_{\text{p.e.}} = 1.6$ % at Q-value). The energy resolutions at Q-value in Run009 and Run010 are 2.6 % [73] and 2.4 % [74], which are both more extensive than the statistical fluctuation, thus, there should be other fluctuation(s) affecting the energy resolution. As the CaF_2(pure) scintillator has a long decay constant of 1 μsec, the CaF_2 signal is integrated in 4000 nsec. Due to the long integration interval, the error of baseline measurement affects the energy resolution, and it consists of digitization error, dark current, and accumulated of pedestal uncertainty. In other experiments (such as KamLAND-Zen), the baseline fluctuation is not considered because of the short decay time of the scintillator. Among the baseline fluctuations, the error of baseline measurement is the most severe with the effect of about 40 p.e. at an integration interval of 4000 nsec. The partial photon counting method is introduced to calculate the obtained energy and reduce the baseline fluctuation. In this method, the signal is divided into two regions: the prompt part is for signal integration, and the latter part is for photon

counting. As a result, the energy resolutions at 2 γpeaks of ^{40}K (1460.822 keV) and ^{208}Tl (2614.511 keV) are improved:

- the resolution at ^{40}K peak is improved from 4.5 % down to 4.0 % when reducing the integral gate from 4000 nsec down to 1600 nsec, and
- the resolution At ^{208}Tl peak is improved from 3.3 % down to 2.9 % when reducing the integral gate from 4000 nsec down to 1700 nsec.

An unknown fluctuation is remained after subtracting the resolutions by all the fluctuations studied in this research. The unknown fluctuation having a severe effect on the energy resolution seems independent toon the integration interval. Thus, it is not reduced by partial photon counting.

The energy resolution at Q-value is extrapolated using the resolutions obtained at ^{40}K and ^{208}Tl peaks, and it is estimated to be improved from 2.5 % down to 2.2 %. Comparing the energy resolutions of Run009 and this thesis, it is expected to obtain the improved $0\nu\beta\beta$ half-life lower limit of ^{48}Ca by 1.09 times. With 93 CaF_2(pure) crystals and the same measuring conditions, the half-life limit is estimated to be:

$$\text{Run009 [73]} : T^{0\nu}_{1/2} > 0.44 - 0.50 \times 10^{23} \text{ year (90 \% C.L.)}$$
$$\Rightarrow \text{This thesis} : T^{0\nu}_{1/2} > 0.48 - 0.55 \times 10^{23} \text{ year (90 \% C.L.)}$$

With the improvement of sensitivity, the partial photon counting method can be a promising method to achieve a lower limit of $0\nu\beta\beta$ half-life with the current CANDLES detector.

Chapter 9

Future Prospect

Improving the energy resolution is essential to improve the sensitivity. CANDLES collaborators are planning to develop a detector with the bolometer technique, which provides excellent energy resolution. However, the technique has significant disadvantages, which are state-of-art refrigerator (operating temperature is nearly 0 K) and detector. It costs a lot of time and money on research and development. Another way to approach better energy resolution by using low-temperature CaF_2(pure) and photon counting is discussed in this chapter.

9.1 CaF_2(pure) scintillation properties at low temperature

The light yield and decay time of CaF_2(pure) scintillator crystal behave as functions of temperature [99]:

- The light yield is increased by four times with the temperature of less than 100 K (Figure 9.1-(a))
- The decay constant is extended from 1 μsec to 40 μsec with the temperature less than 30 K (Figure 9.1-(b)).

The increment of light yield leads to the increment of photoelectrons ($4\times3838 = 15352$ p.e.) results in the improvement of statistical fluctuation (from 1.6 % to 0.8 %). For cooling, we can use the cooling machine (such as CryoCoolers products of Cryomech company [100]) or liquefied gas. The liquefied gas with critical temperature less than 100 K are available on the market, such as LHe (5.19 K), LNe (44.4 K) or LH_2 (20 K) [101]. Because the decay constant is extended, using signal integration leads to a huge fluctuation

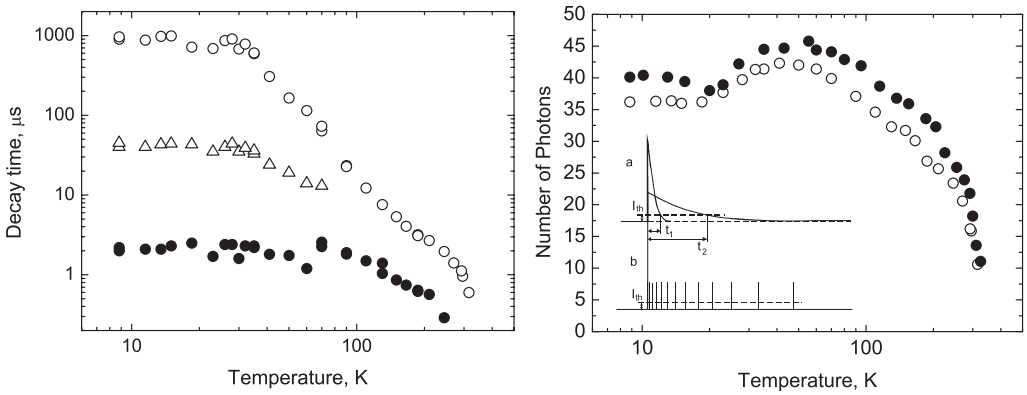

(a) Three components of decay constants **(b)** Light yields of 2 CaF_2(pure) crystals

Figure 9.1: The decay time and light yield of CaF_2(pure) scintillator as a function of temperature [99].

from the baseline. From provided data in the research [99], to achieve all number of photoelectrons, the integration interval is about 2 msec, and the error of baseline measurement can be increased to 20000 p.e. Thus, the photon counting method must be used for low-temperature measurement.

9.2 Photon Counting for low temperature measurement

In this thesis, photon counting is probed as a more appropriate method to improve energy resolution. However, due to the overlap of 1p.e. signals, partial photon counting is introduced. Thus, baseline fluctuation is remained, especially near the rising edge of the waveform. Considering the average rate of photoelectrons in the waveform when using CaF_2(pure) at low temperature:

- At 293 K, the $N_{p.e.}$(Q-value) is 3838 and τ_{decay} is 1 μsec. The rate of photoelectron defined as $N_{p.e.}/\tau_{decay}$ is about 3.8 p.e./nsec.
- At 30 K, the $N_{p.e.}$(Q-value) is 15352 and τ_{decay} is 40 μsec. The rate of photoelectron is about 0.4 p.e./nsec.

With the less rate of photoelectrons, the overlap probability is much reduced; thus, the photon counting method is more effective.

Photon counting method cannot reduce the fluctuation from the dark current and the unknown fluctuation mentioned in chapter 7. Table 9.1 indicates the estimation of fluctuations and energy resolution obtained in the

Table 9.1: Estimate energy resolution with cryogenic CaF_2(pure) and photon counting with waveform interval of 2 msec

Statistical Fluctuation	124 p.e. ($\sim$ 0.8 %)	
Baseline Fluctuation	20000 p.e. ($\sim$ 130 %)	removed
Unknown Fluctuation	60-70 p.e. ($\sim$ 0.4 %)	not changed
Dark Current	35 p.e. ($\sim$ 0.2 %)	
Energy Resolution	$\sim$ 0.9 %	no baseline fluc.

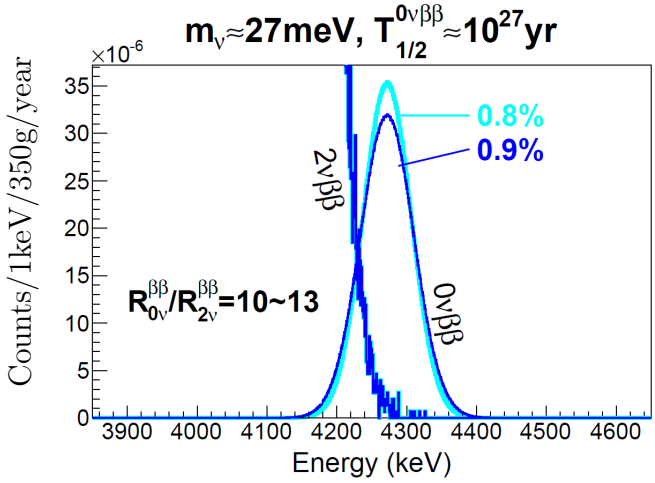

Figure 9.2: The simulation spectrum of $0\nu\beta\beta$ and $2\nu\beta\beta$ with resolution of 0.8-0.9 % at Q-value. The ratio of $0\nu\beta\beta$ over $2\nu\beta\beta$ is ranging 10-13. The $T^{0\nu}_{1/2}$=10^{27}year is equivalent to the $\langle m_{\beta\beta}\rangle$≈27-118 meV (using the NME values introduced in chapter 1).

measurement with cryogenic CaF_2(pure) scintillator and by photon counting. The energy resolution is obtained assuming that baseline fluctuation is removed and unknown fluctuation estimated in chapter 7 is not changed. Consequently, the total fluctuation at Q-value is about 0.9 % when baseline fluctuation is all rejected. With the energy resolution about 0.8 - 0.9 %, the detector can be ready for the sensitivity of $T^{0\nu}_{1/2}$=10^{27}year (Figure 9.2). From equation 1.8, the $\langle m_{\beta\beta}\rangle$≈27 meV is obtained with $G^{0\nu}$ of 2.47×10^{-25} $yr^{-1}eV^{-2}$ and the NME(EDF) of 2.37 [35]. Using CaF_2(pure) operated at cryogenic temperature and photon counting method, the estimated sensitivity of CANDLES detector may get over the current world-best sensitivity ($\langle m_{\beta\beta}\rangle$≈61-165meV) reported by KamLAND-Zen collaboration [48]. The obtained energy resolution by low-temperature CaF_2(pure) and photon counting is estimated in a very promising case. An experimental study is necessary to provide more realistic value of energy resolution.

Acknowledgments

I wish to express my sincere appreciation to my supervisor, Professor Masaharu Nomachi. He convincingly guided and encouraged me to be professional and do the right thing. Without his persistent help and troubleshooting, the goal of this project would not have been realized.

In this research, I received much support from the CANDLES collaboration. I want to thank Prof. T. Kishimoto, Prof. S. Yoshida, Prof. S. Umehara for the wise leadership, and the allowance to carry out my experiment in Kamioka Underground Observatory. I want to thank Prof. I. Ogawa, Prof. K. Fushimi, Prof. R. Hazama, Prof. T. Iida, Prof. K. Nakajima, Dr. Y. Takemoto for good advice during the shift in Kamioka and collaboration meetings. I also would like to thank Dr. Suzuki, and Dr. T. Maeda, for the exceptional contribution to the DAQ system. I also would like to thank the past and present collaborators other student members in CANDLES for their cooperation and excellent research work.

I wish to show my gratitude to Prof. H. Noumi, Prof. S. Yoshida, Prof. T. Shima, and Prof. M. Aoki, for their helpful comments and discussions. Following the comments and discussions, the quality of my thesis is enhanced.

I am also grateful to all the current and old members of the Nomachi group at Osaka University. I want to express gratitude to Prof. T. Shima, Prof. K. Takahisa, Mr. K. Kanagawa, Mr. M. Tsuzuki, Mr. N. V. H. Viet and Mr. K. Miyamoto, for the support and experience. I want to thank Prof. Y. Sugaya for the comments and advice in my first paper. I want to thank Ms. J. Nakajima and Ms. H. Yanou, for their daily support.

I wish to express my deepest gratitude to my family members, Ms. Nguyen T. Lieu, Mr. Bui D. Tuan, Ms. Huynh T. B. Yen, for their continuous support for many years of studying. I am indebted to Ms. Tran Kim Tuyet, for her invaluable encouragement and assistance during my study time in Japan.

Finally, I wish to express my gratitude to the International Physics Course, the Graduate School of Science at Osaka University, for the support in campus life. I want to thank the Nishimura International Scholarship Foundation for the financial support during my Ph.D. course.

Appendix A

Energy spectrum of double beta decay

Calculation for shape of $2\nu\beta\beta$ decay in Figure 3.1. The following calculation is referred from [102].

Single beta decay

The transition rate is given by

$$R = \frac{2\pi}{\hbar}|H_{fi}|^2 n_f \tag{A.1}$$

where H_{fi} is the matrix element and n_f is the density of final states. Since the weak interation is very short range, the matrix element could be form

$$H_{fi} = G_w \int \psi^*_{Nf} H_N \psi_{Ni} \psi^*_e \psi^*_{\bar{\nu}} d^3\vec{r} \tag{A.2}$$

We would assume lepton wave functions are plane wave,

$$\psi_l = \frac{1}{\sqrt{V}} e^{i\vec{k}\vec{r}} \tag{A.3}$$

where the wave function is normalized to 1 in an arbitrarily large volume V. The wave length of electron and anti-neutrino is much longer than the nuclear size. Therefore, expansion of exponential will be a good approximation. We will take the first term of the expansion, which is "one".

$$H_{fi} = \frac{G_W}{V} \int \psi^*_{Nf} H_N \psi_{Ni} d^3\vec{r} = \frac{G_W}{V} M_{fi} \tag{A.4}$$

where M_{fi} is a nuclear matrix element describing a nuclear transition. Assuming the anti-neutrino mass is zero, the transition rate with Coulomb potential after a straight-forward derivation is:

$$dR = \frac{G_W^2}{2\pi^3\hbar^7c^6}|M_{fi}|^2F(Z+1,E_e)E_ep_ec(Q-E_e)^2dE_e \tag{A.5}$$

where F is Fermi-function. The Fermi function for the electron will be approximated as

$$F(Z,E_e) \approx \frac{2\pi\eta}{1-e^{-2\pi\eta}} \approx 2\pi Z\alpha\frac{1}{\beta} = 2\pi Z\alpha\frac{E}{pc} \tag{A.6}$$

when $\eta = \frac{Ze^2}{4\pi\epsilon_0\hbar c}\frac{1}{\beta} = \frac{Z\alpha}{\beta}$ for the electron. Consequently,

$$dR = \frac{G_W^2 Z\alpha}{\pi^2\hbar^7c^6}|M_{fi}|^2E_e^2(Q-E_e)^2dE_e \tag{A.7}$$

is obtained for the electron energy spectrum.

Two-neutrino double beta decay

The case of double beta decay can be calculated as the same way. The transition matrix element is

$$H_{fi} = G_w^2\int \psi_{Nf}^*H_N\psi_{Ni}\psi_e^*\psi_{\bar{\nu}}^*\psi_e^*\psi_{\bar{\nu}}^*d^3\vec{r} = \frac{G_w^2}{V^2}M_{fi} \tag{A.8}$$

The transition rate will be

$$dR = \frac{2\pi(4\pi)^3G_W^4}{\hbar(2\pi\hbar)^{12}c}|M_{fi}|^2\int p_{e1}^2p_{e2}^2p_{\bar{\nu}1}^2(Q-E_{e1}-E_{e2}-cp_{\bar{\nu}1})^2dp_{e1}dp_{e2}dp_{\bar{\nu}1} \tag{A.9}$$

Integrating over anti-neutrino momentum,

$$\int_0^{Q-E_{e1}-E_{e2}} c^2p_{\nu1}^2(Q-E_{e1}-E_{e2}-cp_{\nu1})^2cdp_{\nu1} = \frac{1}{30}(Q-E_{e1}-E_{e2})^5 \tag{A.10}$$

The transition probability is

$$dR = \frac{G_W^4}{15\times2^6\pi^8\hbar^{13}c^7}|M_{fi}|^2\int E_{e1}p_{e1}E_{e2}p_{e2}(Q-E_{e1}-E_{e2})^5dE_{e1}dE_{e2} \tag{A.11}$$

Taking into Coulomb potential

$$dR \propto \int E_{e1}^2 E_{e2}^2 (Q - E_{e1} - E_{e2})^5 dE_{e1} dE_{e2} \tag{A.12}$$

In order to obtain the sum energy spectrum, the energy difference is integrated over the physical energy region. Here, summed kinetic energy will be $T = E_{e1} + E_{e2} - 2mc^2$ and the difference of the kinetic energies will be $t = E_{e1} - E_{e2}$. The physical region for t is between -T and T.

$$dR \propto (Q' - T)^5 \left[(T + 2mc^2)^4 T - \frac{2}{3}(T + 2mc^2)^2 T^3 + \frac{1}{5} T^5 \right] dT \tag{A.13}$$

As the result, we can obtain

$$dR \propto \left[\left(\frac{1}{30}\right) T^4 + \left(\frac{1}{3}\right)(mc^2) T^3 + \left(\frac{4}{3}\right)(mc^2)^2 T^2 + 2(mc^2)^3 T + (mc^2)^4 \right] \times (Q' - T)^5 T dT \tag{A.14}$$

Appendix B

PMT Resolution

The following calculation is carried out to study the contribution of PMT fluctuation in the energy resolution. It turns out that the statistical number of electrons collected at PMT anode is affected by the statistical fluctuation of photoelectrons emitted at PMT cathode, the non-statistical fluctuation of scintillation in the crystal and the multiplication fof PMT dynodes.

Generic function

Generic function is quite useful in calculation of mean and variance of a defined distribution. A variable n has the distribution p_n, the generic function of p_n is defined as:

$$G(t) = \sum_{n=0}^{\infty} p_n t^n \tag{B.1}$$

Differentiate the generic function with t,

$$G'(t) = \sum_{n=0}^{\infty} n p_n t^{n-1} \tag{B.2}$$

$$G''(t) = \sum_{n=0}^{\infty} n(n-1) p_n t^{n-2} \tag{B.3}$$

So that,

$$G(1) = 1,\ G'(1) = \langle n \rangle\,,\ G''(1) = \langle n^2 \rangle - \langle n \rangle \tag{B.4}$$

The variance,

$$\sigma^2 = G''(1) + G'(1) - G''(1)^2 \tag{B.5}$$

Fluctuation of number of photoelectrons at PMT cathode

The number of photon emitted by a scintillator distributing as a function f_m. The photon has a mean probability μ to be detected and converted to a photoelectron. The number of photoelectron distributing as g_n:

$$g_n = \sum_{m=n}^{\infty} {}_mC_n \mu^n (1-\mu)^{m-n} f_m \tag{B.6}$$

The generic function is

$$G(t) = \sum_{n=0}^{\infty} g_n t^n = \sum_{m=0}^{\infty} f_m (1-\mu+\mu t)^m = F(1-\mu+\mu t)$$

where $F(t)$ is the generic function of f_m. The variance of photonelectron is:

$$\begin{aligned} \sigma_g^2 &= G''(1) + G'(1) - G''(1)^2 \\ &= \mu^2 \sigma_f^2 + \mu(1-\mu) \langle f \rangle \end{aligned} \tag{B.7}$$

Dividing by $\langle g \rangle^2 = (\mu \langle f \rangle)^2$,

$$\left(\frac{\sigma_g}{\langle g \rangle}\right)^2 = \left[\left(\frac{\sigma_f}{\langle f \rangle}\right)^2 - \frac{\mu}{\langle g \rangle}\right] + \frac{1}{\langle g \rangle} \tag{B.8}$$

In case that the number of scintillator photons fluctuate statistically (i.e. Poisson distribution), $\sigma_f = \sqrt{\langle f \rangle}$ and the fluctuation of photoelectron is:

$$\left(\frac{\sigma_g}{\langle g \rangle}\right)^2 = \frac{1}{\langle g \rangle} \tag{B.9}$$

The number of photoelectron follows the Poisson distribution. Only the non-statistical fluctuation makes additional fluctuation on the number of photoelectrons.

Fluctuation of number of electrons at PMT dynode

When m electrons arrive a dynode, each electron is multiplied to n_1, n_2, n_3, ... n_m where n has distribution r_n. With the distribution of the number of

input electrons is p_m, the distribution of the number of output electrons is q_n defined as:

$$q_n = \sum_{m=0}^{\infty} p_m \prod_{i=1}^{m} \sum_{n_i=0}^{\infty} r_{n_i} \delta \left(n - \sum_{j=0}^{m} n_j \right) \tag{B.10}$$

Respectively define the generic functions for input electrons, output electrons and electrons generated by one of input electrons:

$$P(t) = \sum_{n=0}^{\infty} p_n t^n,\ Q(t) = \sum_{n=0}^{\infty} q_n t^n,\ R(t) = \sum_{n=0}^{\infty} r_n t^n \tag{B.11}$$

Combing equations B.10 and B.11, the generic function for output electrons can be derived as:

$$Q(t) = \sum_{m=0}^{\infty} p_m R(t)^m = P(R(t)) \tag{B.12}$$

Fluctuation of the number of electrons collected at PMT anode

Define n is the total dynodes of a PMT. Electrons bombard with n dynodes before arriving at the PMT anode. Define the generic function of electrons generated at the nth dynode as $Q_n(t)$,

$$Q_n(t) = Q_0(R_1(R_2(R_3(...R_n(t)...)))) \tag{B.13}$$

Differentiate Q_n by t,

$$Q'_n(t) = Q'_0(R_1)R'_1(R_2)R'_2(R_3)...R'_{n-1}(R_n)R'_n(t) \tag{B.14}$$

Define the mean values:

$$Q'_n(1) = N_A,\ Q'_n(0) = N_C,\ R'_i(1) = \lambda_i \tag{B.15}$$

$$\Rightarrow N_A = N_C \lambda_1 \lambda_2 \lambda_3 ... \lambda_n \tag{B.16}$$

where N_A: is the number of electrons collected at the PMT anode.

N_C: is the number of photoelectrons generated at the PMT cathode.

λ_i: is the multiplication of the ith dynode.

For the case of n dynodes, the fluctuation becomes to:

$$\left(\frac{\sigma_A}{N_A}\right)^2 = \left(\frac{\sigma_C}{N_C}\right)^2 + \frac{1}{N_C}\left(\frac{\sigma_1}{\lambda_1}\right)^2 + \frac{1}{N_C\lambda_1}\left(\frac{\sigma_2}{\lambda_2}\right)^2 \tag{B.17}$$

$$+ ... + \frac{1}{N_C\lambda_1...\lambda_{n-1}}\left(\frac{\sigma_n}{\lambda_n}\right)^2 \tag{B.18}$$

For the case of single photoelectron ($N_C = 1$), the fluctuation is:

$$\left(\frac{\sigma_A}{N_A}\right)^2_{1p.e.} \approx \left(\frac{\sigma_1}{\lambda_1}\right)^2 = \frac{1}{\lambda_1} \tag{B.19}$$

Consequently,

$$\left(\frac{\sigma_A}{N_A}\right)^2 = \left(\frac{\sigma_C}{N_C}\right)^2 + \frac{1}{N_C}\left(\frac{\sigma_A}{N_A}\right)^2_{1p.e.} \tag{B.20}$$

With N_X is the number of scintillation photons and σ_X is the non statistical fluctuation of scintillation photons, the fluctuation of electrons collected at PMT anode is:

$$\left(\frac{\sigma_A}{N_A}\right)^2 = \frac{1}{N_C} + \left(\frac{\sigma_X}{N_X}\right)^2 + \frac{1}{N_C}\left(\frac{\sigma_A}{N_A}\right)^2_{1p.e.} \tag{B.21}$$

Appendix C

Signal Overlap in Digitization Error Estimation

The widths (w) of 1p.e. signals in different PMTs are different. The digitization error of N photoelectrons is proportional to $N \times w$ if there is no overlap. As mentioned in section 4.2 and section D, the overlap of 1p.e. signals results in a reduction of digitization error. In this appendix, the derivation of this reduction factor is discussed.

The probability of being pedestal is derived as follow. A BIN has pedestal data means there is no 1p.e. signal in the preceding w. The expectation number of p.e. in the period w is:

$$p(t)w = N\frac{w}{\tau}e^{-t/\tau} \tag{C.1}$$

where τ is decay time of the scintillator, and N is the total number of p.e. The number of p.e. obey the Poisson distribution. So, the probability of pedestal is:

$$q(t) = exp\left(-p(t)w\right) = exp\left(-N\frac{w}{\tau}e^{-t/\tau}\right) \tag{C.2}$$

The number of BIN, which is not pedestal is:

$$N_{signal} = \sum_i (1 - q(t_i)) = \frac{1}{\delta}\int_0^T (1 - q(t))dt \tag{C.3}$$

where δ is BIN width (2 nsec), and T is the integration interval. Introducing a variable x defined as:

$$x = e^{-t/\tau} \tag{C.4}$$

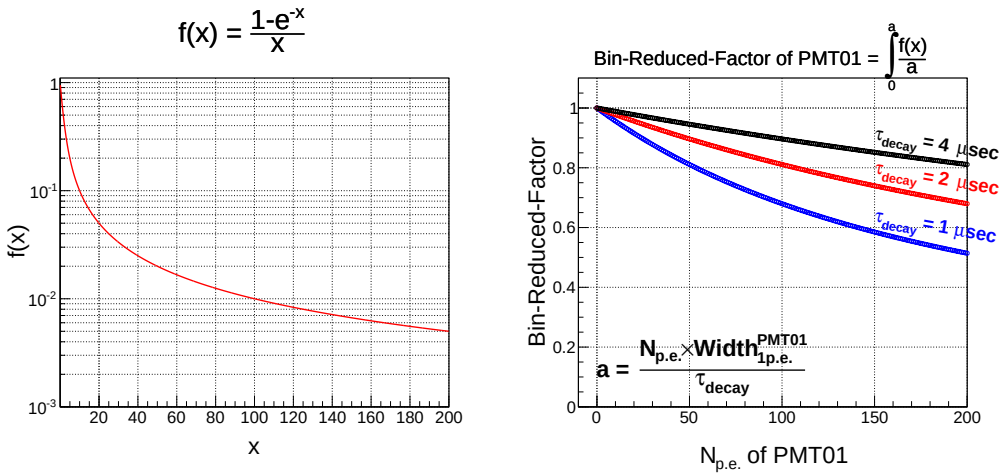

(a) **(b)**

Figure C.1: The calculation of $(1 - e^{-y})/y$ (a) and the calculation of γ of PMT01 with different decay constant of 1 μsec, 2 μsec and 4 μsec (b).

The number of BIN, which is not pedestal is:

$$N_{signal} = \frac{\tau}{\delta} \int_{e^{-T/\tau}}^{1} \left[1 - exp\left(-N\frac{w}{\tau}x\right)\right] \frac{dx}{x} \tag{C.5}$$

Declare variable $y = \frac{Nw}{\tau}x$, the above equation is rewritten as:

$$N_{signal} = \frac{\tau}{\delta} \int_{\frac{Nw}{\tau}}^{0} \frac{1 - e^{-y}}{y} dy \tag{C.6}$$

If there is no signal overlap, the number of signal BIN, which is not pedestal, is $\frac{Nw}{\delta}$. Therefore, the number of signal BIN is reduced as a factor γ:

$$\gamma = N_{signal}\frac{\delta}{Nw} = \frac{\tau}{Nw} \int_{\frac{Nw}{\tau}}^{0} \frac{1 - e^{-y}}{y} dy \tag{C.7}$$

γ is obtained from the average of $(1 - e^{-y})/y$ between 0 and Nw/τ. Here, Nw/τ is occupancy of N signals in the decay time τ. There is no analytical solution on this integral. Therefore, γ is numerically calculated. The γ is used in equation 4.3 for calculation of Digitization Error in CANDLES spectrum.

Appendix D

Digitization error: Signal Overlap and Peak Shifting

Digitization Error effect on the single photoelectron charge

The digitization error affects on single photoelectron (1p.e.) charge value within the signal width:

$$\delta_{\text{p.e.}}^{\text{iPMT}} = \text{w}^{\text{iPMT}} \times (\text{MeasuredPedestal}^{\text{iPMT}} - \text{TruePedestal}^{\text{iPMT}}) \tag{D.1}$$

and the 1p.e. charge obtained from measurement is:

$$\Delta_{\text{p.e.}}^{\text{iPMT}} = \text{True}_{\text{p.e.}}^{\text{iPMT}} + \delta_{\text{p.e.}}^{\text{iPMT}} \tag{D.2}$$

where $\Delta_{\text{p.e.}}$: the 1p.e. charge value obtained from measurement (ADC)

$\text{True}_{\text{p.e.}}$: the true 1p.e. charge value (ADC)

$\delta_{\text{p.e.}}$: digitization error effect on the 1p.e. charge value (ADC)

w: number of signal-pedestal points of 1p.e. signal (timebin)

iPMT: the ith PMT, and $1 \leq \text{i} \leq 62$

As the Digitization Error is canceled at measured pedestals of 244.0 ADC, 244.5 ADC and 245.0 ADC (Figure 4.6), the obtained 1p.e. charge at either one of these measure pedestals is equivalent to the $\text{True}_{\text{p.e.}}$. With measured pedestal ranging from 244.1 ADC to 244.9 ADC:

$$\Delta_{\text{p.e.}}^{\text{iPMT}} = \text{Slope}^{\text{iPMT}} \times \text{MeasuredPedestal}^{\text{iPMT}} \ (+ \textit{Intercept}) \tag{D.3}$$

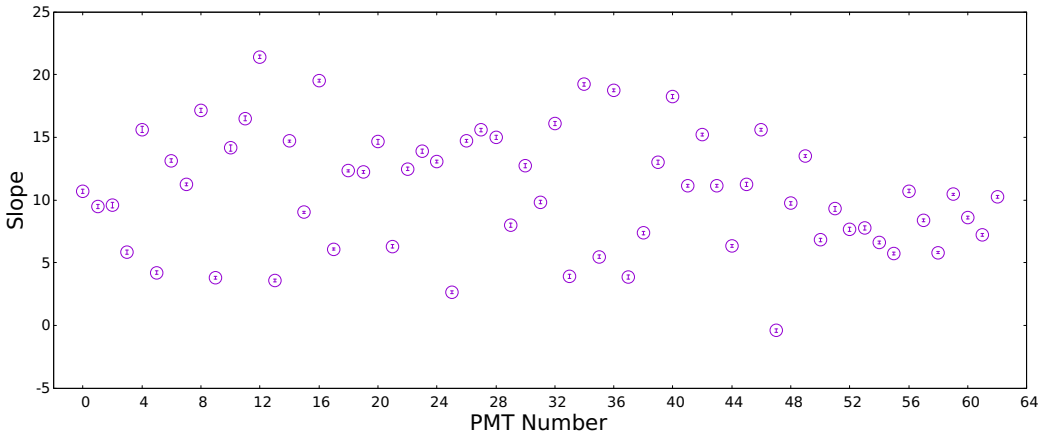

Figure D.1: The linear coefficient Slope between $\Delta_{\text{p.e.}}$ and Measured Pedestal. Theses values are results by fitting the data from [93]. The Slope at the PMT0 is the average slope of 62 PMTs.

Figure D.1 shows the slope parameter of every PMT, and the slope at PMT0 is all PMTs' average value, which is about 10.7±0.1. The digitization error can be canceled at measured pedestal of 244.5 ADC, and the obtained charge at this measured pedestal is $\text{True}_{\text{p.e.}}$. Therefore, the digitization error effect on 1p.e. charge can be estimated as follow:

$$\delta_{\text{p.e.}}^{\text{iPMT}} = \text{Slope}^{\text{iPMT}} \times \left(\text{Measured Pedestal}^{\text{iPMT}} - 244.5\right) \tag{D.4}$$

The width of 1p.e. signal

For calculating the digitization error effect on 1p.e. charge value of a PMT, the width of 1p.e. signal is an essential factor (equation D.1). In this section, the determination of 1p.e. widths of 62 PMTs is introduced. The width of an 1p.e. signal is the number of signal points of that 1p.e. signal. The number of signal points is linearly proportional to the number of photoelectrons if there is no overlap of 1p.e. signals.

An analysis is executed using the experimental data in Chapter 5 to see the correlation of signal points and the number of photoelectrons. Pedestals of 62 PMTs set at 244 ADC to 245 ADC, the signal points are defined as the ones whose digitized values are less than 244 ADC. In this analysis, in every PMT the signal points and photoelectrons are counted. The 2-dimension histogram showing their correlations in PMT01 and PMT02 are shown in Figure D.2. The difference in distributions obtained in 2 PMTs is due to the dependence of overlap probability on the 1p.e. signal width. For a few first

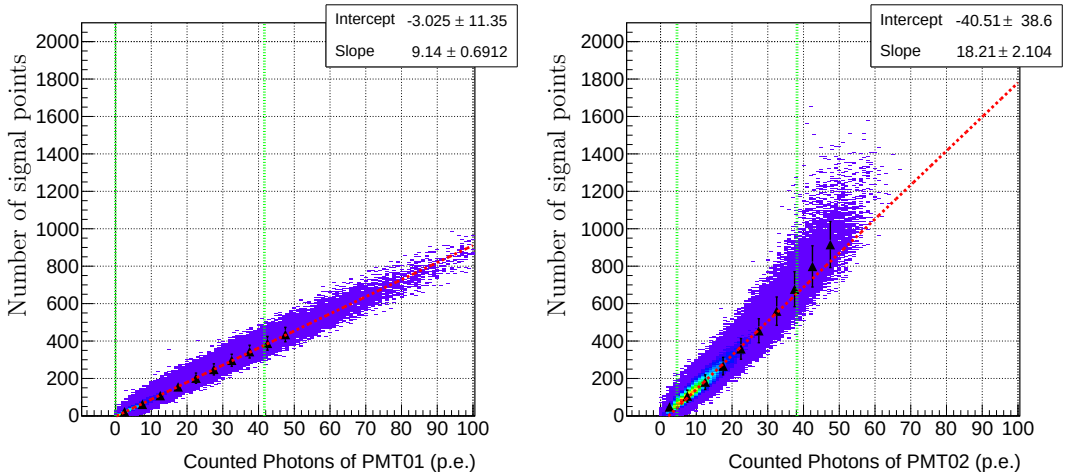

(a) PMT01 **(b)** PMT02

Figure D.2: Number of signal points as a function of number of photoelectrons in PMT01 (a) and PMT02 (b). case of PMT01, whose 1p.e. width is about 18 nsec, and PMT02, whose 1p.e. width is about 36 nsec. The red-dashed lines indicate the linear fitting, which results the slope as the number of signal points per photoelectron. The fitting area, which is marked with green-dashed lines, of number of photoelectrons is determined by the Mean and standard deviation (RMS) of number of photoelectrons.

tens of photoelectrons, the number of signal points is assumed to be linearly proportional to number of photoelectrons. Thus, the linear fitting is applied to estimate the number of signal points per 1p.e. signal (or the 1p.e. width).

The slope parameters of 62 PMTs are plotted in Figure D.3. The width of 1p.e. signals from 10-inch PMTs are narrower than the one of 13-inch and 20-inch PMTs (Figure D.4).

Overlap of 1p.e. signals - Reduction factor

A CaF_2 signal contains many 1p.e. signals created by the photocathodes. Because of the digitization error, one may estimate the digitization error effect in a CaF_2 signal as follow by assuming the 1p.e. signals created in a PMT are not overlapped each other:

$$\Omega' = \sum_{1}^{62} \omega'^{\mathrm{iPMT}} = \sum_{1}^{62} \mathrm{n}_{\mathrm{p.e.}}^{\mathrm{iPMT}} \times \delta_{\mathrm{p.e.}}^{\mathrm{iPMT}} \tag{D.5}$$

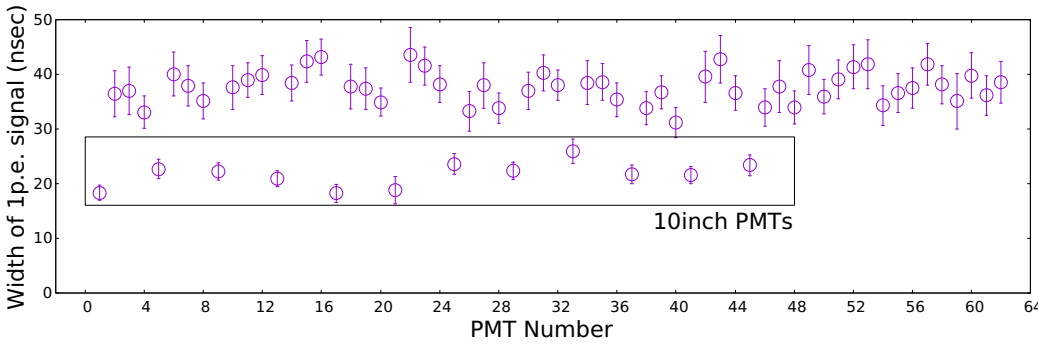

Figure D.3: Obtained widths of 1p.e. signals of 62 PMTs. The width is defined as width = signal Points × 2 nsec. The 1p.e. signals from 10-inch PMTs have narrower shapes (circled in black-solid line) compared to the shapes of 1p.e. signals in 13-inch and 20-inch PMTs.

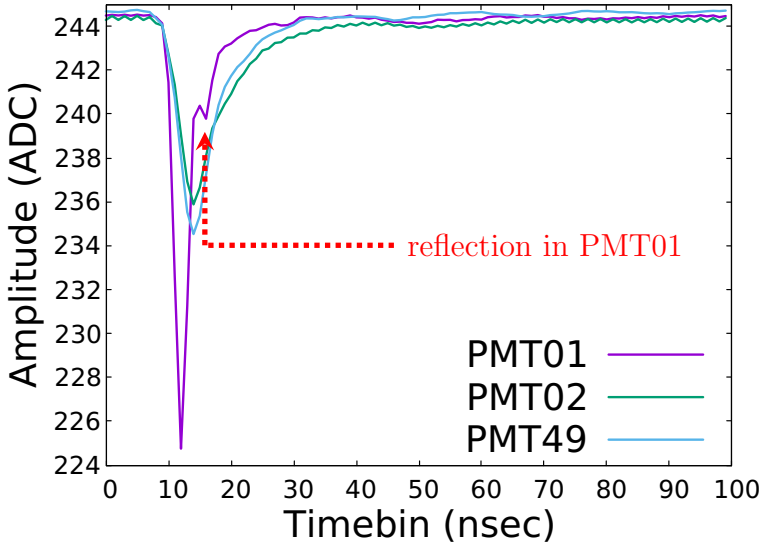

Figure D.4: A comparison of the shapes of 1p.e. signals from PMT01 (10-inch), PMT02 (13-inch) and PMT49 (20-inch). Each average waveform is made using about 500 events of LED measurement data from reference [93].

where Ω': the digitization error effect in a CaF_2 signal with assumption of no overlap of 1p.e. signals (ADC),

ω'^{iPMT}: the digitization error effect on the ith PMT with assumption of no overlap of 1p.e. signals (ADC),

$n_{p.e.}^{iPMT}$: the number of p.e. obtained in the ith PMT.

However, in fact, the 1p.e. signals in a PMT are overlapped. In Figure

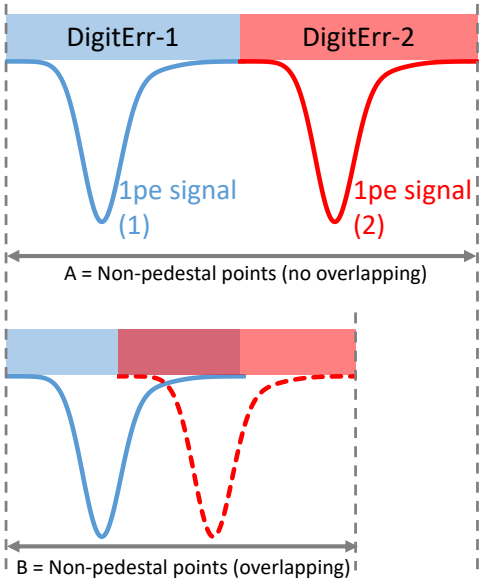

Figure D.5: Demonstration of non-overlap (top) and overlap (bottom) of two single photoelectron signals. The accumulated digitization error in 2 cases are different. If the photoelectron signals are overlapped each other, the number of signal points are reduced (A>B), hence, the digitization error is reduced by B/A.

D.5, the digitization error accumulated when integrating two single photoelectrons in non-overlap and overlap cases are different. In the case of signal overlap, the number of signal points is decreased so that the digitization error accumulated is also reduced. Therefore, to estimate the digitization error in CaF_2 signal, it is needed to calculate the reduction factor defined as:

$$\text{Reduce Factor} = \frac{\text{signal Points}^{\text{Overlap}}}{\text{signal Points}^{\text{Non-Overlap}}} \tag{D.6}$$

The reduction factor of a PMT can be calculated as:

$$\gamma^{\text{iPMT}} = \frac{1}{\text{a}} \int_{\text{e}^{-\text{T}/\tau}}^{\text{a}} \frac{1-\text{e}^{-\text{y}}}{\text{y}} \text{dy}, \text{ with a} = \text{n}_{\text{p.e.}}^{\text{iPMT}} \frac{\text{w}^{\text{iPMT}}}{\tau} \tag{D.7}$$

where γ^{iPMT}: is the reduction factor in the ith PMT,

τ: is the CaF_2's decay constant (1000 nsec),

a: is the occupancy of $\text{n}_{\text{p.e.}}^{\text{iPMT}}$ in the decay constant τ,

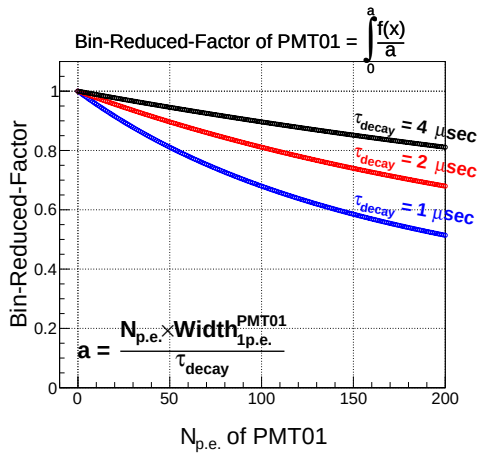

(a) PMT01

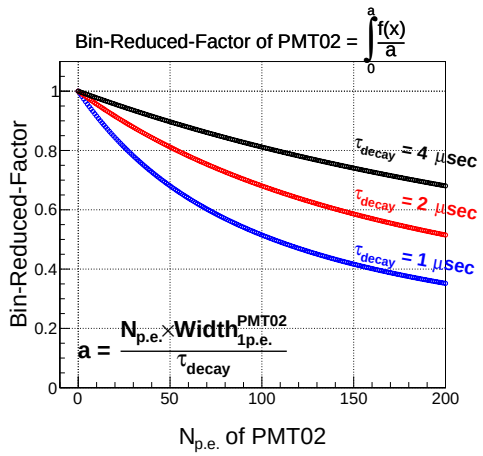

(b) PMT02

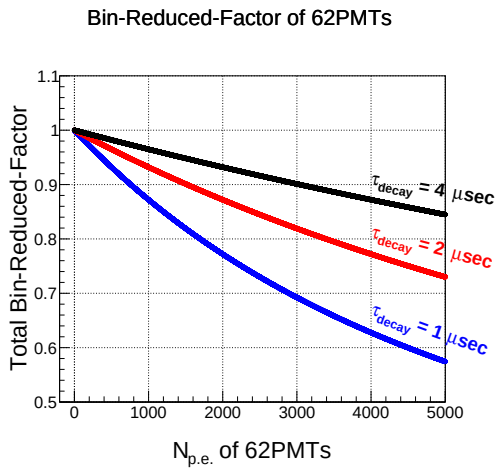

(c) 62 PMTs

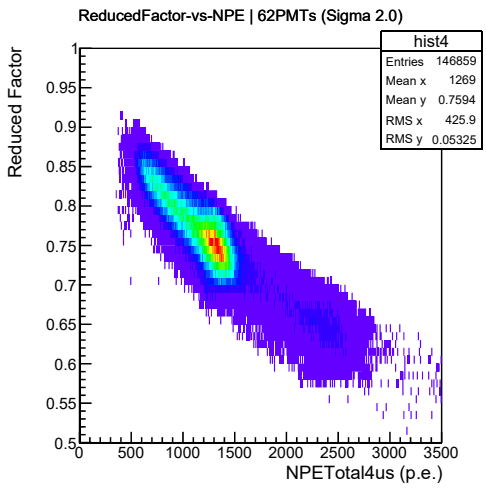

(d) Experimental data

Figure D.6: Reduction factor as a function of obtain number of photoelectrons. The calculation reduction factors for PMT01 (10 inch PMT), PMT02 (13 inch PMT), 62 PMTs are shown in figure (a), (b) and (c). The 1p.e. width of PMT01 is shorter than PMT02's, so the reduction factor in PMT01 is higher (less overlap). Different decay constants are used in these plots 1 μsec (blue), 2 μsec (red) and 4 μsec (black). The right figure is a 2-dimensional plot of reduction factor and number of photoelectrons using experimental data of CANDLES III. The right figure is corresponding to the decay constant of about 1 μsec as the current CaF_2 decay constant.

T_{INT}: is the integration interval (4000 nsec).

Figure D.6 shows 4 plots showing the dependence of reduction factor on the number of photoelectrons. With more number of photoelectrons, the signal points are decreased, thus, so are the reduction factor. Additionally, a shorter decay constant implies a higher overlap probability or a smaller reduction factor. Moreover, the wider width of 1p.e. enhances the chance of signal overlap and causes the decrement of reduction factor (PMT01-10inch and PMT02-13inch).

Using the above equations, the sum reduction factor for 62 PMTs can be calculated as:

$$\Gamma = \frac{\sum^{62} n_{p.e.}^{iPMT} w^{iPMT} \gamma^{iPMT}}{\sum^{62} n_{p.e.}^{iPMT} w^{iPMT}} \tag{D.8}$$

Figure D.6-(c) shows the sum reduction factor of 62 PMTs as a function of number of photoelectrons. In this plot, the $e^{-T/\tau}$ is assumed to be 0, the decay constant is set, respectively, at 1 μsec, 2 μsec and 4 μsec; and the number of photoelectrons collected at every PMT is assumed to be the identical. For comparison, a 2-dimensional scatter plot of reduction factor and obtained number of photoelectrons is prepared (Figure D.6-(d)). With the current setup, the decay constant of CaF_2 is about 1 μsec, and the correlation in Figure D.6-(d) is quite consistent with the estimation in Figure D.6-(c).

Estimate Digitization Error in Physics Run data

In this section, the effect of digitization error on the energy spectrum of Run010 of CANDLES III is discussed. The experimental data in Physics Run of 480 Sub Runs (406 days) are analyzed to obtain the digitization errors.

During data taking, some accidents, which are power outages and high voltage shutdown, occurred, and they led to the change of pedestal values. The pedestals were, then, readjusted as soon as the problem recognized. In Figure D.7, the blue points are the average pedestal of 62 PMTs plotted as a function of Sub Run (SRun), which is equivalent to about 1 day of measurement. The red-dashed line is the expected value 244.5 ADC, and the green-dashed lines inform the limited range of 244 ADC to 245 ADC. The solid-red lines show change of pedestals due to accidents, and the solid-blue lines show the pedestal (re-)adjustments.

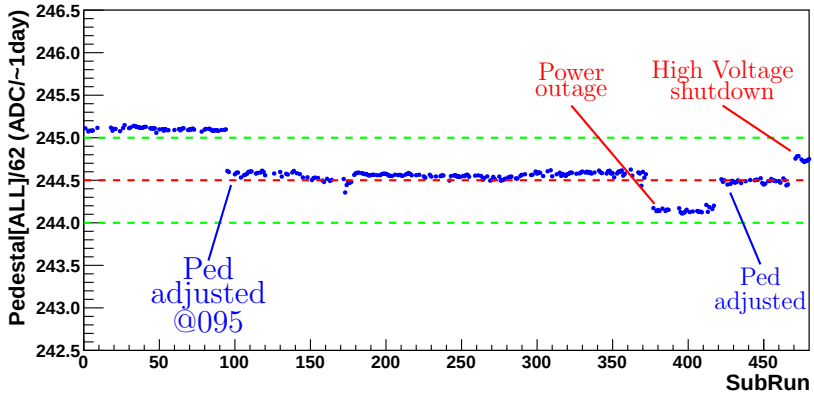

Figure D.7: The profile of average pedestal of 62 PMTs by time using 1-year data of Physics Run. At SRun095, the pedestal of all PMTs are set to 244.5 ADC. During data taking, the pedestal value were changed due to some accidents (power outage, high voltage shutdown) and (re-)adjustments.

When the pedestal changed, the digitization error is affected, and it leads to the change of peak position. A study was carried out to probe the correlation between the changes of pedestal and the changes of peak position. Both peak positions and digitization error are calculated in p.e. unit in this analysis.

The digitization error was estimated in every event of each SRun, and the mean value (μ_{DE}) of digitization error distribution is obtained. To compare the μ_{DE} with the peak positions, both values are normalized using data from SRun100-SRun300. Figure D.8 shows the consistence of normalized peak positions and digitization error at ^{40}K and ^{208}Tl peaks. There are big differences between μ_{DE} and peak positions at some SRuns. It may be due to the method for estimation of digitization error by assuming linear correlation. If the pedestal is close to 244 ADC or 245 ADC, the linear estimation is not good. At the SRuns where μ_{DE} and peak positions are big different, there are PMTs whose Pedestal near 244 ADC or 245 ADC.

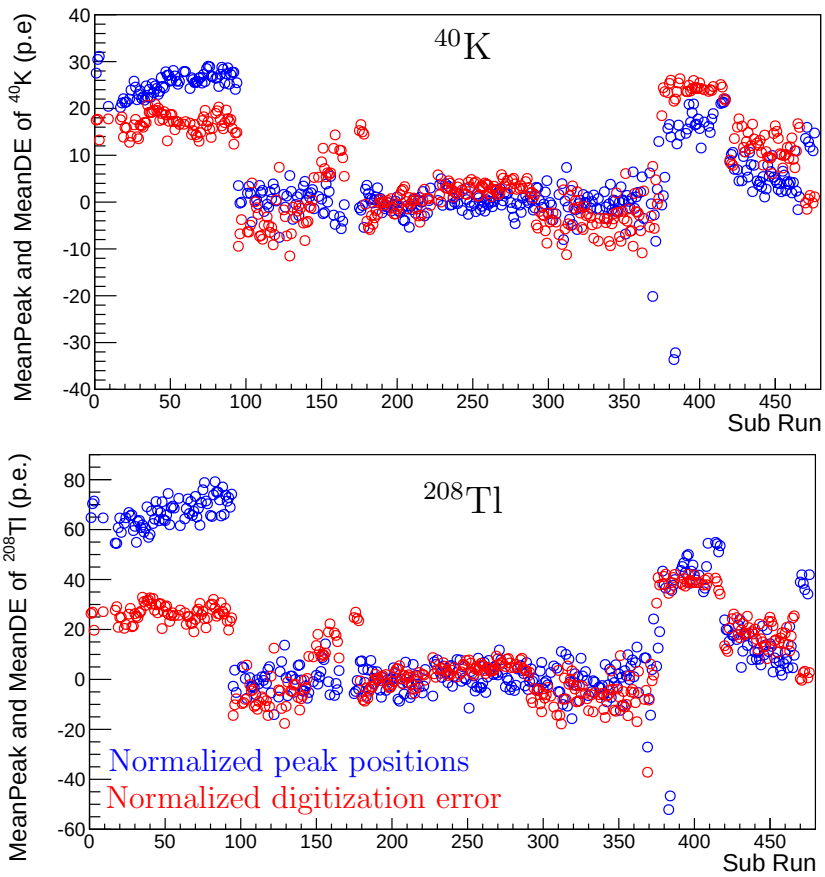

Figure D.8: The profile of normalized peak positions and normalized DEEP at ^{40}K (top) and ^{208}Tl (bottom) peaks are plotted with blue circles and red circles, respectively.

Appendix E

Pedestal Fluctuation - Error in baseline measurement

Among the factors of baseline fluctuation, the error of pedestal measurement is probed to be the most severe one (as discussed in section 4.5 of chapter 4). In this appendix, the uncertainty of pedestal is discussed.

Pedestal measurement

Define the probability of "1" to μ and that of "0" to $1-\mu$. When μ is constant, the number of "1" (n) in N samples follows binomial distribution. In this document, we discuss the case that μ has distribution $f(\mu)$. The probability of the number of "1" being "n" in N sample is:

$$P_n = \int f(\mu)_N C_n \mu^n (1-\mu)^{N-n} d\mu \tag{E.1}$$

Making the generic function (mentioned in section B of appendix B):

$$G(t) = \sum_{n=0}^{N} P_n t^n = \int f(\mu) \left(\mu t + 1 - \mu\right)^N d\mu \tag{E.2}$$

$$\Rightarrow G'(1) = \int f(\mu) N \mu d\mu = N \langle \mu \rangle \tag{E.3}$$

$$\Rightarrow G''(1) = \int f(\mu) N(N-1)\mu^2 d\mu = N(N-1) \langle \mu^2 \rangle \tag{E.4}$$

$$\begin{aligned} \sigma_n^2 &= G''(1) + G'(1) - G'(1)^2 \\ &= N(N-1)\sigma_\mu^2 + N \langle \mu \rangle (1 - \langle \mu \rangle) \end{aligned} \tag{E.5}$$

In this thesis, the pedestal is n/N:

$$\frac{\langle n \rangle}{N} = \langle \mu \rangle \tag{E.6}$$

$$\Rightarrow \left(\frac{\sigma_n}{N}\right)^2 = \frac{N-1}{N}\sigma_\mu^2 + \frac{1}{N}\langle \mu \rangle (1 - \langle \mu \rangle) \tag{E.7}$$

$$= \frac{N-1}{N}\sigma_\mu^2 + \sigma_b^2 \tag{E.8}$$

σ_b is the binomial distribution.

Difference of pedestal measurement

In this section, the distribution of the difference of two pedestal measurements in two different regions of the waveform is discussed. Respectively call them as μ_1 and μ_2 are not the same nor different. Measure the pedestal in N points. One measurement has n "1" points, and another measurement has m "1" points. The distribution of the difference $n - m = l$ is derived as following. Probability of l is:

$$Q_l = \int f(\mu_1, \mu_2) \sum_n \sum_m {}_N C_n \mu_1^n (1-\mu_1)^{N-n} {}_N C_m \mu_1^m (1-\mu_1)^{N-m} \delta(l - n + m) d\mu_1 d\mu_2 \tag{E.9}$$

Generic function is

$$H(t) = \int f(\mu_1, \mu_2)(\mu_1 t + 1 - \mu_1)^N (\mu_2 t^{-1} + 1 - \mu_2)^N d\mu_1 d\mu_2 \tag{E.10}$$

$$H'(1) = N \int f(\mu_1, \mu_2)(\mu_1 - \mu_2) d\mu_1 d\mu_2 \tag{E.11}$$

Since the distribution $f()$ is symmetry for μ_1 and μ_2, $H'(1) = 0$.

$$\begin{aligned} H''(1) = &\int f(\mu_1, \mu_2) N(N-1)\mu_1^2 d\mu_1 d\mu_2 - 2\int f(\mu_1, \mu_2) N^2 \mu_1 \mu_2 d\mu_1 d\mu_2 \\ &+ \int f(\mu_1, \mu_2) N(N-1)\mu_2^2 d\mu_1 d\mu_2 - 2\int f(\mu_1, \mu_2) N \mu_2 t^{-3} d\mu_1 d\mu_2 \end{aligned} \tag{E.12}$$

μ_1 and μ_2 have the same distribution.

$$H''(1) = 2N(N-1)\langle \mu^2 \rangle - 2N^2 \int f(\mu_1, \mu_2)\mu_1 \mu_2 d\mu_1 d\mu_2 + 2N\langle \mu \rangle \tag{E.13}$$

In general, μ_1 and μ_2 are not the same nor independent. Coherent term $\mu_c = (\mu_1 + \mu_2)/2$ and the difference term $\mu_d = (\mu_1 - \mu_2)/2$ may have independent distribution. Since the Jacobian determinant is one,

$$f(\mu_1, \mu_2) d\mu_1 d\mu_2 = g(\mu_c) h(\mu_d) d\mu_c d\mu_d \tag{E.14}$$

$$\int f(\mu_1, \mu_2) d\mu_1 d\mu_2 = \langle \mu_c \rangle = \langle \mu \rangle \tag{E.15}$$

$$\int f(\mu_1, \mu_2) \mu_1^2 d\mu_1 d\mu_2 = \langle \mu_c^2 \rangle + \frac{1}{4} \langle \mu_c^d \rangle = \langle \mu^2 \rangle \tag{E.16}$$

Then,

$$\int f(\mu_1, \mu_2) \mu_1 \mu_2 d\mu_1 d\mu_2 = \langle \mu_c^2 \rangle - \frac{1}{4} \langle \mu_d^2 \rangle = \langle \mu^2 \rangle - \frac{1}{2} \langle \mu_d^2 \rangle \tag{E.17}$$

Therefore, $H''(1)$ is:

$$H''(1) = N^2 \langle \mu_d^2 \rangle + 2N(\langle \mu \rangle - \langle \mu^2 \rangle)$$

$$\langle l \rangle = H'(1) = 0 \tag{E.18}$$

$$\langle \sigma_l^2 \rangle = H''(1) + H'(1) - H'(1)^2 = H''(1) \tag{E.19}$$

Measure the difference of pedestal is l/N:

$$\frac{\langle l \rangle}{N} = 0 \tag{E.20}$$

$$\left(\frac{\sigma_l}{N}\right)^2 = \sigma_d^2 + 2\sigma_b^2 - 2\frac{1}{N}\sigma_\mu^2 \tag{E.21}$$

When μ_1 and μ_2 are the same, σ_d is zero.

$$\left(\frac{\sigma_l}{N}\right)^2 = 2\sigma_b^2 - 2\frac{1}{N}\sigma_\mu^2 \tag{E.22}$$

When μ_1 and μ_2 fluctuate independently,

$$\int f(\mu_1, \mu_2) \mu_1 \mu_2 d\mu_1 d\mu_2 = \langle \mu^2 \rangle \tag{E.23}$$

$$\frac{1}{2}\sigma_d^2 = \langle \mu^2 \rangle - \langle \mu \rangle^2 = \sigma_\mu^2 \tag{E.24}$$

$$\left(\frac{\sigma_l}{N}\right)^2 = 2\left(\frac{N-1}{N}\sigma_\mu^2 + \sigma_b^2\right) \tag{E.25}$$

Integration over long period

Integrating longer period, μ may fluctuate during the period. In this section, λN poins are summed. λ is assumed to be an integer number (in this thesis, $N = 40$ and $\lambda = 50$). The period is divided into λ sections. μ in the section "i" is constant as μ_i. The probability of "m" points of "1" is:

$$R_m = \int f(\mu_1 ... \mu_\lambda)\delta\left(m - \sum n_i\right)\prod_{i=1}^{\lambda} {}_N C_{n_i} \mu_i^{n_i}(1-\mu_i)^{N-n_i} d\mu_i \tag{E.26}$$

Generic function is:

$$F(t) = \int f(\mu_1 ... \mu_\lambda)\prod_{i=1}^{\lambda}(\mu_i t + 1 - \mu_i)^N d\mu_i \tag{E.27}$$

$$F'(1) = \sum_{j=1}^{\lambda}\int f(\mu_1 ... \mu_\lambda) N\mu_j \prod_{i=1}^{\lambda} d\mu_i = N\sum_{j=1}^{\lambda}\langle\mu_i\rangle = N\lambda\langle\mu\rangle \tag{E.28}$$

$$F''(1) = N(N-1)\sum_{j=1}^{\lambda}\langle\mu^2\rangle + N^2\sum_{l=1}^{\lambda} 2(\lambda - l)\langle\mu_0\mu_l\rangle \tag{E.29}$$

As in the equation E.17,

$$\langle\mu_0\mu_l\rangle = \langle\mu^2\rangle - \frac{1}{2}\langle\mu_l^2\rangle \tag{E.30}$$

Here, $\langle\mu_l^2\rangle$ is the mean square of $\mu_0 - \mu_l$.

$$F''(1) = N\lambda(N\lambda - 1)\langle\mu^2\rangle - N^2\sum_{l=1}^{\lambda}(\lambda - l)\langle\mu_l^2\rangle \tag{E.31}$$

$$\sigma_m^2 = N\lambda(N\lambda - 1)\sigma_\mu^2 - N^2\lambda\sigma_b^2 - N^2\sum_{l=1}^{\lambda}(\lambda - l)\langle\mu_l^2\rangle \tag{E.32}$$

In the case of independent fluctuations, $\langle\mu_l^2\rangle = 2\sigma_\mu^2$, the above equation is modified to:

$$\sigma_m^2 = N(N-1)\lambda\sigma_\mu^2 - N^2\lambda\sigma_b^2 \tag{E.33}$$

Integration over long period (with pedestal subtraction)

In this section, λN points are summed. λ is assumed to be an integer. The period is divided into λ regions. μ in the section "i" is constant as μ_i. Pedestal is measured at the region "0" and subtracted:

$$S_k = \int f(\mu_1 ... \mu_k)\delta\left(k - \sum n_i + \lambda n_0\right) \prod_{i=0}^{\lambda} {}_N C_{n_i} \mu_i^{n_i} (1-\mu_i)^{N-n_i} d\mu_i \quad \text{(E.34)}$$

Generic function is:

$$E(t) = \int f(\mu_1 ... \mu_\lambda)(\mu_0 t^{-\lambda} + 1 - \mu_0)^N \prod_{i=1}^{\lambda} (\mu_i t^{-\lambda} + 1 - \mu_i)^N d\mu \quad \text{(E.35)}$$

$$\Rightarrow E'(1) = \sum_{j=1}^{\lambda} \int f(\mu) N \mu_j \prod_{i=1, j\neq j}^{\lambda} d\mu + \int f(\mu) N \mu_0 (-\lambda) \prod_{i=1}^{\lambda} d\mu \quad \text{(E.36)}$$

$$E''(1) = -N\lambda(\lambda+1) \left\langle \mu^2 \right| + N^2 \sum_{j=1}^{\lambda} l \left\langle \mu_l^2 \right\rangle + N\lambda(\lambda+1) \left\langle \mu \right\rangle \quad \text{(E.37)}$$

$$\sigma_k^2 = -N\lambda(\lambda+1)\sigma_\mu^2 + N^2 \sum_{j=1}^{\lambda} l \left\langle \mu_l^2 \right\rangle + N^2 \lambda(\lambda+1)\sigma_b^2 \quad \text{(E.38)}$$

σ_k^2 increases in λ^2. So, the correlation of σ_k with λ is linear. In the case of independent fluctuations, $\langle \mu_l^2 \rangle = 2\sigma_\mu^2$, and:

$$\sigma_k^2 = \lambda(\lambda+1)\left[N(N-1)\sigma_\mu^2 + N^2\sigma_b^2\right] \quad \text{(E.39)}$$

Summary

Following are the variances (σ^2) of:

- Pedestal width: $\sigma_b^2 + \left(1 - \frac{1}{N}\right)\sigma_\mu^2$
- Pedestal difference: $\sigma_d^2 + 2\sigma_b^2 - 2\left(\frac{1}{N}\right)\sigma_\mu^2$

- ADC integration: $N\lambda(N\lambda-1)\sigma_\mu^2 - N^2\lambda\sigma_b^2 - N^2\sum_{l=1}^{\lambda}(\lambda-l)\langle\mu_l^2\rangle$
- ADC integration: $-N\lambda(\lambda+1)\sigma_\mu^2 + N^2\sum_{j=1}^{\lambda} l\langle\mu_l^2\rangle + N^2\lambda(\lambda+1)\sigma_b^2$ (pedestal subtracted)

In this thesis, the $N = 40$ for pedestal calculation. We can neglect $1/N$ to 1. Assuming $\langle\mu_l^2\rangle$ is constant, the variances are approximated to:

- Pedestal width: $\sigma_b^2 + \sigma_\mu^2$
- Pedestal difference: $\sigma_d^2 + 2\sigma_b^2$
- ADC integration: $N^2\left(\lambda^2\sigma_\mu^2 + \lambda\sigma_b^2 + \lambda\sigma_d^2\right)$
- ADC integration: $\frac{1}{2}N^2\lambda(\lambda+1)\left(\sigma_d^2 + 2\sigma_b^2\right)$ (pedestal subtracted)

Applying the experimental data

For every PMT, the pedestal is calculated with the first 40 bins in the waveform. The pedestal difference is calculated by subtracting the pedestal in different regions (40 bins/region) with the pedestal in the first 40 bins. Figure E.1 shows the pedestal difference σ_d discussed in section E, and Figure E.2 shows the accumulated pedestal in a long integration period σ_k discussed in section E. Checking the σ_d as a function of timebin, we can also recognize the noise in the baseline in the PMTs. There are 5 different cycles of noises found, and they are reported in section 4.3.

Choose data from PMT49 to checking the valid of this calculation. The obtained pedestal (μ) is 244.4 ADC, the statistical fluctuation (σ_b) is 7.79×10^{-2} ADC. The obtained fluctuation (σ_{ped}) is about 2 times larger. Thus the σ_μ is $\sqrt{3}$ times larger than σ_b. In the measurement, σ_{diff} is also 2 times larger than σ_b. Therefore, σ_d is $\sqrt{2}$ times larger than σ_b. The fluctuation of ADC integration is $N\lambda\times\sigma_{diff}/\sqrt{2} = 0.12N\lambda$. It is proportional to the width. For 4000 nsec integration, this fluctuation is be accumulated to 240 ADC as it is shown in Figure E.2.

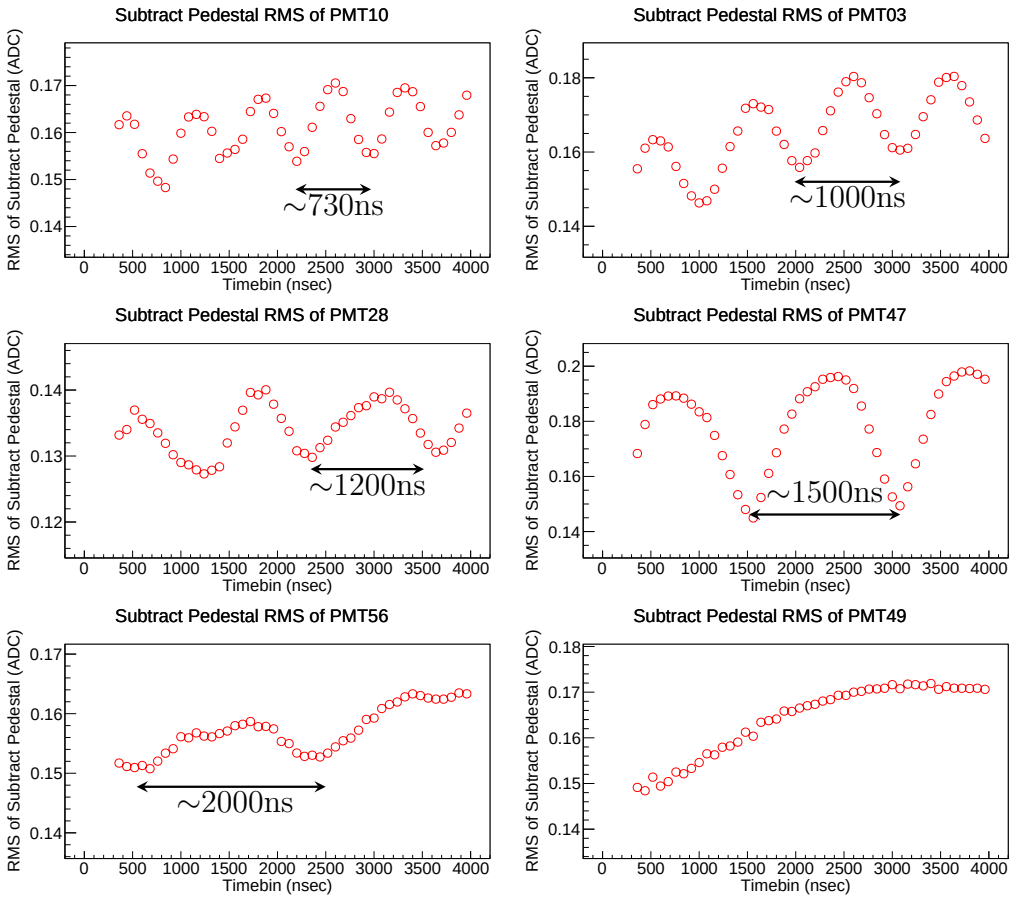

Figure E.1: The deviations of distributions of pedestal differences (σ_d) in different PMTs are plotted as a function of timebin. Different noises are visible by this checking. The solid lines are fitting functions.

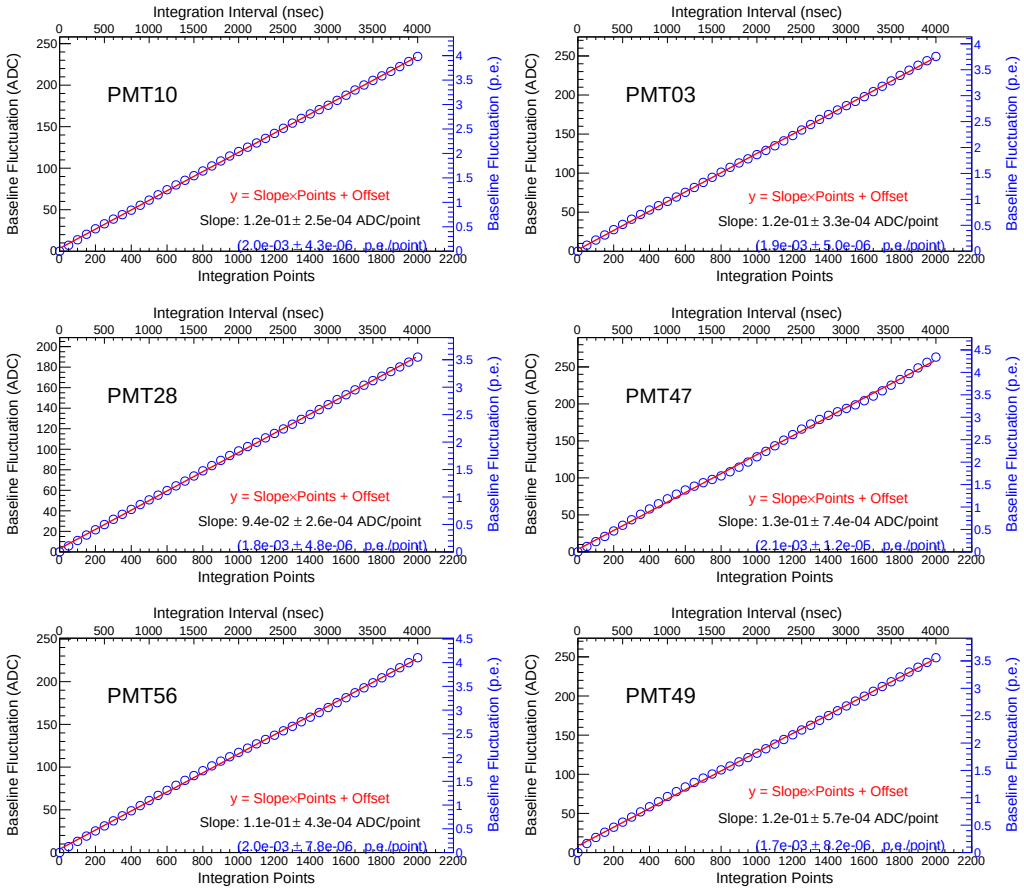

Figure E.2: The deviations of distributions of accumulated baseline in long period (σ_k) in different PMTs are plotted as a function of timebin. As mentioned in equation E.38 the σ_k is linearly correlated with the timebin.

Appendix F

Overlap in Photon Counting

Overlap in Photon Counting

The following calculation is carried out to study the overlap probability of 1p.e. signals in photon counting. Assuming the waveform of CaF_2 is assumed to be an exponential function $\mu_0 exp\left(-\frac{t}{\tau}\right)$, The total number of photoelectrons of a CaF_2 signal is: $N_0 = \mu_0\tau$. In Figure F.1, we define the shortest interval to distinguish two 1p.e. signals is minimum SIGNAL INTERVAL equivalent to w nsec. The w is mentioned in section 6.2, and the values plotted in Figure F.2 are related to w. If the interval is shorter than w, two signals are recognized as only one signal, and the existence of the other signal is lost. To avoid the lost, there should be no 1p.e. signal in the previous w nsec of a 1p.e. signal. Therefore, the probability to count a signal is the probability of no signal in preceding w nsec: $e^{-\mu w}$. The number photoelectrons counted from t $\rightarrow$ t+Δt is:

$$\Delta N = \mu \Delta t e^{-\mu w} = \mu_0 e^{-t/\tau} \Delta t e^{-\mu_0 w e^{-t/\tau}} \tag{F.1}$$

Define $s = e^{-t/\tau}$, the equation F.1 is modified to:

$$\Delta N = \mu_0 s \Delta t e^{-\mu_0 w s} \Rightarrow dN = -\mu_0 \tau e^{-\mu_0 w s} ds \tag{F.2}$$

$$\Rightarrow N = \int_1^0 -\mu_0 \tau e^{-\mu_0 w s} ds = \frac{\tau}{w}\left(1 - e^{-\mu_0 w}\right) \tag{F.3}$$

Since $N_0 = \mu_0\tau$, the above equation can be rewritten as:

$$N = \frac{\tau}{w}\left(1 - e^{-N_0 \frac{w}{\tau}}\right) \tag{F.4}$$

Function F.4 is used for fitting in Figure 6.5.

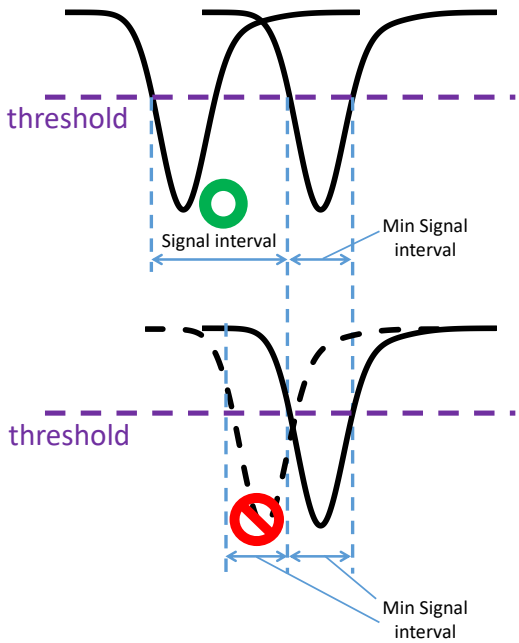

Figure F.1: SIGNAL INTERVAL in Photon Counting is the minimum interval to distinguish two single photoelectron signals. The SIGNAL INTERVAL depends on the shape of 1p.e. signal and the threshold. If the interval of two 1p.e. signals is less than the SIGNAL INTERVAL, they are counted as one signal. The top figure shows the two 1p.e. signals that can be distinguished, and the bottom figure shows two 1p.e. signals that are not distinguished.

Statistical Fluctuation in Partial Photon Counting

In partial photon counting, a waveform in each PMT is divided into two regions. The prompt region (near the rising edge) is used for signal integration; and the latter region (near the tail) is used for photon counting. In this section, the statistical fluctuation of partial photon counting is discussed. The total number of photoelectrons in the waveform is assumed to be $\mathbf{N}_0$. The decay constant of CaF_2 is τ nsec. The minimum Signal Interval is ω nsec. The prompt region is integrated from 0 nsec to $\mathbf{T}$ nsec; and the photoelectrons in the latter region is counted from $\mathbf{T}$ nsec. The number of photoelectrons in the prompt region ($\mathrm{N_P}$) is calculated as:

$$\mathrm{N_P} = \frac{\mathrm{N_0}}{\tau}\int_0^{\mathrm{T}} \exp\left(-\frac{\mathrm{t}}{\tau}\right)\mathrm{dt} = \mathrm{N_0}\left(1-\exp\left(-\frac{\mathrm{T}}{\tau}\right)\right) \tag{F.5}$$

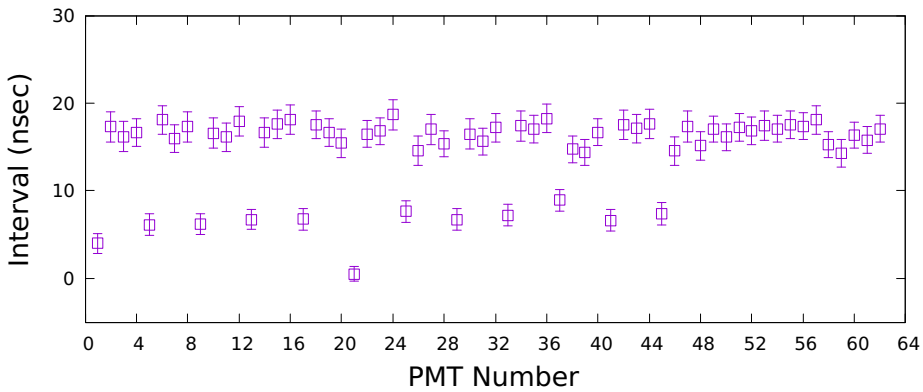

Figure F.2: The intervals, which are related to the SIGNAL INTERVALS, of 62 PMTs. Smaller value of interval indicates the lower overlapping probability.

The number of photoelectrons in the latter region (N_D) is calculated as:

$$N_D = N_0 \exp\left(-\frac{T}{\tau}\right) \tag{F.6}$$

Apply photon counting in the latter region, the number of photoelectrons counted (M_D) is (using equation F.4):

$$M_D = \frac{\tau}{\omega}\left(1 - \exp\left(-\frac{\omega}{\tau}N_D\right)\right) \tag{F.7}$$

$$\Rightarrow \frac{dM_D}{dN_D} = \exp\left(-\frac{N_D\omega}{\tau}\right) \tag{F.8}$$

The total number of photoelectrons obtained by partial photon counting (N_{total}) is:

$$N_{total} = N_P + M_D \tag{F.9}$$

$$= N_0\left(1 - \exp\left(-\frac{T}{\tau}\right)\right) + \frac{\tau}{\omega}\left(1 - \exp\left(-\frac{\omega}{\tau}N_0 \exp\left(-\frac{T}{\tau}\right)\right)\right) \tag{F.10}$$

In this thesis, the N_{total} is normalized to N_0. The statistical fluctuation of N_{total} after normalization is calculated as:

$$\Delta N_{total}^2 = \Delta N_P^2 + \left(\frac{dN_D}{dM_D}\right)^2 \Delta M_D^2 \tag{F.11}$$

$$= N_0\left(1 - \exp\left(-\frac{T}{\tau}\right)\right) + \frac{\tau}{\omega}\left(\exp\left(\frac{N_D\omega}{\tau}\right) - 1\right)\exp\left(\frac{N_D\omega}{\tau}\right) \tag{F.12}$$

Appendix G

Threshold in Photon Counting

Threshold is essential in photon counting method. In section 6.1, the threshold is selected based on the discrimination of 1p.e. and 0p.e. In this appendix, some results of overlap probability in photon counting and counting efficiency are presented.

Threshold and overlap probability

Figure G.1 shows the correlation of counted p.e. with true p.e. using different thresholds for PMT01 and PMT02. In PMT01 (10-inch), with threshold of $\mu - 1\sigma$, the counted p.e. is saturated as the other PMTs. For the threshold of $\mu - 2\sigma$, the number of counted p.e. is increased due to the signal reflection is more counted with a lower threshold level. For the threshold of $\mu - 3\sigma$, the number of counted p.e. is over-counted and more than the expected p.e. number. In PMT02, the correlations with different threshold levels are quite consistent with each other. With a lower threshold, the number of counted p.e. with the threshold of $\mu - 2\sigma$ is slightly more than when we use the with the threshold of $\mu - 1\sigma$. With these discussions, the threshold $\mu - 2\sigma$ is probed to be good enough for photon counting in CANDLES.

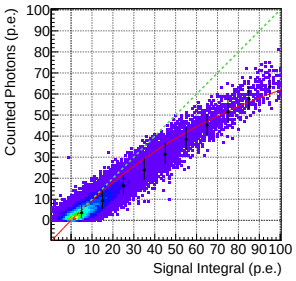

(a) PMT01, threshold = $\mu - 1\sigma$

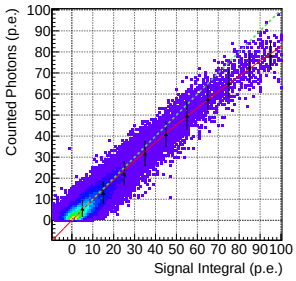

(b) PMT01, threshold = $\mu - 2\sigma$

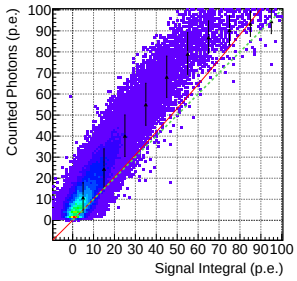

(c) PMT01, threshold = $\mu - 3\sigma$

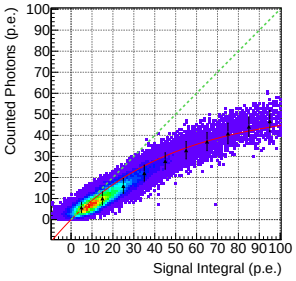

(d) PMT02, threshold = $\mu - 1\sigma$

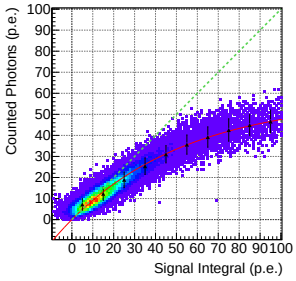

(e) PMT02, threshold = $\mu - 2\sigma$

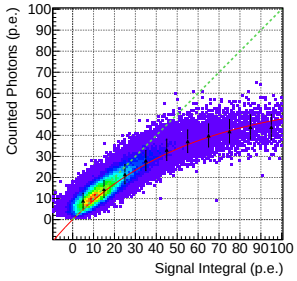

(f) PMT02, threshold = $\mu - 3\sigma$

Figure G.1: Correlation of counted p.e. with true p.e. using different thresholds for 2 PMTs

Bibliography

[1] S. Mukhi and P. Roy, "Developments in high energy theory", Pramana - J Phys, vol. 73, pp. 3–60 (2009).
DOI: 10.1007/s12043-009-0093-9

[2] J. Chadwick, "Comparison of the intensity of the different types of beta rays from radium B and radium C," Verh. d. deutschen Phys. Ges., vol. 16, pp. 383 (1914).

[3] C. L. Cowan, Jr. F. Reines, et al., "Detection of the Free Neutrino: a Confirmation," Science, vol. 20, no. 3212, pp. 103-104 (1956).
DOI: 10.1126/science.124.3212.103

[4] G. Danby, et al., "Observation of High-Energy Neutrino Reactions and the Existence of Two Kinds of Neutrinos," Phys. Rev. Lett., vol. 9, pp. 36 (1962).
DOI: 10.1103/PhysRevLett.9.36

[5] DONUT Collaboration, "Observation of tau neutrino interactions," Phys. Rev. Lett., vol. 504, no. 3, pp. 218-224 (2001).
DOI: 10.1016/S0370-2693(01)00307-0

[6] The ALEPH Collaboration, The DELPHI Collaboration, The L3 Collaboration, The OPAL Collaboration, The SLD Collaboration, The LEP Electroweak Working Group and The SLD Electroweak and Heavy Flavour Groups, "Precision electroweak measurements on the Z resonance," Physics Reports 427 (2006).
DOI: 10.1016/j.physrep.2005.12.006

[7] John N. Bahcall, Raymond Davis Jr., "Solar Neutrinos: A Scientific Puzzle," Science, vol. 191, no. 4224, pp. 264-267 (1976).
DOI: 10.1126/science.191.4224.264

[8] K. S. Hirata et al., "Experimental study of the atmospheric neutrino flux," Phys. Lett. B, vol. 205, no. 2-3, pp. 416-420 (1988).
DOI: 10.1016/0370-2693(88)91690-5

[9] V.Gribov and B.Pontecorvo, "Neutrino astronomy and lepton charge," Physics Letter B, vol. 28, no. 7, pp. 493-496 (1969).
DOI: 10.1016/0370-2693(69)90525-5

[10] S. Fukuda et al. (Super-Kamiokande Collaboration), "Solar and hep neutrino measurements from 1258 days of super-kamiokande data," Phys. Rev. Lett., vol. 86, p. 5651 (2001).
DOI: 10.1103/PhysRevLett.86.5651

[11] Q. R. Ahmad et al. (SNO Collaboration), "Direct evidence for neutrino flavor transformation from neutral-current interactions in the sudbury neutrino observatory," Phys. Rev. Lett., vol. 89, p. 011301 (2002).
DOI: 10.1103/PhysRevLett.89.011301

[12] P. Hernández, "Neutrino Physics," Proceedings of the 2015 CERN–Latin-American School of High-Energy Physics, CERN-2016-005 (2016).
DOI: 10.5170/CERN-2016-005.85

[13] I. Esteban et al., "Global analysis of three- avour neutrino oscillations: synergies and tensions in the determination of θ_{23}, δ_{CP}, and the mass ordering," Journal of High Energy Physics, vol. 2019, pp. 106,
DOI: 10.1007/JHEP01(2019)106

[14] G. Yang (JUNO Collaboration), "Neutrino mass hierarchy determination at reactor antineutrino experiments,"
arXiv:1509.08747v3 [physics.ins-det] 30 Apr 2016.

[15] PLANCK Collaboration, "Planck 2018 results. VI. Cosmological parameters,"
1807.06209v2 [astro-ph.CO] 20 Sep 2019.

[16] Craig Aalseth et al., "Neutrinoless double beta decay and direct searches for neutrino mass,"
arXiv:hep-ph/0412300v1 21 Dec 2004.

[17] M. Aker (KATRIN Collaboration), "An improved upper limit on the neutrino mass from a direct kinematic method by KATRIN," Phys. Rev. Lett, vol. 123, pp. 221802 (2019),
DOI: 10.1103/PhysRevLett.123.221802

[18] C. Patrignani et al., "The Review of Particle Physics (2017)", (Particle Data Group), Chin. Phys. C, 40, 100001 (2016) and 2017,
DOI: 10.1088/1674-1137/40/10/100001

[19] S. Dell'Oro, S. Marcocci, M. Viel and F. Vissani, "Neutrinoless Double Beta Decay: 2015 Review," Adv. High Energy Phys. 2162659 (2016).
DOI: 10.1155/2016/2162659

[20] M. Goeppert-Mayer, "Double Beta-Disintegration," Phys. Rev., vol. 48, no. 512 (1935).
DOI: 10.1103/PhysRev.48.512

[21] Andrea Giuliani and Alfredo Poves, "Neutrinoless Double-Beta Decay," Adv. High Energy Phys. 2012, pp. 1-38 (2012).
DOI: 10.1155/2012/857016

[22] A. Balysh et al., "Double Beta Decay of ^{48}Ca," Phys. Rev., Lett., vol. 77, pp. 5186 (1996).
DOI: 10.1103/PhysRevLett.77.5186

[23] The GERDA Collaboration, "Measurement of the half-life of the two-neutrino double beta decay of ^{76}Ge with the GERDA experiment," J. Phys. G: Nucl. Part. Phys., vol. 40, no. 3, pp. 035110 (2013).
DOI: 10.1088/0954-3899/40/3/035110

[24] NEMO3 Collaboration, "Measurement of the two neutrino double beta decay half-life of ^{96}Zr with the NEMO-3 detector," Nucl. Phys. A, vol. 847, no 3-4, pp. 168-179 (2010).
DOI: 10.1016/j.nuclphysa.2010.07.009

[25] R. Arnold et al. (NEMO-3 Collaborator), "First results of the search of neutrinoless double beta decay with the NEMO-3 detector", Phys. Rev. Lett., vol. 95, pp. 182302 (2005).
DOI: 10.1103/PhysRevLett.95.182302

[26] L. Simard et al. (NEMO-3 Collaborator), "The NEMO-3 results after completion of data taking," Journal of Physics: Conference Series, vol. 375, no. 4, pp. 042011 (2012),
DOI: 10.1088/1742-6596/375/1/042011

[27] R. Arnold et al. (NEMO-3 Collaborator), "Measurement of the Double Beta Decay Half-life of ^{130}Te with the NEMO-3 Detector," Phys. Rev. Lett., vol. 107, pp. 062504 (2011).
DOI: 10.1103/PhysRevLett.107.062504

[28] J. B. Albert et al. (EXO Collaboration), "Improved measurement of the $2\nu\beta\beta$ half-life of ^{136}Xe with the EXO-200 detector", Phys. Rev. C, vol. 89, pp. 015502 (2014).
DOI: 10.1103/PhysRevC.89.015502

[29] J. Argyriades et al. (NEMO Collaboration), "Measurement of the double-β decay half-life of ^{150}Nd and search for neutrinoless decay modes with the NEMO-3 detector," Phys. Rev. C, vol. 80, pp. 032501 (2009).
DOI: 10.1103/PhysRevC.80.032501

[30] Frank T. Avignone III, "Double beta decay, Majorana neutrinos, and neutrino mass," Rev. Mod. Phys., vol. 80, pp. 481-516 (2008).
DOI: 10.1103/RevModPhys.80.481

[31] Oliviero Cremonesi, "Neutrinoless double beta decay: Present and future," Nucl. Phys. B (Proc. Suppl.), vol. 118, pp. 287-296 (2003).
DOI: 10.1016/S0920-5632(03)01331-8

[32] J. Kotila and F. Iachello, "Phase space factors for double-β decay," Phys. Rev. C, vol. 85, pp. 034316 (2012).
DOI: 10.1103/PhysRevC.85.034316

[33] A. Faessler, V. Rodin and F. Simkovic, "Nuclear matrix elements for neutrinoless double beta decay and double-electron capture," J, Phys. G: Nucl. Part. Phys., vol. 39, pp. 124006 (2012).
DOI: 10.1088/0954-3899/39/12/124006/meta

[34] Y. Iwata et al., "Large-Scale Shell-Model Analysis of the Neutorinoless $\beta\beta$ Decay of ^{48}Ca," Phys. Rev. Lett., vol. 116, pp. 112502 (2016).
DOI: 10.1103/PhysRevLett.116.112502

[35] T. R. Rodriguez and G. M. Pinedo, "Energy Density Functional Study of Nuclear Matrix Elements for Neutrinoless $\beta\beta$ Decay," Phys. Rev. Lett., vol. 105, pp. 252503 (2010).
DOI: 10.1103/PhysRevLett.105.252503

[36] J. Barea, J. Kotila and F. Iachello, "$0\nu\beta\beta$ and $2\nu\beta\beta$ nuclear matrix elements in the interacting boson model with isospin restoration," Phys. Rev. C 91 034304 (2015).
DOI: 10.1103/PhysRevC.91.034304

[37] F. Simkovic et al., "$0\nu\beta\beta$ and $2\nu\beta\beta$ nuclear matrix elements, quasiparticle random-phase approximation, and isospin symmetry restoration,"

Phys. Rev. C 87 045501 (2013).
DOI: 10.1103/PhysRevC.87.045501

[38] S. R. Elliot and P. Vogel, "DOUBLE BETA DECAY," Ann. Rev. Nucl. Part. Sci. 52 115 (2002).
DOI: 10.1146/annurev.nucl.52.050102.090641

[39] S. Umehara et al., "Neutrino-less double-β decay of ^{48}Ca studied by CaF_2(Eu) scintillators," Phys. Rev. C 78, 058501 (2008).
DOI: 10.1103/PhysRevC.78.058501

[40] T. Iida et al., "First result of the CANDLES III experiment searching for double beta decay of ^{48}Ca," Poster the Neutrino Conference (2018).
DOI: 10.5281/zenodo.1300736

[41] M. Agostini et al., "Probing Majorana neutrinos with double-β decay," Science, vol. 365, no. 6460, pp. 1445-1448 (2019).
DOI: 10.1126/science.aav8613

[42] M. Agostini et al., "Supplementary Materials - Probing Majorana neutrinos with double-β decay," (2019).
DOI: 10.1126/science.aav8613

[43] O. Azzolini et al., "Final Result of CUPID-0 Phase-I in the Search for the ^{82}Se Neutrinoless Double-β Decay," Phys. Rev. Lett., vol. 123, pp. 032501 (2019).
DOI: 10.1103/PhysRevLett.123.032501

[44] NEMO Collaboration, "Measurement of the two neutrino double beta decay half-life of Zr-96 with the NEMO-3 detector," Nuclear Physics A, vol. 847, pp. 168-179 (2010).
DOI: 10.1016/j.nuclphysa.2010.07.009

[45] NEMO Collaboration, "Results of the search for neutrinoless double-β decay in ^{100}Mo with the NEMO-3 experiment," Phys. Rev. D, vol. 92, pp. 072011 (2015).
DOI: 10.1103/PhysRevD.92.072011

[46] A. S. Barabash et al., "Final results of the Aurora experiment to study 2β decay of ^{116}Cd with enriched $^{116}CdWO_4$ crystal scintillators," Phys. Rev. D, vol. 98, pp. 092007 (2018).
DOI: 10.1103/PhysRevD.98.092007

[47] C. Alduino et al. (CUORE Collaboration), "First Results from CUORE: A Search for Lepton Number Violation via $0\nu\beta\beta$ Decay of ^{130}Te," Phys. Rev. Lett., vol. 120, pp. 132501 (2018).
DOI: 10.1103/PhysRevLett.120.132501

[48] KamLAND-Zen Collaboration, "Search for Majorana Neutrinos Near the Inverted Mass Hierarchy Region with KamLAND-Zen," PRL 117 082503 (2016).
DOI: 10.1103/PhysRevLett.117.082503

[49] NEMO Collaboration, "Measurement of the $2\nu\beta\beta$ decay half-life of 150Nd and a search for $0\nu\beta\beta$ decay processes with the full exposure from the NEMO-3 detector," Phys. Rev. D 94 072003 (2016).
DOI: 10.1103/PhysRevD.94.072003

[50] A. Bakalyarov et al.,"Search for β^- and $\beta^-\beta^-$ decays of ^{48}Ca," Nucl. Phys. A, vol. 700, pp. 12-24, (2002).
DOI: 10.1016/S0375-9474(01)01306-9

[51] Y. Suzuki and K. Inoue, "Kamioka underground observatories," The Eur. Phys. J. Plus, vol. 127, p. 111 (2012).
DOI: 10.1140/epjp/i2012-12111-2

[52] Chan W.M., "Study of ^{180m}Ta Decay and Development of Ultra-low Background Gamma-ray Spectrometry," Ph.D. Thesis, Osaka University (2017)
DOI: 10.18910/61506.

[53] J. M. Carmona et al., "Neutron background at the Canfranc underground laboratory and its contribution to the IGEX-DM dark matter experiment," Astropart. Phys., vol. 21, pp. 523-533 (2004).
DOI: 10.1016/j.astropartphys.2004.04.002

[54] S. Yoshida, "CANDLES project for double beta decay of ^{48}Ca", Nuclear Physics B (Proc. Suppl.) vol. 138, pp. 214-216 (2005).
DOI: 10.1016/j.nuclphysbps.2004.11.051

[55] Hamamatsu Photonics K. K., "Photomultiplier tubes and assemblies for scintillation counting & high energy physics,"
Web (accessed date September 14 2020): R7081-100 Datasheet

[56] Hamamatsu Photonics K. K., "Photomultiplier tubes and assemblies for scintillation counting & high energy physics,"
Web (accessed date September 14 2020): R8055 R7250 Datasheet

[57] S. Umehara et al., "Search for Neutrino-less Double Beta Decay with CANDLES," Physics Procedia, vol. 61, pp. 283 – 288 (2015).
DOI: 10.1016/j.phpro.2014.12.046

[58] K. Nakajima et al., "Performance of updated shielding system in CANDLES," AIP Conference Proceedings 1921, 060003 (2018).
DOI: 10.1063/1.5018999

[59] T. Iida et al., "Status and future prospect of ^{48}Ca double beta decay search in CANDLES," J. of Phys.: Conf. Series, vol. 718, no. 6, p. 062026 (2016).
DOI: 10.1088/1742-6596/718/6/062026

[60] Y. Hirano, "CANDLES Detector for the study of Double Beta Decay of ^{48}Ca," Ph.D. Thesis Osaka University (2008).
Thesis link - Local access in CANDLES

[61] S. Yoshida et al., "Ultra-violet wavelength shift for undoped CaF_2 scintillation detector by two phase of liquid scintillator system in CANDLES," Nucl. Ins. Meth. A, vol. 601, pp. 282-293 (2009).
DOI: 10.1016/j.nima.2008.12.190

[62] H. Kakubata, "Study of Backgrounds in CANDLES to search for Double Beta Decays of ^{48}Ca," Ph.D. Thesis, Osaka University (2015).
DOI: 10.18910/54022

[63] T. Maeda et al., "The CANDLES Trigger System for the Study of Double Beta Decay of ^{48}Ca," IEEE Trans. Nucl. Sci., vol. 62, pp. 1128–1134 (2015).
DOI: 10.1109/TNS.2015.2423275

[64] K. Suzuki et al., "New DAQ System for the CANDLES Experiment," IEEE Trans. Nucl. Sci., vol. 62, no. 3, pp. 1122–1127 (2015).
DOI: 10.1109/TNS.2015.2423673

[65] B. T. Khai et al., "μTCA DAQ System and Parallel Reading in CANDLES Experiment," IEEE Trans. Nucl. Sci., vol. 66, no. 7, pp. 1174–1181 (2019).
DOI: 10.1109/TNS.2019.2900984

[66] Texas Instruments, "Low Power, 8-Bit, Dual 500 MSPS A/D Converter," March 2013, Web (accessed date September 14 2020): ADC08DL502 Data Sheet.

[67] M. Nomachi and S. Ajimara, "Serial Data Link on Advanced TCA Back Plane," IEEE Trans. Nucl. Sci., vol. 53, no. 5, pp. 2849-2852 (2006).
DOI: 10.1109/TNS.2006.882776

[68] S. Umehara et al., "Search for Neutrino-less Double Beta Decay with CANDLES," Phys. Procedia, vol. 61, pp. 283 – 288 (2015).
DOI: 10.1016/j.phpro.2014.12.046

[69] S.R.Hashemi-Nezhad and L.S.Peak, "Background neutron flux determination at a depth of 3200 mwe underground," Nucl. Inst. Meth. A, vol. 357, no. 2-3, pp. 524-534 (2015).
DOI: 10.1016/0168-9002(94)01527-9

[70] A. Minamino, "XMASS実験、100kg検出器の性能評価と中性子バックグラウンドの研究," Master Thesis, University of Tokyo (2004).
Thesis link

[71] D.-M. Mei and A. Hime, "Muon-induced background study for underground laboratories," Phys. Rev. D, vol. 73, pp. 053004 (2006).
DOI: 10.1103/PhysRevD.73.053004

[72] T. Maeda, "Study of Ca-49 Background in Neutrinoless Double Beta Decay of Ca-48," Ph.D. Thesis, Osaka University (2018).
Thesis link

[73] T. Ohata, "Search for Neutrinoless Double Beta Decay in ^{48}Ca with the CANDLES III experiment," Ph.D. Thesis, Osaka University (2018).
Thesis link

[74] K. Mizukoshi, "Energy response of CANDLES detector and background of ambient neutron in underground," Master Thesis, Osaka University (2019).
Thesis link

[75] M. Moser, "Analysis of neutron induced background in CANDLES," Master Thesis, Osaka University (2017).
Thesis link

[76] S. Okumura et al., "Recent Studies on Ca Isotope Separation by Crown-Ether Resin Chromatography," J. Nucl. Radiochem. Sci, 16 (2015).
DOI: 10.14494/jnrs.16.11

[77] S. Umehara et al., "A basic study on the production of enriched isotope ^{48}Ca by using crown-ether resin," Prog. Theor. Exp. Phys., vol. 2015,

pp. 053C03 (2015).
DOI: 10.1093/ptep/ptv063

[78] B. E. Jepson and R. Dewitt, "SEPARATION OF CALCIUM ISOTOPES WITH MACROCYCLIC POLYETHER CALCIUM COMPLEXES," J. Inorg, Nucl. Chem. 38 (1976).
DOI: 10.1016/0022-1902(76)80244-8

[79] T. Kishimoto, K. Matsuoka, T. Fukumoto, and S. Umehara, "Calcium isotope enrichment by means of multi-channel counter-current electrophoresis for the study of particle and nuclear physics," Prog. Theor. Exp. Phys. 033D03 (2015).
DOI: 10.1093/ptep/ptv020

[80] C.J. Kim et. al., "Proliferation-resistant stable isotope separation based on optical pumping," Proceeding of the 10. International workshop on SPLG2008 (2008)

[81] A. P. Babichev et. al., "Development of the laser isotope separation method (AVLIS) for obtaining weight amounts of highly enriched 150Nd isotope," Quantum Electron. 35 879 (2005).
DOI: 10.1070/QE2005v035n10ABEH006601

[82] S. Umehara, "Neutrino-less double beta decay of ^{48}Ca studied by CaF_2(pure) scintillators," Oral Presentation in International Conference on Topics in Astroparticle and Underground Physics, 24-28 July (2017).

[83] K. Tetsuno, "Status of ^{48}Ca double beta decay search and its future prospect in CANDLES," Oral Presentation in International Conference on Topics in Astroparticle and Underground Physics, 9-13 September (2019).

[84] X. Li, "Study of a Large CaF_2(Eu) Scintillating Bolometer for Neutrinoless Double Beta Decay," Poster Presentation in International Conference on Topics in Astroparticle and Underground Physics, 9-13 September (2019).

[85] K. K. Lee, " Bolometer Development using Neutron Transmutation Doped Ge in CANDLES for the study of Neutrinoless Double Beta decay," Oral Presentation in Japan Physics Society Autumn Meeting 2019, 10-13 September (2019).

[86] V. B. Brudanin et al., "Search for double beta decay of ^{48}Ca in the TGV experiment," Physics Letters B, vol. 495, no 1-2, pp. 63-68 (2000).
DOI: 10.1016/S0370-2693(00)01244-2

[87] A. S. Barabash, "Average (recommended) half-life values for two-neutrino double-beta decay," Czechoslovak Journal of Physics, vol. 52, no. 4 (2002).
DOI: 10.1023/A:1015369612904

[88] M. Moszyński et al., "Intrinsic energy resolution of NaI(Tl)," Nucl. Inst. Meth. A, vol. 484, no. 1-3, pp. 259-269 (2002).
DOI: 10.1016/S0168-9002(01)01964-7

[89] M. Moszyński, "Energy resolution and non-proportionality of scintillation detectors – new observations," Nucl. Inst. Meth. A, vol. 45, no. 3-6, pp. 372-376 (2010).
DOI: 10.1016/j.radmeas.2009.10.012

[90] M. Moszyński et al., "Energy resolution of scintillation detectors," Nucl. Inst. Meth. A, vol. 805, pp. 25-35 (2016).
DOI: 10.1016/j.radmeas.2009.10.012

[91] IEEE Instrumentation Society, "IEEE Standard for Digitizing Waveform Recorders", IEEE Std 1057^{TM}-2017 (2018).
DOI: 10.1109/IEEESTD.2018.8291741

[92] K. Kanagawa, "μTCA規格による読み出しシステムを用いた CaF_2(Eu) 結晶のエネルギー分解能の測定," Master Thesis, Osaka University (2017).
Thesis link - Local access in CANDLES

[93] H. Kino, "CANDLES実験のためのLED光源を用いた1光電子測定," Master Thesis, Osaka University (2018).
Thesis link - Local access in CANDLES

[94] E. Kinoshita, "1p.e. analysis", Non-Accelerator Meeting (NAP) report in CANDLES, Mar. 13th (2017).

[95] B. T. Khai, "PMT Noise", Non-Accelerator Meeting (NAP) report in CANDLES, Apr. 17th (2017).

[96] M. Tsuzuki, "CANDLES実験のための時間較正," Master Thesis, Osaka University (2017).
Thesis link - Local access in CANDLES

[97] S. Derenzo, M. Boswell, M. Weber and K. Brennan (Lawrence Berkeley National Laboratory), Scintillation Properties Website (accessed date February 24 2020).

[98] Laboratoire National Henri Becquerel, Nucléide - Lara, Library for gamma and alpha emissions (accessed date February 24 2020).

[99] V.B. Mikhailik et al., "Scintillation properties of pure CaF_2", Nucl. Inst. and Meth. in Phys. Res. A, vol. 566, pp. 522–525 (2006), DOI: 10.1016/j.nima.2006.06.063

[100] Cryomech Co., "Pulse Tube Cryocoolers (online resource)" (accessed date February 24 2020).

[101] U. Wagner, "REFRIGERATION", CAS - CERN Accelerator School on Superconductivity and Cryogenics for Accelerators and Detectors, Erice, Italy, 8 - 17 May 2002, pp.295-345, DOI: 10.5170/CERN-2004-008.295

[102] M. Doi, T. Kotani et al., "Neutrino Mass, the Right-Handed Interaction and the Double Beta Decay, I", Prog. Theo. Phys., vol. 66, no. 5 (1981). DOI: 10.1143/PTP.66.1739